

Faraday Accelerator with Radio-frequency Assisted Discharge (FARAD)

Kurt Alexander Polzin

A DISSERTATION
PRESENTED TO THE FACULTY
OF PRINCETON UNIVERSITY
IN CANDIDACY FOR THE DEGREE
OF DOCTOR OF PHILOSOPHY

RECOMMENDED FOR ACCEPTANCE
BY THE DEPARTMENT OF
MECHANICAL AND AEROSPACE ENGINEERING

June 2006

Faraday Accelerator with Radio-frequency Assisted Discharge (FARAD)

Prepared by:

Kurt Alexander Polzin

Approved by:

Professor Edgar Y. Choueiri
Dissertation Advisor

Professor Robert G. Jahn
Dissertation Reader

Dr. Michael R. LaPointe
Dissertation Reader

© Copyright by Kurt Alexander Polzin, 2006. All rights reserved.

Abstract

A new electrodeless accelerator concept, called Faraday Accelerator with Radio-frequency Assisted Discharge (FARAD), that relies on an RF-assisted discharge to produce a plasma, an applied magnetic field to guide the plasma into the acceleration region, and an induced current sheet to accelerate the plasma, is presented. The presence of a preionized plasma allows for current sheet formation at lower discharge voltages and energies than those found in other pulsed inductive accelerator concepts. A proof-of-concept experiment, supported by optical and probe diagnostics, was constructed and used to demonstrate the main features of the FARAD and to gain physical insight into the low-voltage, low-energy current sheet formation and acceleration processes. Magnetic field data indicate that the peak sheet velocity in this unoptimized configuration operating at a pulse energy of 78.5 J is 12 km/s. It is found that changes in the background gas pressure and applied field affect the initial preionized plasma distribution which, in turn, affects the sheet's initial location, relative magnetic impermeability and subsequent velocity history.

The results of the experimental investigation motivated further theoretical and numerical investigations of pulsed inductive plasma acceleration. A model consisting of a set of coupled circuit equations and a one-dimensional momentum equation was nondimensionalized leading to the identification of several scaling parameters. Numerical analysis revealed the benefits of underdamped current waveforms and led to an efficiency maximization criterion that requires matching the external circuit's natural period to the acceleration timescale. Predictions of the model were compared to experimental measurements and were found to be in good qualitative agreement and reasonable quantitative agreement for most quantities.

A set of design rules aimed at producing a high-performance FARAD thruster are de-

rived using the modeling results and physical insights. The rules concern the optimization of each of the major processes in FARAD: plasma acceleration, current sheet formation, applied field generation, and mass injection and preionization, and are cast as specific prescriptions for the dynamic impedance, inductance change, circuit damping, plasma collisionality (or magnetization), magnetic field strength and topology, and intra-pulse sequencing.

Acknowledgments

This dissertation could not have been completed without the support and encouragement of many individuals, to whom I am very grateful. I wish to especially thank:

My wife Sheri and our daughter Allie, who have both forever changed my life for the better. Thank you for your continued patience, understanding and love as I completed this journey. I could not have gotten this far without your support.

My parents, David and Linda, who taught me well and always expected nothing less than my best. Much of what I have achieved I owe to you and the values you taught me. Thank you.

Prof. Edgar Choueiri, who throughout the completion of this dissertation has consistently pushed me to dig deeper to locate important physical insights revealed by experimental data or numerical results. I have learned much about scientific investigation and communication from you, making me more prepared for my future research endeavors.

Robert Sorenson, from whom I learned most of what I know about RF power transfer, circuit design and analysis, soldering, machining, Smith charts and gold. Thank you.

Rostislav ‘Slava’ Spektor, who graciously shared his experimental apparatus with me during the course of our dissertation research. Thank you for your patience and aid as we worked to complete our work.

Kamesh Sankaran and Tom Markusic, both of whom helped me extensively throughout my time at Princeton and have contributed many valuable suggestions during the preparation of this dissertation. Thank you.

Andrea, Lenny, Jack, Jimmy, Vince, Slava, Kamesh, Tom. You have been colleagues and, more importantly, friends of both myself and my family over the past several years. I shall look back fondly on the good times we had together.

Mr. Kenneth Kormanyos, Mr. Clyde Bame and Mr. Bruce Smith, who instilled within me a deep love of physics and a desire to investigate the physical world we inhabit. You provided me with the first tools to begin my own journey of exploration and discovery. Thank you.

This dissertation carries the designation 3147-T in the records of the Department of Mechanical and Aerospace Engineering. Support for the research was provided by the National Defense Science and Engineering Graduate Fellowship Program.

Nomenclature

a	Inner radius [m]
A_p	Probe surface area [m ²]
b	Outer radius [m]
\mathbf{B}, B	Magnetic induction vector, scalar [T]
C	Circuit capacitance [F]
\mathbf{D}	Displacement current vector [C/m ²]
e	Elementary charge [C]
E	Electric field [V/m]
F	Force [N]
g_0	Gravitational acceleration [m/s ²]
I_1, J_{Coil}	Accelerator coil current [A]
I_2, J_{Plasma}	Induced plasma current [A]
I_{enc}	Enclosed current [A]
I_{sat}	Ion saturation current [A]
I_{sp}	Specific impulse [s]
J	Total current [A]
\mathbf{j}, j	Current density vector, scalar [A/m ²]
k	Boltzmann constant [J/K]
L	Inductance [H]
\mathcal{L}	Characteristic acceleration coil dimension [m]
L^*	Inductance ratio
L_a	Antenna inductance [H]
L_C	Acceleration coil inductance [H]
L_{term}	Terminal (series) inductance [H]
L_{tot}	Total circuit (series) inductance [H]
M	Mutual Inductance [H]
\dot{m}	Mass flow rate [kg/s]
m_{bit}	Propellant mass per pulse [kg]
m_i	Initial spacecraft mass or ion mass [kg]
m_p	Propellant mass [kg]
m_{ps}	Power supply mass [kg]
$\hat{\mathbf{n}}$	Unit normal vector
n_e	Number density [m ⁻³]
p	Gas pressure [Pa]

Nomenclature (Cont.)

Q	Charge [C]
R	Circuit resistance [Ω]
$r_{ce, ci}$	Electron, ion cyclotron radius [m]
R_c	Radius of curvature of helicon to accel. stage transistion [m]
R_e	External circuit resistance [Ω]
R_H	Helicon stage radius [m]
R_p	Plasma circuit resistance [Ω]
r	Radial coordinate [m]
$t, \Delta t$	Time, time increment [s]
T	Thrust [N]
$T_{e, i}$	Electron, ion temperature [eV or K]
u, v, \dot{z}	Velocity [m/s]
u_e	Exhaust velocity [m/s]
U_m	Magnetic field potential energy [J]
V	Voltage [V]
V_{bias}	Bias voltage [V]
V_{float}	Floating potential [V]
v_A	Alfvén speed [m/s]
v_{CIV}	Critical ionization velocity [m/s]
$v_{th, (e, i)}$	Electron, ion thermal speed [m/s]
v_{\perp}	Particle velocity perpendicular to magnetic field vector [m/s]
z	Axial coordinate [m]
$z_{initial, final}$	Initial, final axial position [m]
α	Ionization fraction or dynamic impedance ratio
α_p	Power supply specific mass [kg/kW]
β_e	Plasma energy/magnetic field energy
δ	Current sheet width [m]
ΔL	Inductance change [H]
δ_m	Propellant distribution axial thickness [m]
$\Delta t_{a, g, RF}$	Acceleration coil, gas injection, RF pulse widths [s]
Δv	Mission velocity increment [m/s]
λ_D	Debye length [m]
η, η_t	Efficiency, thrust efficiency [%]
γ	Applied field acceleration parameter

Nomenclature (Cont.)

μ	First adiabatic invariant [J/T]
μ_0	Permeability of vacuum [N/A ²]
ν	Applied field back-EMF parameter
$\nu_{e,i}$	Total electron, ion collision frequency [Hz]
ω	Frequency [rad/s]
$\omega_{ce,ci}$	Electron, ion cyclotron frequency [rad/s]
$\Omega_{e,i}$	Electron, ion Hall parameter
$\psi_{1,2}, \Psi$	Critical resistance ratios
ρ	Gas density [kg/m ³]
ρ_A	Linear gas density [kg/m]
σ	Error/standard deviation

Common Subscripts

Applied	Applied Field
P	Poloidal
r	Radial
ss	Strong Sheet
T	Toroidal
ws	Weak Sheet
z	Axial
0	Initial
θ	Azimuthal

Contents

Abstract	iii
Acknowledgments	v
Nomenclature	vi
List of Figures	xiii
List of Tables	xvii
1 Introduction	1
1.1 Pulsed Inductive Acceleration	2
1.2 Previous Work: Pulsed Inductive Thruster	4
1.3 FARAD Concept	8
1.4 Dissertation Scope and Outline	12
2 FARAD Proof-of-Concept Experiment	14
2.1 Vacuum Vessel	14
2.2 Applied Magnetic Field	16
2.2.1 Magnetostatic Model	16
2.2.2 Applied Field Calibration Measurements	17
2.2.3 FARAD Applied Field Design	18
2.3 Plasma Generation	19
2.4 Acceleration Coil	20

2.5	Experimental Operation	22
3	Experimental Diagnostics	23
3.1	Current Monitoring	23
3.2	Voltage Probe	25
3.3	Magnetic Field Probes	25
3.4	Imacon Fast-Framing Camera	26
3.5	Langmuir Probes	28
4	Experimental Observations and Measurements	31
4.1	Circuit Measurements	33
4.1.1	Acceleration Coil Current	33
4.1.2	Capacitor Voltage Measurements	34
4.2	General Visual Observations	36
4.3	Magnetic Field	38
4.3.1	Applied Field	38
4.3.2	Induced Field Measurements	39
4.4	Current Density Contours	44
4.5	Current Sheet Visualization	48
4.6	Plasma Density	54
4.7	Calculated Plasma Parameters	61
4.8	Discussion	65
4.9	Summary of Findings	74
5	Inductive Acceleration Modeling	76
5.1	Governing Equations	77
5.1.1	Circuit Equations	77

5.1.2	Momentum Equation	79
5.1.3	Plasma Model	80
5.1.4	Addition of an Applied Magnetic Field	81
5.1.5	Additional Shortcomings of the Acceleration Model	82
5.2	Nondimensional Equations	84
5.3	Interpretation of the Scaling Parameters	87
5.3.1	Inductance Ratio: L^*	87
5.3.2	Critical Resistance Ratios: ψ_1 and ψ_2	87
5.3.3	Dynamic Impedance Parameter: α	88
5.3.4	Applied Field Acceleration Parameter: γ	89
5.3.5	Applied Field Back-EMF Parameter: ν	90
5.4	Nondimensional Solutions	91
5.4.1	Solution Strategy	91
5.4.2	Solutions	92
5.5	Implications of the Results	98
5.6	Comparison with FARAD POCX Results	102
5.6.1	Accelerator Coil Current	103
5.6.2	Acceleration Model Modifications for FARAD Simulations	104
5.6.3	Plasma Current	106
5.6.4	Current Sheet Trajectory	108
5.7	Summary of Findings	110
6	Conclusion	113
6.1	FARAD Design and Optimization Ruleset	114
6.1.1	Plasma Acceleration	116
6.1.2	Current Sheet Formation	116

6.1.3	Applied Magnetic Field Generation	118
6.1.4	Mass Injection and Preionization	124
6.1.5	Summary	127
6.2	FARAD Research Directions	127
A	Literature Review	131
A.1	The Pulsed Inductive Thruster (PIT)	132
A.1.1	Early Research & Development: 1965-1973	133
A.1.2	Thruster System Development: 1979-1988	138
A.1.3	Current State-of-the-Art: 1991-Present	143
A.2	Other Pulsed Inductive Acceleration Concepts	147
A.2.1	Theta Pinch	147
A.2.2	Field-Reversed Configuration	149
A.3	Summary	152
B	Computer Algorithms	154
	Bibliography	167

List of Figures

1.1	Schematics diagramming the operation of pulsed inductive accelerators . . .	2
1.2	Schematic illustration of the PIT	5
1.3	Marx generator PIT coil configuration	7
1.4	Schematic illustration of the FARAD concept.	9
2.1	Photograph of the FARAD proof-of-concept experimental facility	15
2.2	Photograph of the FARAD POCX	15
2.3	Schematic of the applied field model geometry	17
2.4	Comparison of applied field measurements and calculations	18
2.5	RF discharge circuit schematic	19
2.6	End view of the FARAD experiment	20
2.7	FARAD acceleration stage circuit schematic	21
3.1	Schematic of a Rogowski coil.	24
3.2	B -dot probe photograph and circuit schematic	26
3.3	Relative positions of the different measurement locations	27
3.4	Langmuir probe circuit schematic	28
4.1	Acceleration coil total current waveforms	34
4.2	Capacitor voltage waveforms	35

4.3	Steady-state RF-plasma photograph	36
4.4	Comparison of applied fields computed for the Base and B_{\downarrow} cases	38
4.5	Radial and axial applied magnetic field value at $r = 66$ mm	39
4.6	Radial induced magnetic field strengths as a function of energy	40
4.7	Radial induced magnetic field strengths as a function of background pressure	42
4.8	Radial induced magnetic field strengths as a function of applied field strength	43
4.9	Radial induced magnetic field strengths with no preionization	43
4.10	Azimuthal current densities as a function of energy	45
4.11	Azimuthal current densities as a function of background pressure	47
4.12	Azimuthal current densities as a function of applied field strength	48
4.13	Representative high-speed current sheet images	49
4.14	Photographically measured current sheet position as a function of energy . .	51
4.15	Photographically measured current sheet position as a function of back- ground pressure	52
4.16	Photographically measured current sheet position as a function of applied field configurations	53
4.17	Plasma density measurements for the $E_{\downarrow\downarrow}$ case	56
4.18	Plasma density measurements for the $E_{\downarrow\downarrow} P_{\downarrow}$ case	57
4.19	Plasma density measurements for the $E_{\downarrow\downarrow} P_{\uparrow}$ case	59
4.20	Plasma density measurements for the $E_{\downarrow\downarrow} B_{\downarrow}$ case	60
4.21	Characteristic frequencies in the FARAD plasma	63
4.22	Length scales in the FARAD plasma	64
4.23	Plasma and current density measurement comparison for $E_{\downarrow\downarrow}$ case	69
4.24	Assumed preionized plasma axial distribution and assumed initial current sheet location and strength	72

5.1	Pulsed inductive accelerator lumped-element circuit model	78
5.2	Accelerator lumped-element circuit model with applied magnetic field . . .	82
5.3	Comparison of experimentally acquired and numerically generated current waveforms	83
5.4	Non-dimensional performance as a function of ψ_1 and ψ_2 vs α , slug mass loading	94
5.5	Non-dimensional performance as a function of ψ_2 vs ψ_1 and L^* vs ψ_2 , slug mass loading	95
5.6	Thrust efficiency as a function of ψ_1 vs α , non-slug mass loading	96
5.7	Thrust efficiency as a function of γ vs α , slug mass loading	97
5.8	Time histories of the various computed parameters in a pulsed inductive accelerator for different values of ψ_1, ψ_2	100
5.9	Comparison of measured and predicted coil currents	104
5.10	Delays before starting plasma acceleration computation in the FARAD simulations	105
5.11	Comparison of measured and predicted plasma current densities	106
5.12	Comparison of measured and predicted current sheet trajectories	109
6.1	Schematic of a pulsed inductive accelerator coil face	118
6.2	Schematics of non-optimized and optimized FARAD applied field topologies	120
6.3	Conceptual sketch of the ideal applied field strength profile in the accel- eration region	122
6.4	Conceptual rendering of a FARAD thruster	128
A.1	Schematic showing the operation of a planar pulsed inductive accelerator .	132
A.2	Schematic showing a typical pulsed inductive thruster propellant injection scheme	135

A.3	Circuit schematics for various inductive accelerator preionization schemes .	136
A.4	Ringing and clamped mode PIT MkIV circuit schematics	140
A.5	PIT MkI & MkIV performance data	141
A.6	PIT MkI magnetic field measurements	142
A.7	PIT MkIV magnetic field measurements	142
A.8	Fully-assembled PIT MkV	143
A.9	Marx generator PIT coil configuration	144
A.10	PIT MkV performance data	145
A.11	Theta pinch and conical theta pinch drawings	148
A.12	Stages in the formation of an FRC plasma	150
A.13	Schematic representations of two pulsed plasmoid thruster configurations .	152

List of Tables

4.1	Summary of experimental conditions	33
4.2	Sheet velocities inferred from j_θ measurements	48
4.3	Sheet velocities inferred from current sheet visualization	54
4.4	Summary of experimental conditions for Langmuir probe data	55
4.5	Estimated plasma parameters	61
4.6	Estimated dimensionless plasma parameters and characteristic plasma ve- locities	65
5.1	Summary of experimental conditions	102
5.2	Parameters for comparison between acceleration model and FARAD data .	103
5.3	Current sheet widths used to estimate current density based on modeling . .	107
A.1	Performance of early pulsed inductive accelerators	137
A.2	Performance of a 1 m diameter pulsed inductive thruster	139
A.3	Summary of the PIT MkV performance data	145

Chapter 1

Introduction

Pulsed inductive plasma accelerators are electrodeless spacecraft propulsion devices in which energy is stored in a capacitor and then discharged quickly through an inductive coil, inducing a plasma current sheet near the face of the coil. The current in the sheet interacts with an induced magnetic field, producing a Lorentz body force that accelerates the sheet, which in turn entrains surrounding propellant, to high exhaust velocity (\mathcal{O} (10 km/s)) thus producing useful impulsive thrust.

Inductive plasma accelerators are attractive as propulsive devices for many reasons. The lifetime and contamination issues associated with electrode erosion in conventional pulsed plasma thrusters (PPTs) do not exist in electrodeless devices where the discharge is inductively driven. In addition, a wider variety of propellants (e.g. CO_2 , H_2O) becomes available for use when compatibility with metallic electrodes is no longer an issue. Moreover, pulsed inductive accelerators (indeed, pulsed accelerators in general) can maintain the same performance level over a wide range of input power levels by adjusting the pulse rate.

1.1 Pulsed Inductive Acceleration

While the acceleration mechanism will be discussed in detail later, it is, perhaps, best to introduce the concept of pulsed inductive acceleration with an illustrative example. Imagine two conducting rings, aligned as shown in Fig. 1.1A. A current pulse, I_1 , is driven in the lower ring by a discharging capacitor. This current induces a magnetic field in accordance with Ampère's law:

$$\nabla \times \mathbf{B} = \mu_0 \mathbf{j}.$$

Any temporal-variation in the magnetic field induces an electric field (and consequently a voltage drop) in the upper ring according to Faraday's law:

$$\nabla \times \mathbf{E} = -\frac{\partial \mathbf{B}}{\partial t}.$$

It is this electric field which drives the current, I_2 , in the upper ring. Currents I_1 and I_2 flow in opposite directions since current I_2 must flow in the direction needed to prevent the flux created by I_1 from penetrating the upper ring. The currents in the two rings repel each

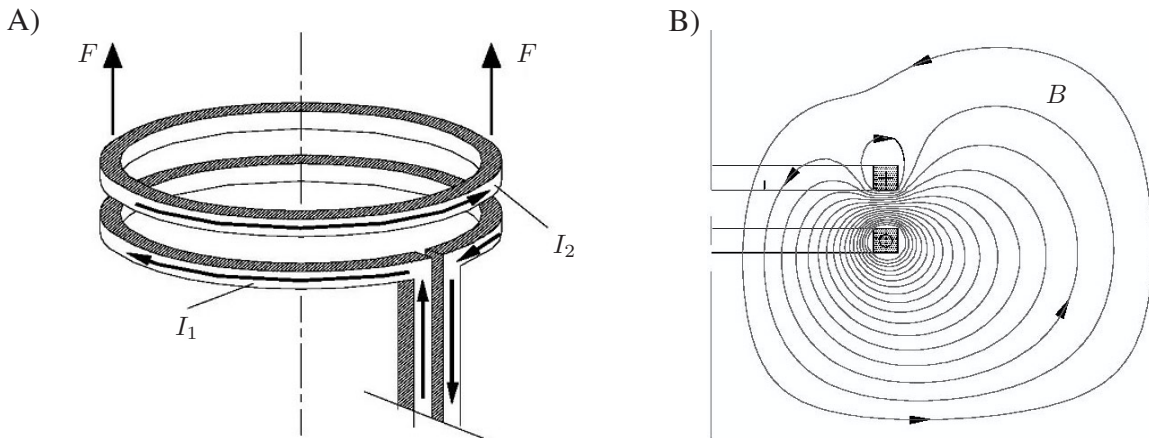


Figure 1.1: A) A schematic showing the currents and forces found in a set of coupled rings and B) a cross-sectional view showing the resulting magnetic field distribution. (Both images after Ref. [1].)

other, and if we take the lower ring as our reference frame, the upper ring “feels” a force, F , which accelerates it in the direction indicated.

A cross-sectional view of the current carrying rings and the magnetic field found in figure 1.1A is shown in fig. 1.1B. Between the two rings the magnetic field is tightly concentrated. This is the source of the force felt between the rings, which can be understood in one of three equivalent ways:

1. The concentration of flux lines results in an elevated magnetic pressure ($B^2/2\mu_0$) which pushes against the conducting rings as the magnetic field attempts to expand.
2. The induced radial magnetic field interacts with the induced azimuthal current I_2 to yield a Lorentz force, causing the ring to accelerate.
3. From a circuit analysis perspective, the tightly packed field lines represent a low inductance, high potential energy configuration. The magnetic force between the rings acts to minimize the potential energy of the system by maximizing its inductance. This is most easily accomplished by pushing the two rings apart.

Development of an efficient pulsed inductive plasma accelerator is not without its challenges. Jahn succinctly states the following two difficulties which must be overcome in an efficient accelerator:

“... inductive discharges embody two inherent electrodynamic disadvantages to conversion efficiency which detract from their propulsive effectiveness. First, any delay in breakdown of the gas after application of the primary field pulse results in energy being dissipated in the external circuit, which, unlike that of the direct electrode devices, is complete without the gas loop... This difficulty might be relieved by providing a separate preionization mechanism or by op-

eration at a sufficiently rapid repetition rate, but it is indicative of an inherent inefficiency in coupling of the external circuit to the plasma.”[2]

“Equally troublesome is the need to accomplish all the energy input to the gas before much motion of it has occurred. The current induced in the gas-loop “secondary” depends on its mutual inductance with the external primary, and thus is a strong function of the physical separation of these two current paths. As they separate under the acceleration, the coupling rapidly becomes weaker.”[2]

In other words, if current is pulsed in the induction coil and there is no plasma, or the plasma is late in forming, the magnetic field produced by the coil (and the associated field energy) will radiate into space and be lost without performing any useful work. In addition, any acceleration of the plasma must occur very quickly before it gets too far from the acceleration coil and effectively decouples from the magnetic field induced by the current in the coil.

1.2 Previous Work: Pulsed Inductive Thruster

The Pulsed Inductive Thruster (PIT)[1, 3] is the most mature concept employing inductive plasma acceleration. Development of the PIT has been primarily directed by C.L. Dailey and R.H. Lovberg with the work occurring at TRW Space Systems in Redondo Beach, CA (later acquired by Northrop-Grumman). Development began with fundamental proof-of-concept studies performed in the mid-1960s. The present PIT base design was proposed in the early 1990s and was guided by the lessons learned from several previous design iterations. Present day work is aimed at improving the various components in that base PIT design.

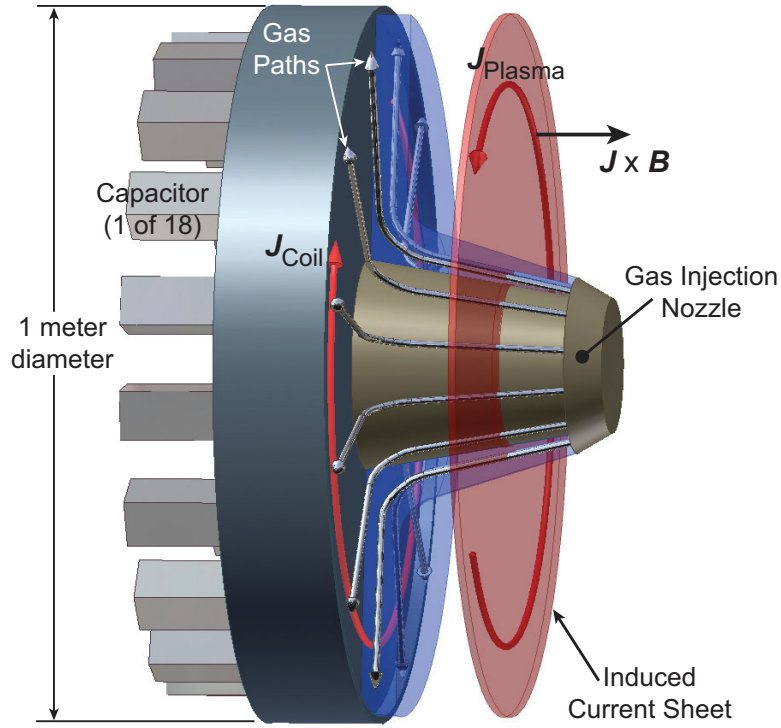


Figure 1.2: Schematic illustration of the PIT. (Neutral gas-filled region (blue volume) sectioned to show inner detail.)

From a development standpoint, the PIT represents the state-of-the art in inductive plasma acceleration. It is, in fact, the only pulsed inductive accelerator concept for which thrust data currently exists, achieving thrust efficiencies near 50% over a range of I_{sp} from 3000-8000 sec. In this section, we describe the current PIT design, paying special attention to the methods employed to alleviate the difficulties cited at the end of the previous section. This is followed by a brief description of some of the shortcomings inherent in the design. A full review of the research and development history of the PIT is provided in Appendix A and the findings of that review are summarized at the end of this section

A schematic rendering of the PIT is shown in Fig. 1.2. Neutral gas (propellant) injected from a nozzle located at the downstream end of the device propagates down the sides of the nozzle's cone structure and spreads over the face of the acceleration coil. The capaci-

tors are discharged through the acceleration coil to create a large azimuthal current, J_{Coil} , once propellant completely covers the coil. After a short but finite delay, the current pulse ionizes the gas, forming a current sheet containing an induced current J_{Plasma} , which is subsequently accelerated by a $\mathbf{j} \times \mathbf{B}$ force density in the direction indicated in Fig. 1.2.

In the previous section, the inherent inefficiencies arising from the delay between the initiation of the primary current pulse and the formation of the current sheet were cited. These detrimental effects have been experimentally demonstrated in previous PIT design iterations[4, 5]. It was found in these experiments that the delay between initiation of the current pulse and formation of the current sheet was decreased by increasing the initial current rise rate, dI/dt , in the acceleration coil. As the delay was decreased, current sheets were formed that were capable of better entraining and accelerating more of the encountered propellant.

The lessons learned in previous design iterations were incorporated into the latest version of the PIT[3], which is roughly 1 meter in diameter and possesses an acceleration coil comprised of 18 half-turn spiral loops of wire. Two half-turn loops form a single turn spiral connecting two capacitors in series as illustrated in Fig. 1.3A to form what is known as a Marx-generator coil. This configuration yields an azimuthal voltage drop around a complete loop equal to twice the voltage on each capacitor. Increases in the initial azimuthal voltage drop lead to substantially increased current rise rates and, consequently, more impermeable current sheets relative to earlier PIT designs. In the PIT, the Marx-generator configuration is repeated nine times to yield the coil shown in Fig. 1.3B.

Even employing the Marx-generator configuration, the PIT must operate at relatively high charge voltages (15 kV per capacitor) and discharge energies (4 kJ per pulse) to ensure complete inductive breakdown of the propellant. The high voltages and associated high current rise rates and peak current levels place very stringent constraints on the types

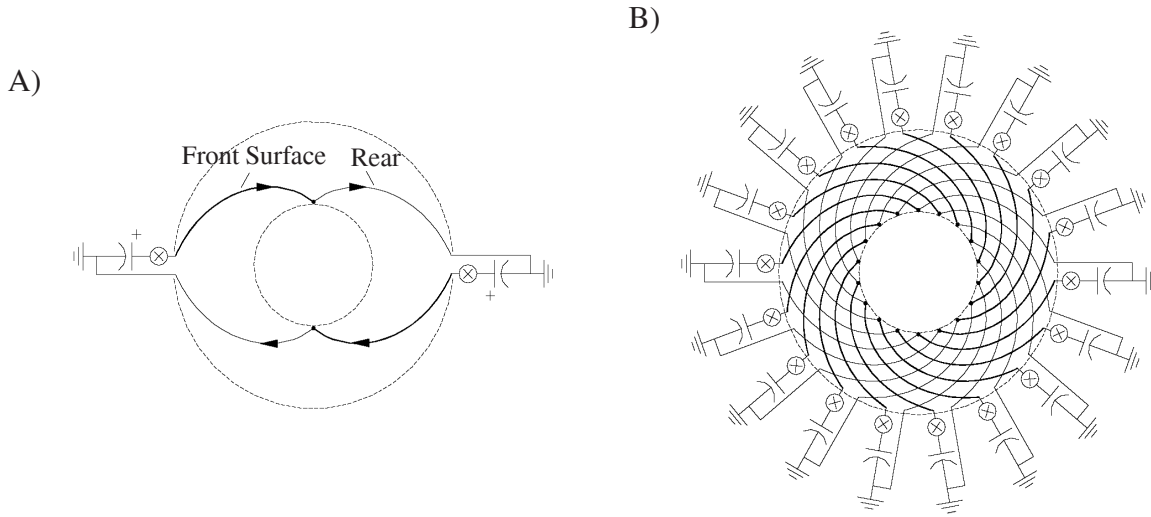


Figure 1.3: Marx generator PIT coil configuration. A) One complete loop of a half-turn Marx generator. B) The nine complete loops comprising the PIT MkV. (from Ref. [1]).

of switches that can be employed. Additional complexity arises from the fact that the switches connecting each of the 18 capacitors to their portion of the circuit must be closed simultaneously to ensure uniformity of the discharge over the coil surface. Moreover, the Marx-type coil, which possesses a low inductance (and very little potential acceleration) at small diameters, must be large in order to maintain an electromagnetic acceleration stroke of appreciable length relative to the gas depth thickness ($\sim 7\text{-}10$ cm). These constraints make it quite difficult to scale the PIT concept to smaller sizes.

Before moving on, we list additional findings and lessons distilled from the history of PIT development, which is reviewed in Appendix A.

- The current in the inductive current sheet is primarily conducted by electrons.
- Axial acceleration of the current sheet is primarily accomplished by the polarization electric field which arises due to charge separation.
- Uneven gas distributions can detrimentally affect current sheet formation and propellant sweeping efficiency.

- Increasing the ratio $\Delta L/L_0$ increases thruster efficiency (Lovberg criteria).
- For a real mission, high-current switches and capacitors must be able to survive for 10^9 - 10^{10} shots while operating at a high repetition rates (50-100 Hz). These problems are compounded by the fact that the PIT operates at high charge voltages and discharge currents, which additionally strain the system.
- Since it is a pulsed device, the PIT can maintain constant I_{sp} and thrust efficiency, η_t , at arbitrary levels of input power, while repetition rate and average thrust scale directly with input power.

1.3 FARAD Concept

In this dissertation, we introduce a new pulsed inductive plasma accelerator concept, the **F**araday **A**ccelerator with **R**adio-frequency **A**ssisted **D**ischarge (FARAD)[6, 7]. The concept was first proposed by E. Choueiri in 2002. A schematic representation of the FARAD proof-of-concept experiment constructed for the present work is shown in Fig. 1.4. In the schematic two joined cylindrical glass tubes form a vacuum chamber for the experiment. Plasma generation occurs in the smaller vessel while acceleration takes place in the larger-diameter, adjoining vessel. The chamber is surrounded by a set of applied B -field electromagnet coils, which are configured to produce a highly axial field inside the smaller tube and a highly diverging, mostly radial field near the flat back-end of the larger vessel, as shown by the representative applied B -field lines drawn in the figure.

In a FARAD thruster, gas is injected into the smaller tube (from the left of the picture) and is ionized by a radio-frequency (e.g. helicon) discharge, which requires the applied axial magnetic field and an RF/helicon antenna; the latter is shown wrapped around the outside of the smaller tube. A helicon discharge[8]-[10] is a radio-frequency inductive

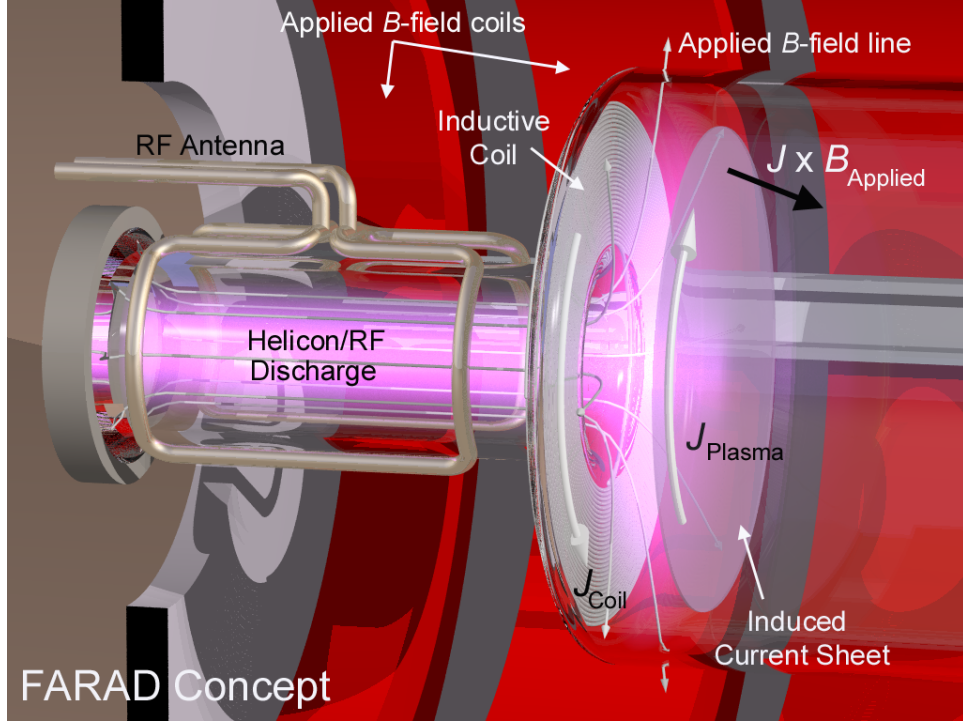


Figure 1.4: Schematic illustration of the FARAD concept.

discharge that is very efficient as a plasma source. The ionized plasma (ionization fraction $\geq 10^{-3}$ at 1 kW) is guided by the applied magnetic field to flow radially outward along the flat back-end of the adjoining larger vessel.

A flat inductive coil is mounted on the outer side of the back-end (which protects the coil from the plasma). The coil extends from the outer radius of the central opening to the inner radius of the larger vessel and is referred to as the acceleration stage. A large azimuthal current, labeled J_{Coil} in Fig. 1.4, is quickly pulsed through the coil. For a high-enough current rise rate[2], $dI/dt \geq 10^{10} \text{ A/(cm s)}$, this pulse induces a current sheet in the plasma, which initially forms parallel and very close to the back-end.

The current sheet, shown as a thin disk in the figure, contains an induced azimuthal current, labeled J_{Plasma} , which flows in the opposite direction to the current in the coil. The induced current density interacts with the magnetic field (both the induced and applied

components) resulting in a Lorentz body force which accelerates the current sheet. The sheet entrains any additional gas it encounters and subsequently expels the propellant at high exhaust velocity to impart impulsive thrust to the spacecraft.

Advantages and Motivation

The FARAD concept shares one main feature with the PIT[3, 4, 11], namely the inductive production and acceleration of a current sheet via a current pulse in an external coil. As such, we expect the propulsive characteristics of a FARAD thruster in which the circuit and accelerator have been optimized to be quite comparable to the PIT ($I_{sp} = 2000\text{-}8000$ s, $\eta_t = 40\text{-}50\%$ when operating under similar conditions with the same propellant).

The novelty of the FARAD is that the plasma is preionized by a mechanism separate from that used to form the current sheet and accelerate the gas. This is much different than the PIT where ionization, current sheet formation and acceleration are all performed by the pulse of current flowing through the acceleration coil. As observed in the previous section, this leads to a large device (1 m diameter) which requires high discharge voltages (15 kV) and energies (4 kJ/pulse). However, as speculated in the first of the two quotes cited at the end of section 1.1, a design like FARAD that uses preionization may be able to achieve a sufficiently rapid breakdown for efficient operation without requiring the very high voltages and discharge energies found in the PIT. Furthermore, early data from PIT predecessors (discussed in Appendix A) indicate that preionization will, in certain cases, have a positive effect on thruster performance[12, 13]. Relief of the high energy, high initial voltage design constraint makes it possible to construct FARAD thrusters that are inherently much more compact than the current PIT design. Also, it is envisioned that FARAD will operate using only one capacitor bank and switch. Even with the added complexity of the preionization stage in FARAD, this greatly simplifies the system relative to the 18 separate capacitors

and switches found in the PIT.

Another conceptual difference between the FARAD and the PIT is that in the FARAD the propellant is fed as a plasma from upstream of the acceleration stage and passively guided by the applied magnetic field, rather than as a neutral gas fed from downstream by a sizeable nozzle (greater than 30 cm in diameter) that intersects the inner part of the accelerated plasma flow. Finally, in addition to the acceleration produced by the interaction of the induced magnetic field and plasma current, an acceleration component may be realized through the interaction of the applied magnetic field with the induced current. A strong applied magnetic field may, however, impede the azimuthal current in the sheet, thus lowering thruster efficiency. Study of this aspect of the FARAD is beyond the scope of this dissertation, but we mention it here as it may merit separate investigation.

FARAD also offers several advantages over other existing electric propulsion concepts:

- FARAD is completely electrodeless. Both the RF antenna needed for the helicon source and the pulsed acceleration coil are not in contact with the working fluid. This mitigates the lifetime issues associated with electrode erosion (chemical reactions and sputtering, as well as spot-attachment induced melting and evaporation of electrodes) in electric thrusters.
- The FARAD concept is compatible with a wide variety of propellants since plasma-electrode interaction is not an issue. Water vapor, for instance, may prove to be a viable propellant (although its use in helicon discharges has not been explored). Ne, Ar, He, Kr, H₂, SiH₄, O₂, Cl, F and Xe have all been used successfully in helicon sources.
- The separation of the ionization and acceleration stages, the ionization efficiency of the helicon source, and the reliance on the magnetic field to guide and supply the working plasma to the acceleration stage should result in a significant decrease of

the fraction of neutrals in that stage. This should translate into high mass utilization efficiency.

- Since it is a purely electromagnetic accelerator, FARAD does not suffer from the space charge limitation of electrostatic devices (which limits the thrust density) nor is it subject to the exhaust velocity limitations inherent to electrothermal devices (due to the requirement of tolerable thermal fluxes).
- FARAD is an inherently pulsed device. Therefore it has the advantage of operating at a finite duty cycle from an arbitrarily low steady-state power and can thus, conceptually, be used on both high-power and low-power spacecraft while still maintaining constant I_{sp} and η_t .

1.4 Dissertation Scope and Outline

The motivation of this dissertation is explore the physical mechanisms present in the FARAD through a series of experimental and numerical studies aimed at developing physical insight which can be used to guide the design of a FARAD-based thruster. Specifically, we aim to accomplish the following three goals:

- Demonstrate the main features of FARAD through a proof-of-concept experiment.
- Obtain insight into the physical processes found in FARAD.
- Develop design criteria that will help evolve the proof-of-concept experiment into an optimized thruster.

The outline of the remainder of this thesis is as follows. In the next chapter the FARAD proof-of-concept experiment is described in detail while the diagnostics employed are dis-

cussed in chapter 3. The data collected from the proof-of-concept experiment are presented, analyzed and summarized in chapter 4. An existing inductive acceleration model is non-dimensionalized in chapter 5 for the purpose of providing physical insight into the operation of pulsed inductive accelerators. The model is also used to further interpret the experimental results from chapter 4. Finally, we conclude with a series of design rules for constructing an optimized FARAD thruster, which are distilled from the findings of this thesis.

Chapter 2

FARAD Proof-of-Concept Experiment

The different components of the FARAD proof-of-concept experiment (POCX) are described in this chapter. These components are assembled to form the FARAD POCX apparatus in a dedicated experimental facility as shown in Fig. 2.1.

2.1 Vacuum Vessel

The vacuum vessel consists of two Pyrex cylinders placed inside an electromagnet. The small cylinder has a 6 cm inner diameter and is 37 cm in length while the large cylinder has a 20 cm inner diameter and is 46 cm in length. The cylinders are connected using a G-11 (fiberglass) plate with a 6 cm concentric hole at the center to allow free flow of gas between the two cylinders. A flat induction coil (used to accelerate the plasma) is mounted to the G-11 plate inside the vacuum chamber. A photograph of the small cylinder mated to the G-11 plate is shown in Fig. 2.2.

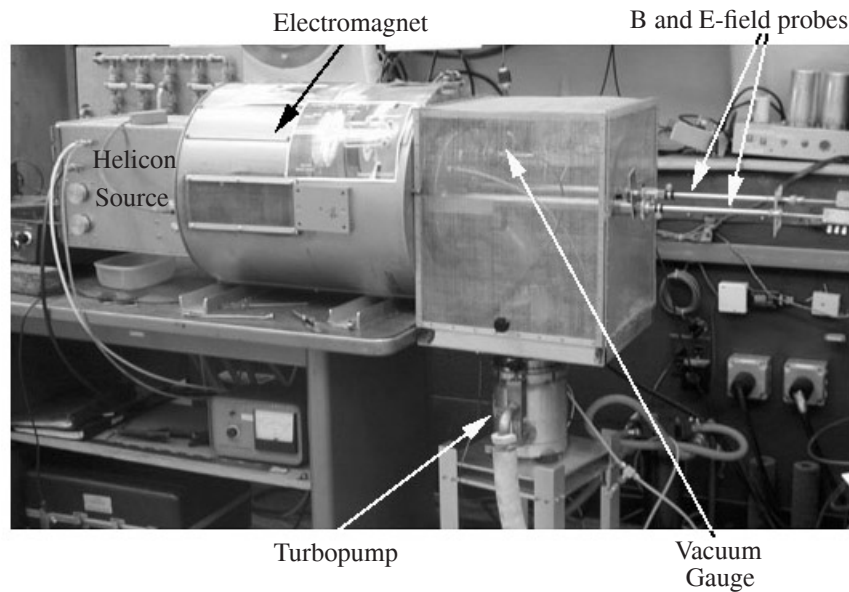


Figure 2.1: Photograph of the facility used for the FARAD POCX. The picture shows the water-cooled electromagnet, Faraday cage, turbopump and associated equipment. The plasma helicon source is located inside the box on the left hand side.

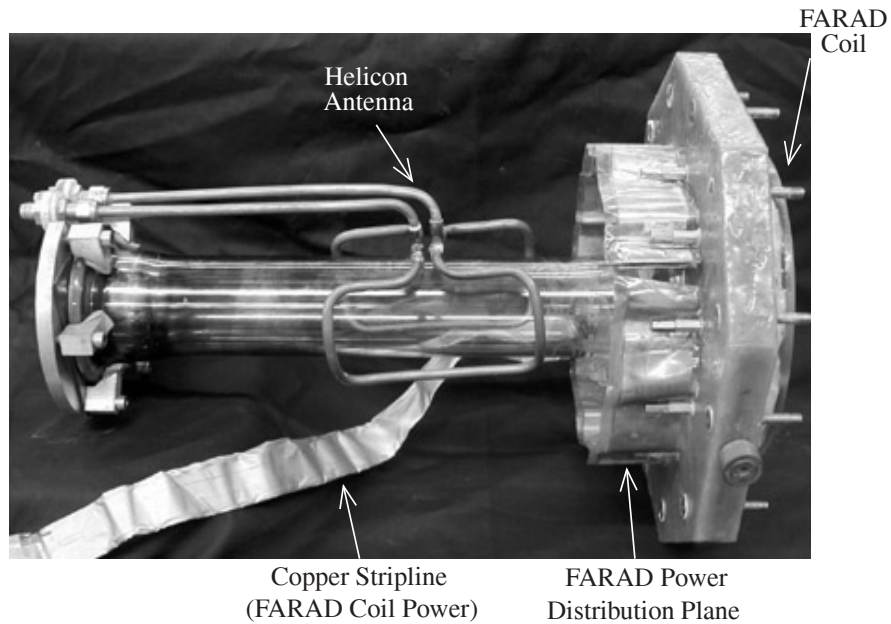


Figure 2.2: Side view of the fully assembled FARAD POCX. This photograph can be compared directly to the conceptual schematic shown in Fig. 1.4.

The chamber is evacuated using a 150 l/s turbo pump backed by a roughing pump. The base pressure with no active gas flow is 5×10^{-6} Torr. A constant background pressure (0.1 to 55 mTorr) can be maintained by injecting gas through a feed located at the endplate of the large cylinder while simultaneously evacuating the chamber through a conductance controller located in the vacuum line just upstream of the turbo pump. All experiments presented in this dissertation were performed using argon.

2.2 Applied Magnetic Field

The applied magnetic field is generated using a Varian VA-1955A klystron magnet. As the present work is a proof-of-concept experiment, no effort has been made at this stage to develop a compact magnet that would be more ideal for an actual thruster. This apparatus contains five separate, water-cooled magnet coils (see schematic in Fig. 2.3). The magnet wiring has been altered to allow the currents in coils 1 and 2 and coils 3, 4 and 5 to be driven in opposite directions by two different power supplies. Using two Electronic Measurements EMCC 120-40 power supplies to drive the current in opposite directions in these coil sets, a cusped magnetic field can be created.

2.2.1 Magnetostatic Model

A 2-D axisymmetric numerical model of the magnet and case is constructed and solved using a magnetostatic modeling program (Maxwell SV, Ansoft Corp.). The model is shown to scale in Fig. 2.3. Each coil set consists of three separate, concentric, toroidal copper rings. Each ring carries an equal amount of the total assigned current. The magnet casing is modeled with a relative magnetic permeability of 60. As in the experiment, the currents in coil sets 1 and 2 flow in the same direction while coil sets 3, 4 and 5 are driven by a

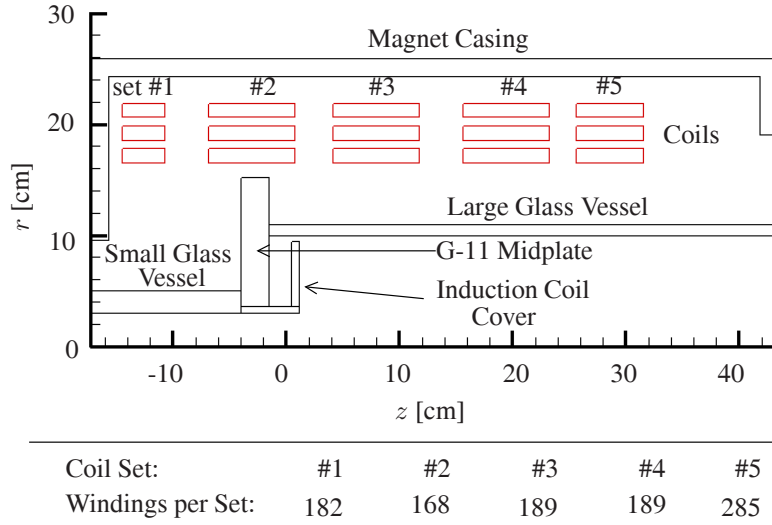


Figure 2.3: An axisymmetric schematic depicting the geometry of the magnet and vacuum vessel (to scale). The acceleration coil is located at $z = 0$ in all plots in this dissertation.

separate power supply in the opposite direction. Throughout this dissertation, the axial position $z = 0$ is coincident with the location of the acceleration coil.

2.2.2 Applied Field Calibration Measurements

Measurements of the steady-state magnetic field in the coil were performed before the vacuum vessel was installed using an FW Bell gaussmeter (model 5080) calibrated to an accuracy of 1%. These calibration measurements are used to validate the magnetostatic model. The axial and radial components of the field were measured on a grid with spacings in both the axial and radial directions of 1.27 cm (1/2"). This grid covers approximately 10 cm (4") in the radial direction and 58 cm (23") in the axial direction. The current provided by the power supply for coils 1 and 2 was 23.9 A while the current for coils 3, 4 and 5 was 10.2 A (e.g. coil set #1 = 23.9 A \times 182 turns = 4350 A-turns). The results of the applied field measurement are given in the top half of Fig. 2.4 while the bottom half of the same figure shows results predicted by the magnetostatic model operating under the same conditions. The agreement with the model is excellent with an average difference between

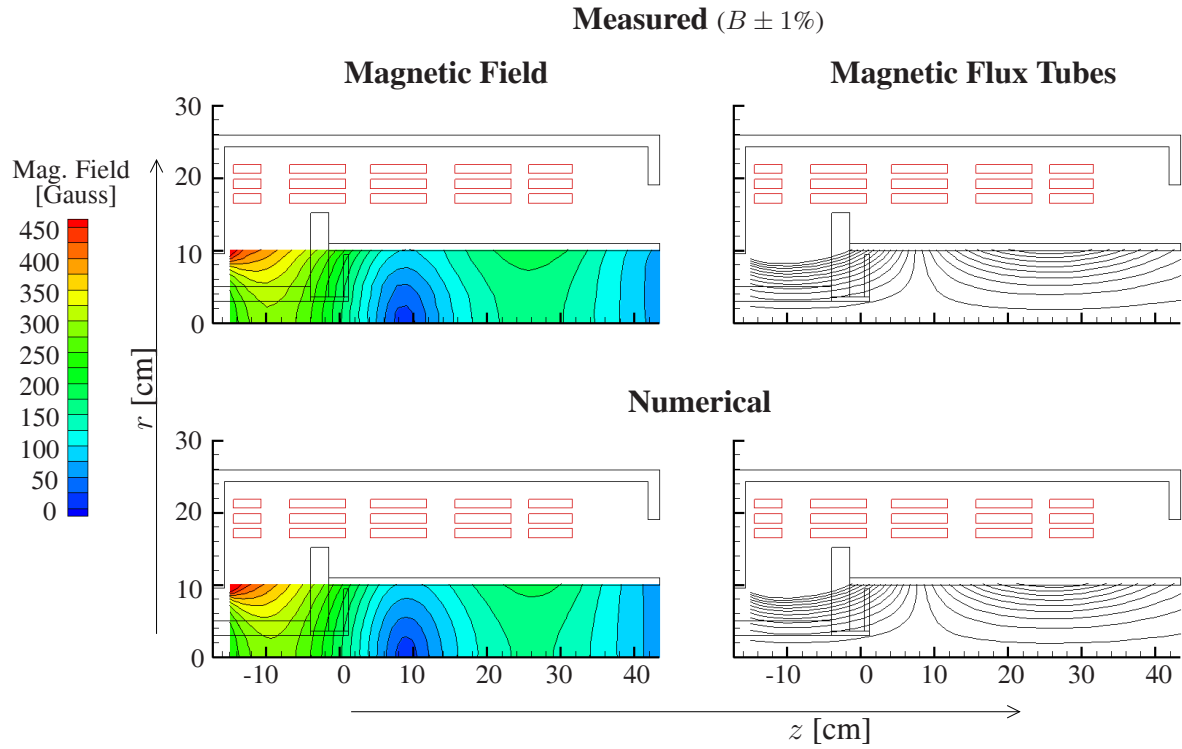


Figure 2.4: Applied magnetic field measurements (top) and modeling results (bottom) for the calibration case where the current in coils 1-2 is 23.9 Amps and the current in coils 3-5 is 10.2 Amps. The agreement is within a few Gauss.

the measured and calculated values at each grid point of less than 5 Gauss and a maximum difference of 12.5 Gauss.

2.2.3 FARAD Applied Field Design

The magnetostatic model is used to identify the distribution of coil currents which yield a mostly radial field at the coil face while still producing a mostly axial field in the helicon stage. For the given configuration, there are a wide range of current values for which an axial field is produced in the helicon stage. Plots of the magnetic field lines are used to identify field geometries which could deliver magnetized particles from the inductive discharge to the acceleration coil face. While a cusp magnetic field is produced in the

proof-of-concept experiment, it is an undesirable consequence of how the applied magnetic field is presently generated. Only the axial field in the helicon stage and the mostly radial field in the acceleration stage are truly necessary.

2.3 Plasma Generation

A Boswell-type saddle antenna (helicon antenna)[14] is placed around the small cylinder (shown on the left side of Fig. 2.2) and used to generate the plasma. The antenna is constructed of copper tubing to allow water cooling during operation. The helicon discharge[8]-[10] is produced by supplying power (steady-state or pulsed) to the antenna from an ENI 13.56 MHz, 1.2 kW power supply through a tuner. The tuner consists of an L network composed of two Jennings 1000 pF, 3 kV variable vacuum capacitors (see circuit schematic in Fig. 2.5, where L_a is the antenna inductance, R_p is the plasma resistance and M is the mutual inductance between the antenna and the plasma). It is located as close to the antenna as possible to maximize coupling efficiency.

The plasma source was operated at power levels between 500 W and 1 kW. At these power levels, the measured plasma density, electron density, electron temperatures, reflected powers[15] as well as the luminous structure of the plasma inside the source (a

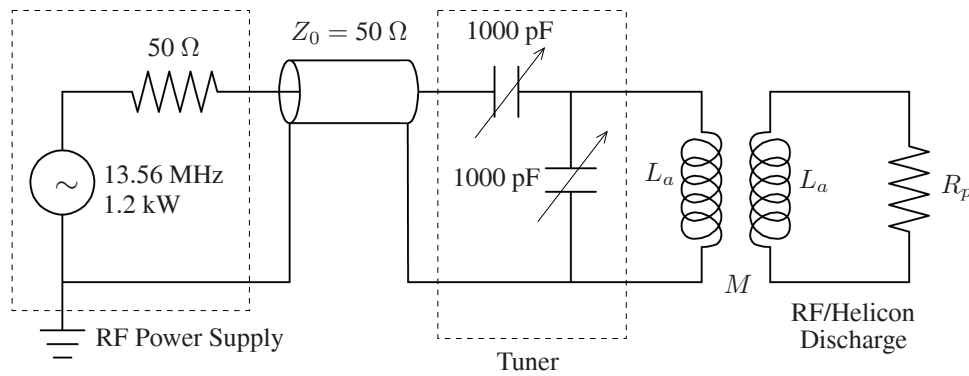


Figure 2.5: Circuit schematic of the RF/helicon discharge plasma generation stage.

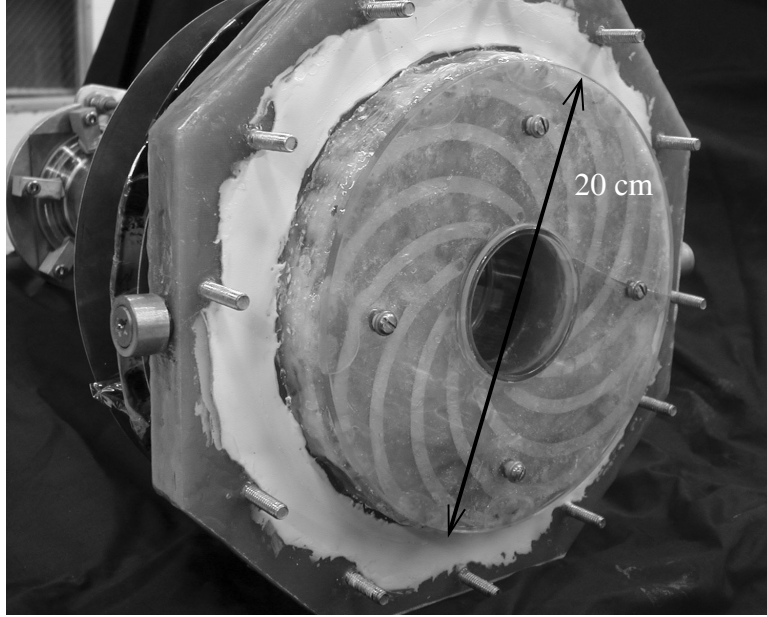


Figure 2.6: Skewed end view of the fully assembled FARAD experiment showing the face of the acceleration coil.

pencil-like core of bright emission surrounded by plasma) are representative of a helicon source as described in the literature (see Ref. [9] and the references within) as opposed to an inductive discharge. Helicon discharges were ignited at axial field strengths in the small cylinder ranging from 175-400 Gauss.

2.4 Acceleration Coil

The FARAD acceleration coil (seen in Fig. 2.6) is similar to the Marx-type coil used by Dailey and Lovberg in later generations of the PIT[3]. However, it is quite different in scale and pulse energy. The PIT MkV coil is comprised of 18 half-turn coils, has an outer diameter of 1 meter and operates at roughly 4 kJ/pulse. The FARAD POCX, on the other hand, possesses 12 half-turn coils, has an outer diameter of 20 cm and has been operated from 44 to 78.5 J/pulse.

The half-turn coils are connected in parallel using copper strips. A 39.2 μF capacitor is

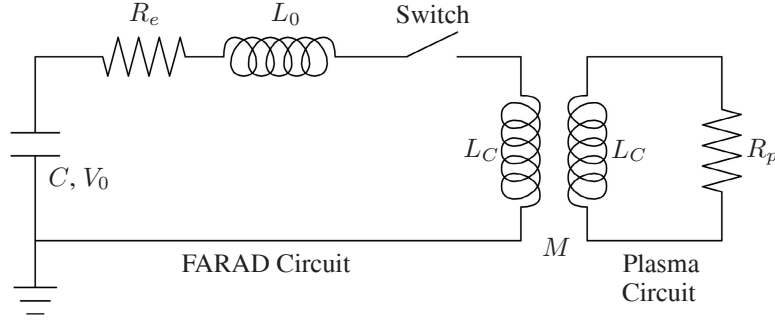


Figure 2.7: Circuit schematic of the FARAD acceleration coil and the inductively coupled plasma.

remotely located and connected to the coil using copper stripline. Current is switched using a simple contact, or “hammer”, switch. In a real thruster, SCRs or some other type of solid-state switching would be used. A lumped-element circuit schematic of the acceleration stage, showing both the driver circuit and the inductively coupled plasma, is shown in Fig. 2.7. The external circuit possesses capacitance C , external inductance L_0 , resistance R_e , and acceleration coil inductance L_C . The plasma also has an inductance equal to L_C and a resistance R_p . The two circuits are inductively coupled through the acceleration coil, which acts as a transformer with mutual inductance M .

In a real thruster, one would want the fractional change in inductance to be high ($\Delta L/L_0$ greater than 1). The value of $\Delta L/L_0$ is approximately equal to 15% in our proof-of-concept experiment. This is an unfortunate effect of adopting the PIT’s half-turn Marx-type coil geometry, which possesses a low inductance at small diameters. However, demonstrating current sheet formation and *any* subsequent acceleration in this unoptimized configuration, rather than optimizing thruster performance, is the goal of the POCX.

2.5 Experimental Operation

During operation of the FARAD POCX, a helicon plasma is initiated and allowed to reach a steady-state condition. The duration of the helicon discharge prior to pulsing the acceleration coil is ~ 1 -2 secs. The helicon source remains active well after the acceleration pulse ($\mathcal{O}(1-10) \mu\text{s}$) is complete.

In a real thruster, the propellant feed system and the helicon discharge would operate in a pulsed mode along with the acceleration pulse. It is clear that the length and inter-sequencing of these three pulsed systems will have a significant impact on both the mass utilization efficiency and the propulsive performance of a thruster. We shall discuss the issues associated with optimization of these pulsed systems in Chapter 6.

Chapter 3

Experimental Diagnostics

This chapter gives details regarding the various diagnostics used to obtain quantitative and qualitative information on current sheet formation and acceleration in the proof-of-concept experiment.

3.1 Current Monitoring

The current flowing through the acceleration coil, J_{Coil} , is monitored using an air-core Rogowski coil. Since they don't rely on ferrite cores, Rogowski coils are not susceptible to magnetic field saturation. Consequently, miniaturized Rogowski coils can be constructed that are capable of measuring very high levels of current (> 10 kA). This makes them ideal for integration into small, compact pulsed-power experiments since they do not greatly alter the circuit inductance of the experiment, leading to relatively unchanged current waveforms (see Ref. [16] for an example of an integrated Rogowski coil).

Rogowski coils, like the one shown schematically in Fig. 3.1, consist of a single wire which is first made to form a circle. The wire then winds back along the initial circular path, forming a torus having minor radius r_m and major radius r_M .

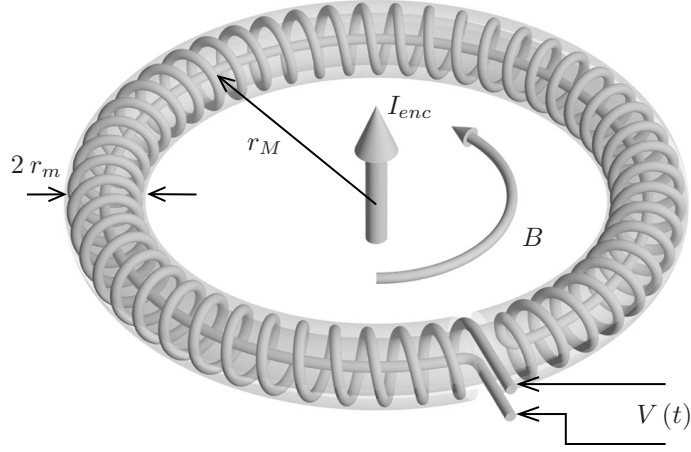


Figure 3.1: Schematic of a Rogowski coil.

The full theory of Rogowski coil operation is detailed in Refs. [17, 18]. Any current enclosed by the torus, I_{enc} , induces an azimuthal magnetic field, B , as shown in the figure. If the magnetic field is time-varying, it induces a voltage drop across the coil terminals, $V(t)$, which is proportional to dI_{enc}/dt . The current can be obtained by integrating the voltage waveform and multiplying by a calibration constant, a :

$$I_{enc}(t) = a \int_0^t V(\tau) d\tau. \quad (3.1)$$

In our experiments the voltage across the coil is recorded using a fast oscilloscope operated at 100 megasamples/sec and integrated numerically in post-processing to yield a measure of the current in the acceleration coil.

The raw coil output also served a second purpose in these experiments. Synchronizing equipment and diagnostics with the current pulse is typically not trivial in a pulsed experiment. However, this did not prove to be difficult in the present study since the Rogowski coil provides a unique trigger signal in the form of an initial jump in the coil voltage (caused by the initially high dI/dt level in the experiment). This signal is used to trigger all oscilloscopes and cameras used in the present study.

3.2 Voltage Probe

Measurement of the time-varying voltage on the capacitor bank is performed using a Tektronix P6015A high-voltage probe. This probe is frequency compensated, having a bandwidth of 75 MHz. Its output is attenuated by a factor of 1000, yielding a measure of the capacitor voltage (up to 2 kV in the present experiment) that can be displayed and recorded by a fast oscilloscope.

3.3 Magnetic Field Probes

The induced (time-varying) magnetic fields found in the experiment are measured using B -dot probes. This method has been employed extensively to measure magnetic fields in pulsed plasma thrusters[19] and is applicable to a wide range of temporally varying plasma physics phenomena[20]. The theory of operation for B -dot probes is discussed in Ref. [21].

There are two major constraints on the construction of the probes used in our experiments. They had to be small compared to the diameter of the acceleration coil to yield good spatial resolution in the measurement. Also, the probe had to be constructed such that the field was measured simultaneously in three orthogonal directions. These measurements would later be linearly combined to obtain $B(t)$ in the r - θ - z coordinate system of the acceleration coil.

A photo and circuit schematic of the balanced B -dot probes used in this study are shown in Fig. 3.2. The heads consist of Panasonic 220 nH wire-wound non-magnetic core surface mount (chip) inductors similar to that used in Ref. [22]. The probe head is contained within a glass tube which protects it from the plasma. The tube diameter is on the order of a mm, so as to not significantly disturb the plasma. Following Ref. [20], the circuit is balanced by connecting the probe heads to the outer taps on 1:1 center-tap transformers using twisted

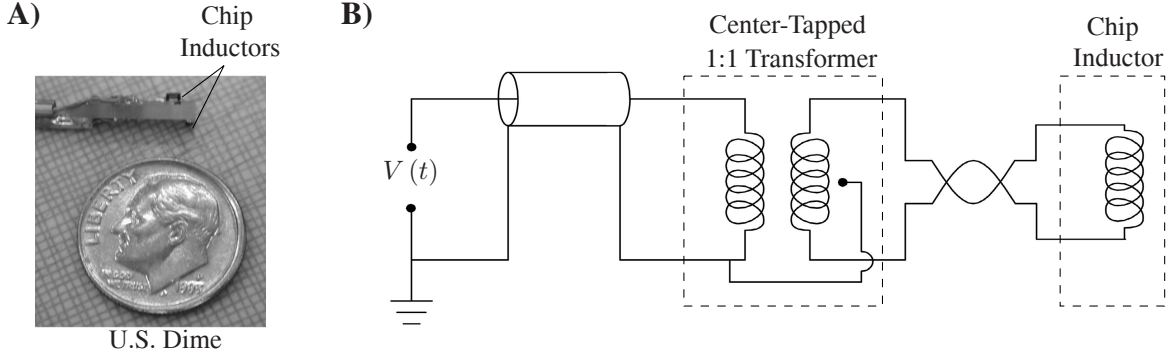


Figure 3.2: A) Photograph of the B -dot probe head. B) Circuit schematic of a balanced B -dot probe.

wire pairs while the center taps on the probe side of the transformer are grounded. Circuits balanced in this manner have been shown to offer excellent common-mode signal rejection. The probes are calibrated by placing the head in the center of a Helmholtz coil in a manner similar to that used by Markusic[23].

The probe outputs (voltages) are proportional to dB/dt and are recorded using a fast oscilloscope. These signals are integrated to yield the time-dependent magnetic field:

$$B(t) = \int_0^t c(\omega) V(\tau) d\tau, \quad (3.2)$$

where $c(\omega)$ is a frequency-dependent proportionality constant (calibration constant). The probes constructed for these experiments have a constant frequency response within the experimental range of interest, from 30 kHz to 2 MHz. Magnetic field data are acquired at axial stations spaced 5 mm apart at a radius of roughly 66 mm (see Fig. 3.3 for the relative radial position of the field measurements).

3.4 Imacon Fast-Framing Camera

Visualization of current sheet formation and its subsequent motion is accomplished using a Hadland Photonics Imacon 792/LC fast-framing camera. The photographs are obtained

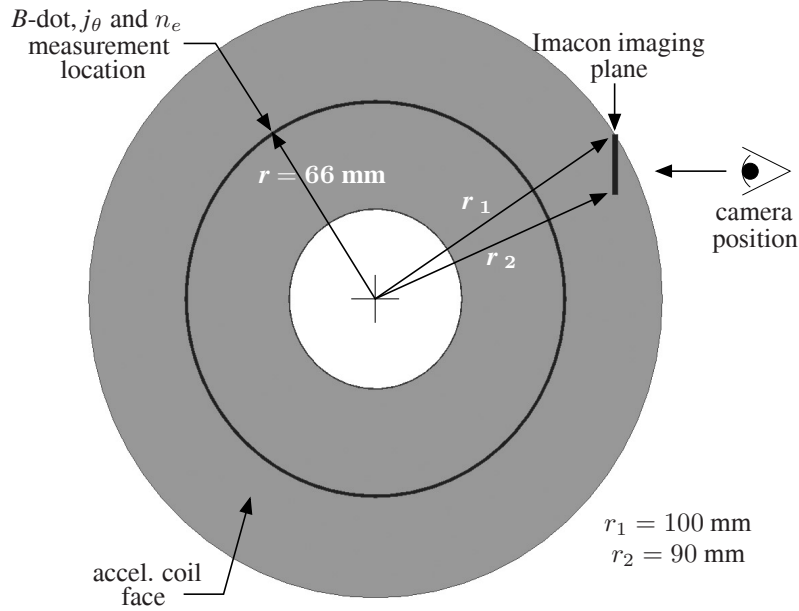


Figure 3.3: A schematic showing the relative locations of 1) the magnetic field and Langmuir probe data and 2) the plane imaged by the fast-framing Imacon camera. The schematic is to scale and the vertical extent of the imaging plane matches the extent of the images presented in this dissertation.

using a 20 million frames per second module, with each frame having an exposure time of 10 ns. Images are captured on Polaroid film, which is subsequently scanned into a computer for digital image analysis.

The imaging is useful to show the spatial and temporal evolution of the discharge. Due to obstructions in the optical path only one region of the plasma, located on the face of the acceleration coil and extending 20 mm in the vertical direction, is imaged. A mask is affixed to the outside of the vacuum vessel to allow the current sheet's absolute position to be determined in each exposure. Consequently, the imaging plane is located at the edge of the vacuum vessel to properly image the mask (see Fig. 3.3 for the relative location of the imaging plane).

The photographs are obtained without the use of narrow linewidth filters, so any light emission that is bright enough to be imaged is seen. However, the RF/helicon plasma that

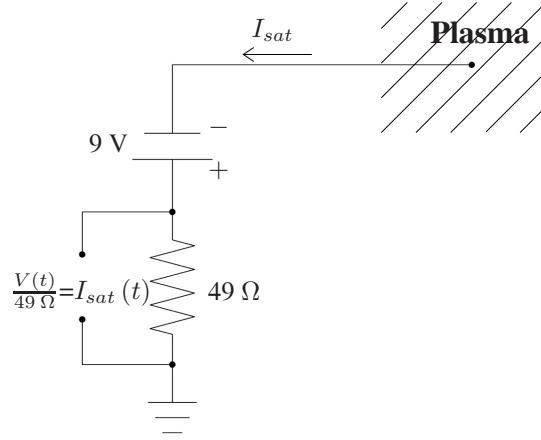


Figure 3.4: Langmuir probe circuit used to measure the ion saturation current.

reaches the acceleration coil face did not produce enough light on its own to appear in any of our photographs, so we take the light captured in each exposure to correspond to the emission from the current sheet.

3.5 Langmuir Probes

A single Langmuir probe is used to measure the relative plasma density in the FARAD current sheet. It is necessary to probe the plasma directly since a dense plasma may exist in regions that are not carrying current (and not inducing magnetic fields that can be measured using B -dot probes). In the POCX, we are only using the Langmuir probe to track regions of high plasma density; we are not making any quantitative measurement of n_e .

The circuit schematic of the Langmuir probe used to measure the ion saturation current, I_{sat} , in the proof-of-concept experiment is shown in Fig. 3.4. The measurement of the voltage drop across the $49\ \Omega$ resistor was performed using a frequency-compensated voltage probe. In addition, a separate measure of the floating potential was made using the same frequency-compensated voltage probe terminated into a high impedance.

It should be noted that Langmuir probes are not typically the ‘best’ method for directly

measuring the time-varying number density in a plasma. It is an intrusive technique and any quantitative data that can be extracted typically possesses error bars greater than 50% for a variety of reasons. Laser interferometry, which is non-intrusive, provides a far more accurate and reliable measurement. This measurement was attempted in the FARAD using a two-pass helium-neon laser interferometry system (the same system that was employed for measurements presented in Refs. [19, 23]) and we were able to measure the maximum plasma density in the sheet to be about $7 \times 10^{14} \text{ cm}^{-3}$. However, this density is at the very edge of the system's resolution, so no further, time-resolved measurements could be attained.

As the probe is biased sufficiently negative, it repels all electrons and collects only ions (ion saturation current regime). The equation relating the number density to the ion saturation current collected by a cylindrical probe is[24]

$$I_{sat} = \exp\left(-\frac{1}{2}\right) e A_p n_e \sqrt{\frac{k T_e}{m_i}}, \quad (3.3)$$

where e is the charge of an electron and A_p is the surface area of the probe. Notice that the ion saturation current is dependent on both n_e and T_e . Typically, the probe voltage is swept through a range and the resulting I - V curve can be analyzed to determine both plasma parameters. However, Eq. (3.3) was derived under several assumptions, a number of which may be simultaneously violated in FARAD (as well as any high-current, self-field, pulsed plasma accelerator). The major assumptions include:

1. Non-magnetized plasma,
2. Cold ions ($T_i \ll T_e$),
3. Collisionless sheath around the probe tip,
4. Local thermodynamic equilibrium (LTE),

If the number density is computed based upon a measurement acquired using the circuit given in Fig. 3.4, then we are further assuming that the applied bias voltage is sufficient for the probe to reach the ion saturation limit. This assumption can be checked, in part, by monitoring the difference between the bias voltage and the floating potential. For the probe in Fig. 3.4 to yield accurate information regarding the absolute number density, V_{bias} must be significantly lower than V_{float} . When this condition is not satisfied (or even as V_{bias} approaches V_{float}), the errors on the number density measurement can grow even larger than those typically associated with Langmuir probe measurements. As for the other assumptions in the list above, calculations presented in chapter 4 show that the electrons are indeed magnetized in the current sheet when compared to the length scale of the probe. Also, measurements in other electromagnetic accelerators (PPTs[25] and MPDs[26, 27]) have shown that T_i can be on the same order T_e in high-current devices. Finally, the plasma density increases rapidly as the current sheet moves past the probe, implying higher collisionality and shorter collision length scales. In the next chapter, we'll present estimates of the relevant length and time scales in the proof-of-concept experiment and revisit the issue of whether the plasma is magnetized, collisional, or both.

An alternative probe technique, the triple probe, has been recently used for measurements in the plumes of pulsed plasma thrusters[28] and quasi-steady MPDs[29, 30]. Unlike standard Langmuir probes, the voltages on the probe tips of a triple probe do not have to be swept through a voltage range, making the triple probe more suited for pulsed thruster measurements. Unfortunately, triple probe theory is also limited by the same set of assumptions as single Langmuir probe theory[31].

Fortunately, an absolute measure of number density or electron temperature is not required for our purposes. The measurement technique described above (single, negatively biased probe) is sufficient to spatially and temporally track high density regions of plasma.

Chapter 4

Experimental Observations and Measurements

The data collected in the FARAD POCX are presented in this chapter. These data demonstrate the formation of a low-energy, low-voltage inductively-coupled current sheet. In addition, these data show that the sheet experiences significant acceleration during the first half-cycle of the discharge. Initial qualitative visual observations are presented first, followed by quantitative measurements presented in a series of sections corresponding to the various diagnostic techniques outlined in the previous chapter. We also vary the controllable parameters in the experiment to observe their impact on the accelerator's operation. The diagnostics, which were designed to resolve current sheet dynamics, expose the effects of various controllable parameters on the sheet's strength, speed and width.

Three different pulse energies were used in this study: 78.5, 60 and 44 J. The upper limit represents the rated voltage limit on the capacitor (2 kV). A discharge energy of 78.5 J was used for trials in which other parameters were varied.

The working gas for these data was argon. Three different background pressures were used: 7.5, 23 and 48 mTorr. The lower limit appears to represent a threshold below which

current sheet formation did not occur. The upper limit is near the pumping speed limit of the turbopump with the conductance controller in the fully restricted position. It was also more difficult to obtain a good match between the RF power supply and the inductively-coupled plasma at this higher pressure. A pressure of 23 mTorr was the baseline level in these experiments because the strongest current sheet formed at this pressure.

Two different applied magnetic field strengths were used. The baseline level represented the ‘stronger’ of the two fields. The ‘weaker’ field was one in which the current levels in the applied field coils were adjusted until they were half those used in the baseline configuration.

The helicon source was operated at 1000 W of forward power in these experiments. Tuning was adjusted or checked in every trial to assure that the best possible impedance match was being achieved. Typically, the reflected power was less than 10% of the total forward power. Measurements were performed for operation down to 500 W, but there were insignificant changes in the magnetic field waveforms and the photographic images at these helicon power levels.

A matrix of experimental conditions in the FARAD POCX is found in Table 4.1. The column labeled *Designation* gives the shorthand used throughout this chapter to differentiate between the various experimental operating conditions. The shorthand makes it easy for the reader to see if the discharge energy (E), ambient fill pressure (P) or applied magnetic field (B) is being changed relative to the base (also called the baseline) conditions. In addition, we can see whether the controllable parameters are increased (\uparrow) or decreased (\downarrow) relative to those found in the base condition. The radial component of the applied magnetic field, B_r , was calculated at $r = 66$ mm and is presented in Table 4.1. This radial position is coincident with the location of the induced field measurements.

The reported uncertainties are the combination of systematic and random errors in the

Table 4.1: Summary of the experimental conditions tested in the FARAD POCX. The up and down arrows indicate changes in the operating condition relative to the Base condition as defined in the text.

Designation	V_0 (E_0) [V (J)]	p_0 [mTorr]	B_r at $r = 66$ mm [Gauss]
Base	2000 (78.5)	23	160
E↓	1750 (60)	23	160
E↓↓	1500 (44)	23	160
P↓	2000 (78.5)	7.5	160
P↑	2000 (78.5)	48	160
B↓	2000 (78.5)	23	80

various measurement systems. All reported errors are within a 95% confidence interval, unless otherwise noted.

4.1 Circuit Measurements

4.1.1 Acceleration Coil Current

Typical driver circuit current waveforms are given in Fig. 4.1 for three pulse energies. These measurements represent the integrated waveforms obtained using the Rogowski coil described in Section 3.1. The peak current levels corresponding to pulse energies of 78.5, 60 and 44 J are 22.5, 19.5 and 16.5 kA, respectively. The corresponding maximum dJ_{Coil}/dt levels in the circuit are 1.8×10^{10} , 1.6×10^{10} and 1.35×10^{10} A/s. These levels all occur at time $t = 0$ and scale with the well-known relation

$$\left. \frac{dI}{dt} \right|_{t=0} \propto \frac{V_0}{L_0},$$

where V_0 is the initial voltage and L_0 is the initial inductance. The rise rates in the POCX are not great enough to induce a current sheet when there is no preionization present.

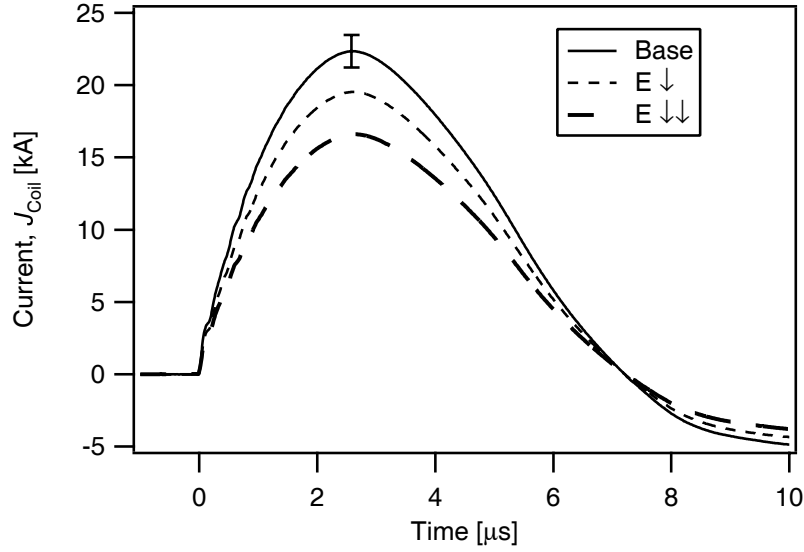


Figure 4.1: Total current in the acceleration coil, J_{Coil} , (with a typical error bar) for different pulse energies.

Absent from this section are figures showing the variation of the total discharge current with gas pressure or applied magnetic field strength. Since the fractional change in the inductance is low, the coil current is roughly the same with or without a current sheet present. Consequently, only changes in discharge energy appreciably affect the coil current.

4.1.2 Capacitor Voltage Measurements

Capacitor voltage waveforms for three different pulse energies are given in Fig. 4.2. Before time $t = 0$, the voltages are at the levels required to yield discharge energies of 78.5, 60 and 44 J (2000, 1750 and 1500 V, respectively). The waveforms in the figure all have the same features, noticeably ringing in the early stages of the discharge and then smoothing out as the voltage nears zero. The early ringing is indicative of reflections caused by impedance mismatches between the capacitor and the different circuit elements which comprise the transmission line and the load[32]. As in the case of the current waveforms, the voltage traces change in magnitude but not in shape with different pulse energies. The voltage

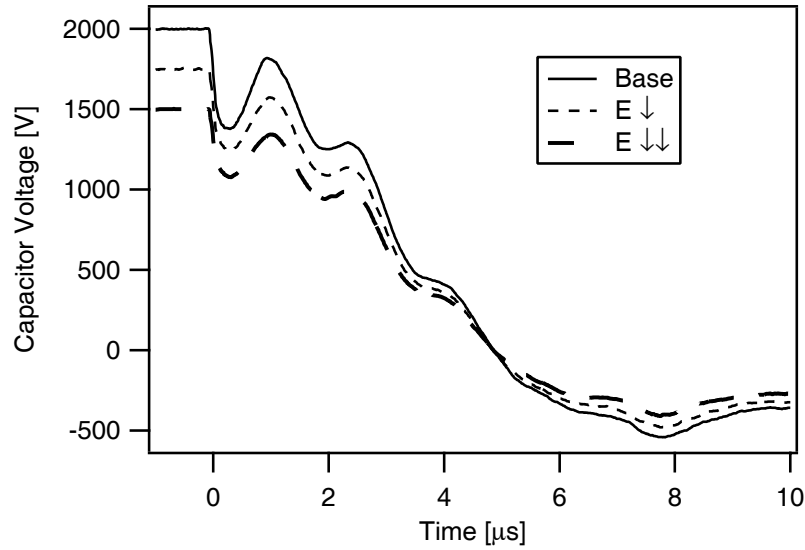


Figure 4.2: Voltage on the capacitor for different pulse energies.

waveforms for different ambient gas pressures or applied magnetic field strengths are essentially identical to those obtained for the baseline case.

Comparing figures 4.1 and 4.2, the question might arise as to why there is a high degree of ringing in the voltage waveform measurement but none in the current measurement. The voltage measurement is performed at the capacitor and, consequently, detects all the wave reflections returning to that point in the circuit. There are several locations between the capacitor and the load where the transmission line impedance suddenly changes (such as the transitions from 1) capacitor to stripline, 2) stripline to switch, 3) switch back to stripline) and any of these discontinuities in impedance can result in significant signal reflections propagating back toward the source. The current measurement, on the other hand, is performed very near to the inductive load (antenna) making it relatively immune to signal reflections.

4.2 General Visual Observations

Simple visual observations provided verification that some of the preionized plasma was passively guided onto the acceleration coil face. The helicon plasma is quite luminescent and can be seen following the applied magnetic field lines and spreading over the acceleration coil (see Fig. 4.3). We expect that electrons are magnetized and follow the applied magnetic field. The manner in which ions reach the face of the acceleration coil will be discussed in detail later in this chapter. The luminosity is greatest at the centerline of the device (not shown in the figure) and decreases with increasing radius. This is not surprising since the preionized plasma density should scale like $1/r$ as the plasma spreads radially outward across the accelerator coil face. The preionized plasma extends over a greater ax-

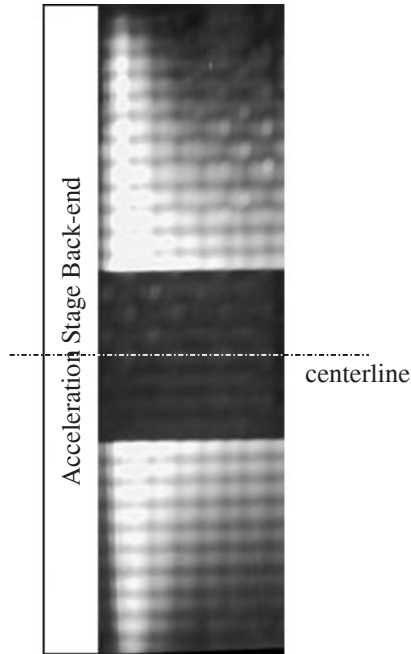


Figure 4.3: Photograph of the steady-state RF plasma as it follows magnetic field lines and spreads out over the face of the acceleration coil (viewed through a 1.0 neutral density filter). The bright area adjacent to the back-end, where the acceleration coil is located, is due to emission from the preionized plasma (no coil discharge in this picture). The grid pattern in the picture is due to the mesh of the Faraday cage enclosing the experiment and the dark, rectangular shape near the centerline is a structural member outside the chamber.

ial range and its luminosity decreases as the pressure increases, which is consistent with increased collisionality. A similar broadening and dimming is observed as the applied magnetic field is weakened, implying that the plasma is turned less effectively (i.e. transitioning from magnetized to unmagnetized electrons).

In the current configuration, in addition to the glowing region spreading over the acceleration face, a luminous column is seen expanding downstream along the centerline indicating that not all the plasma is turned. This issue would have to be addressed in a real thruster, where the unturned plasma would represent a propellant utilization inefficiency. In addition, the plasma density at the plane of the acceleration coil in a real thruster, while being greatest near the centerline, must be of sufficient magnitude at the outside edge of the coil to allow for current sheet formation and subsequent propellant acceleration over the entire coil face.

Visual observations provide evidence of current sheet formation. When current is pulsed through the acceleration coil, a very bright ‘flash’ of light appears in a thin region near the coil. The flash appears homogeneous over the face of the coil and its intensity temporarily overwhelms the light emitted by the steady-state (helicon) plasma. The short duration, bright light emission is indicative of additional excited state emission due to current sheet formation across the coil face. While these observations are only qualitative, it is important to note that no current sheet formation was observed when the preionized plasma was not present. This leads to the conclusion that the present B -field topology directed ‘enough’ preionized plasma to the acceleration coil face to allow for the formation of a current sheet at low discharge energies.

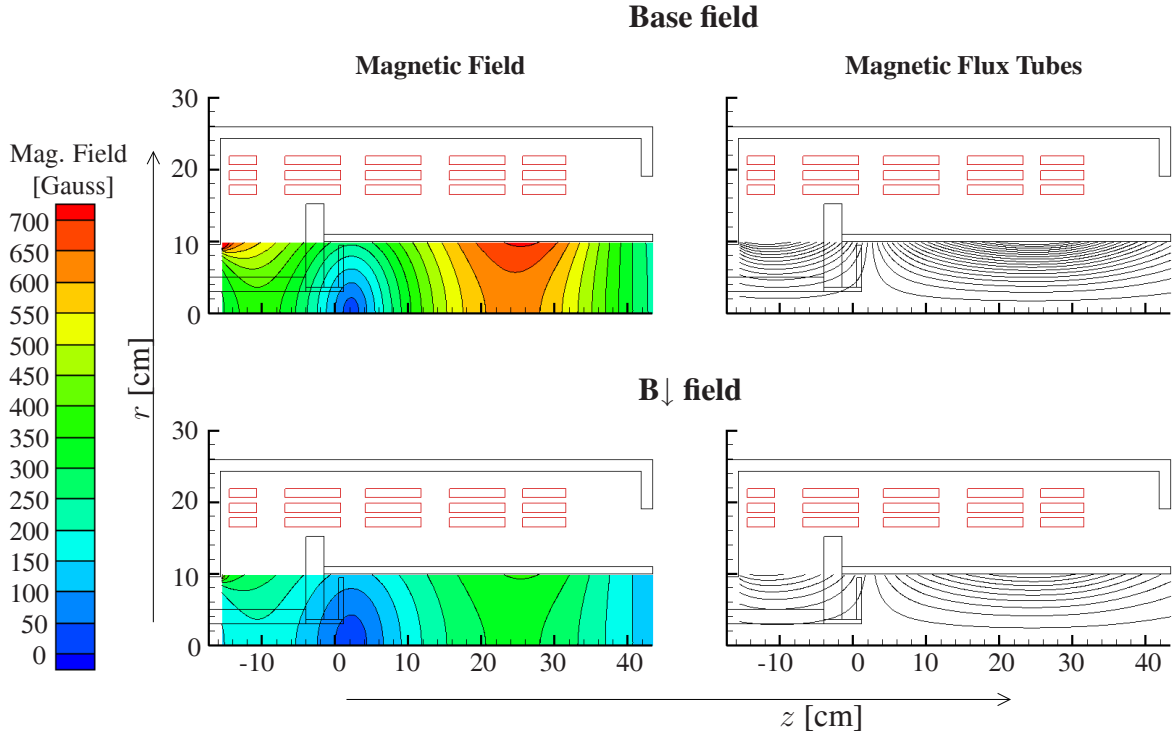


Figure 4.4: Results of applied magnetic field calculations for the baseline case (top) and the B_{\downarrow} case (bottom). The scales are the same for both sets of graphs.

4.3 Magnetic Field

4.3.1 Applied Field

Values of the applied (steady-state) magnetic field were computed numerically using the magnetostatic model presented in section 2.2.1. Plots of the applied field and resulting magnetic flux tubes for both the baseline and B_{\downarrow} field configurations are presented in Fig. 4.4. The scale is the same in both cases. In the baseline case, coils 1-2 are each supplied with 38 Amps of current while 36.5 Amps are delivered to coils 3-5. The current levels in the B_{\downarrow} case are half those in the baseline case. These currents match those used in the experimental trials.

In addition to Fig. 4.4, plots of the magnetic field components along an axial line located

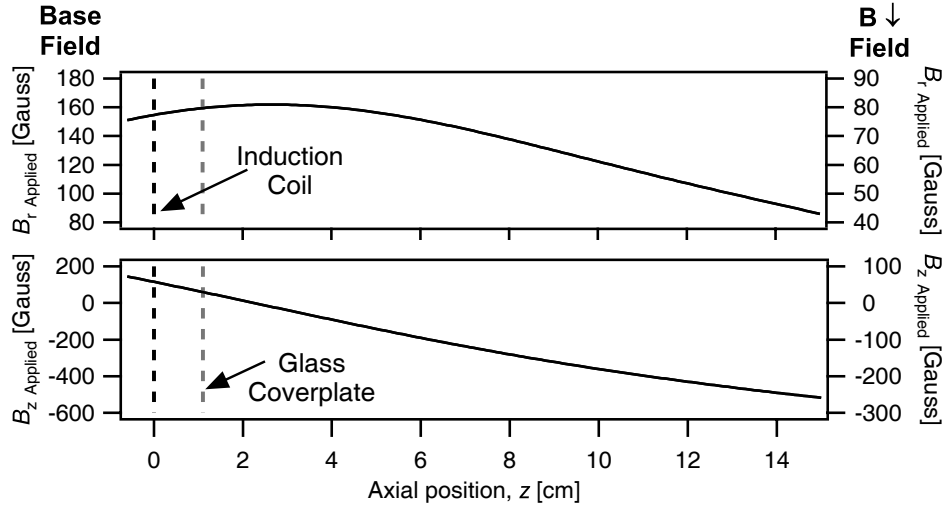


Figure 4.5: Calculated values of the radial and axial components of the applied magnetic field at a radius of 66 mm for both the baseline case (left axes) and B_{\downarrow} case (right axes).

at $r = 66$ mm are presented in Fig. 4.5. This radius corresponds to the position at which the B -dot and Langmuir probe measurements were obtained. The scales for the baseline field are located on the left side of each graph while those for the B_{\downarrow} field are on the right side. Note that the field strengths scale linearly with the coil current levels. Also, the radial component of the field, B_r , peaks just in front of the coil while the axial component, B_z , at that same location goes through zero, as expected.

4.3.2 Induced Field Measurements

The induced magnetic field is a combination of the fields emanating from the current in the acceleration coil and the current in the plasma sheet. Data showing the temporal and spatial variation of the induced radial field acquired at a radius of 66 mm are presented for different pulse energies (Fig. 4.6), background pressures (Fig. 4.7) and applied magnetic field configurations (Fig. 4.8). In addition, Fig. 4.9 contains a plot of the induced magnetic field obtained for the baseline case in which there is no preionized plasma, and consequently no

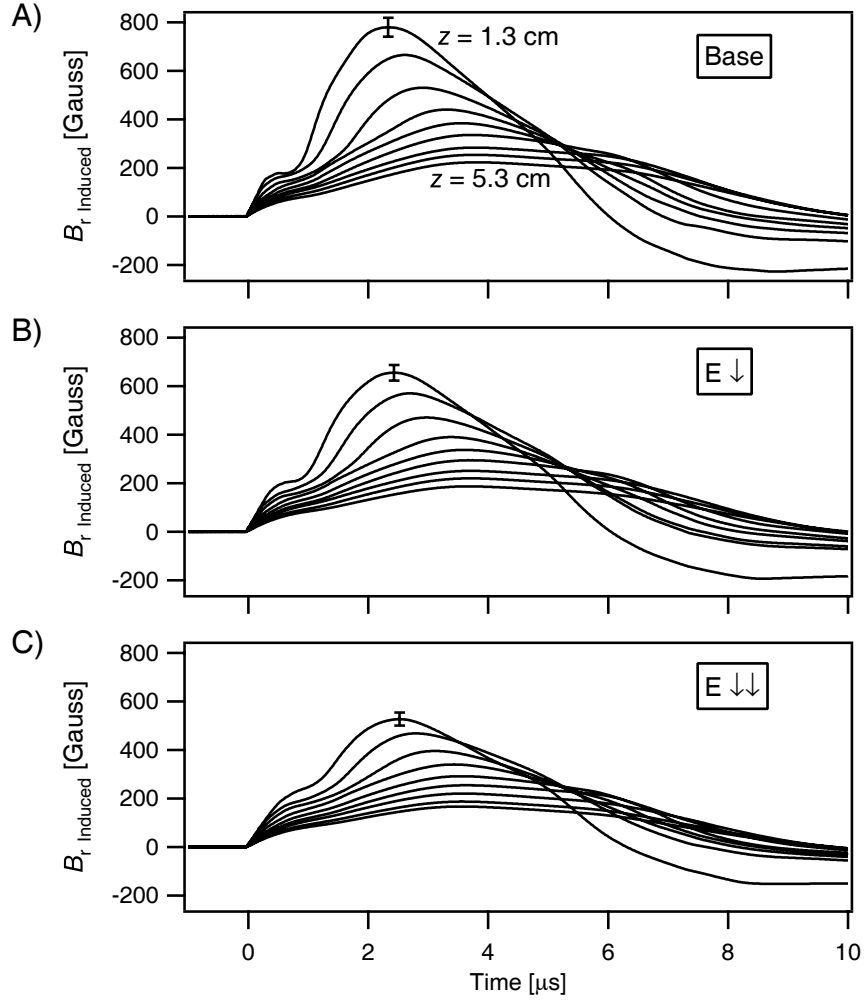


Figure 4.6: Time histories of the induced radial magnetic field strengths (with a typical error bar) for different discharge energies at a radius of 66 mm. The axial positions are spaced evenly every 5 mm.

current sheet, present. As a result, the traces in Fig. 4.9 essentially mirror the coil current. The axial, z , locations at which the measurements were made are evenly spaced every 5 mm between 1.3 cm and 5.3 cm from the coil face.

We note first that the traces all begin increasing immediately at $t = 0$. This has been previously observed in pulsed inductive devices [4, 5] and indicates that the initial fields induced by the coil rapidly diffuse through the preionized plasma, implying low initial con-

ductivity. At a time shortly after $t = 0$, the waveforms generally exhibit a distinct ‘knee’, or inflection point (which is especially evident when compared to Fig. 4.9 where preionization was not employed). This ‘knee’ is indicative of current sheet formation and the associated increases in plasma conductivity and electromagnetic shielding that accompany it. After the ‘knee’ feature the magnetic field continues to rise at all axial locations including those that have presumably not yet been reached by the current sheet. This indicates that the magnetic field continues to resistively diffuse through the plasma even after the current sheet forms.

As the pulse energy is decreased (Fig. 4.6), both the overall level of the induced magnetic field and the relative strength of the ‘knee’ feature become smaller. In addition, the ‘knee’ occurs later in time in the $E\downarrow$ and $E\downarrow\downarrow$ cases. The decreasing magnitude of the fields are expected based upon the measured accelerator coil currents, which also scale with pulse energy (see Fig. 4.1). Qualitatively, a sharper ‘knee’ is indicative of stronger current sheet formation (higher plasma current and conductivity). The initial point where the waveform begins to deviate from its initial rise is when the current sheet forms (delay time between $t = 0$ and formation, t_{delay}). As we previously stated, current sheet formation is driven by dJ_{Coil}/dt , which scales with the discharge energy. Consequently, it is not surprising that the current sheet is strongest and forms fastest for the baseline case (i.e. at higher initial energy).

As the backfill pressure is changed (Fig. 4.7), we see that while the discharge voltage and acceleration coil current remain the same in all three cases, the ‘knee’ is most distinct for the baseline case. Moreover, the current sheet forms earlier in time in the baseline case than at either higher or lower pressure. These observations are indicative of stronger current sheet formation at a background pressure of 23 mTorr. Most importantly, however, there is no observable ‘knee’ in the $z = 1.3$ cm waveform for the $P\downarrow$ case and only a very slight

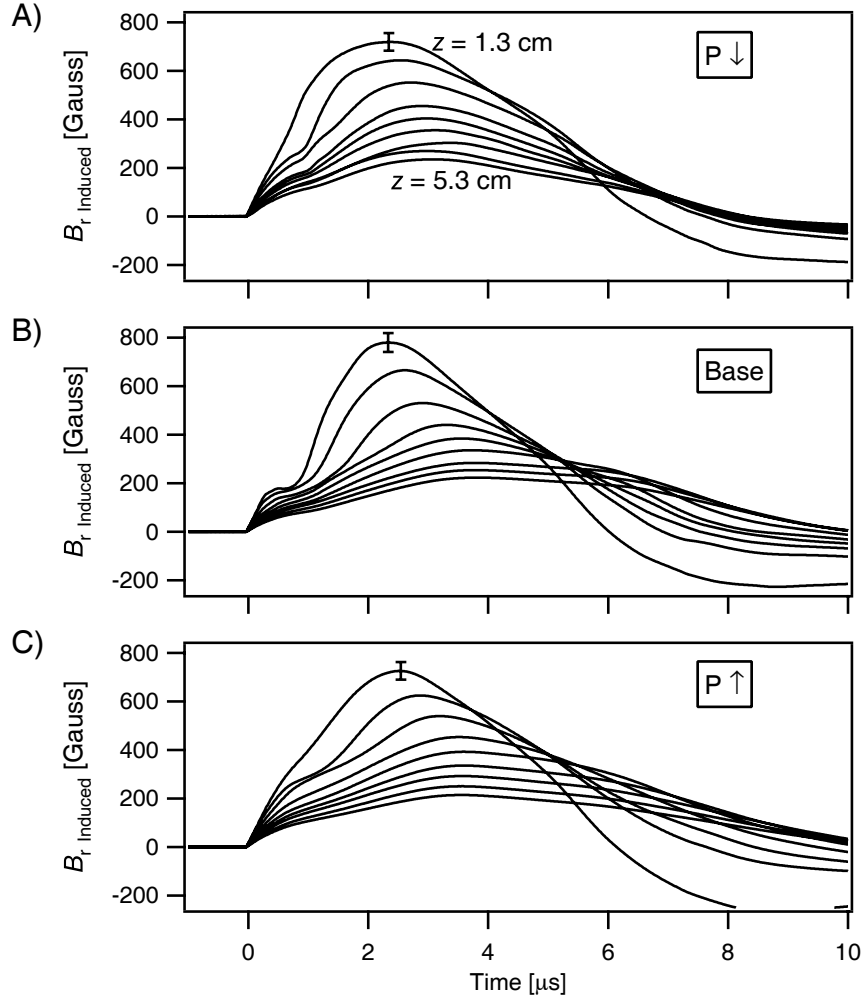


Figure 4.7: Time histories of the induced radial magnetic field strengths (with a typical error bar) for different background pressures at a radius of 66 mm. The axial positions are spaced evenly every 5 mm.

inflection at the same axial location in the $P \uparrow$ case. We can interpret these data as indicative of current sheet formation occurring somewhere between $z = 1.3$ and 1.8 cm instead of right at the face of the glass plate covering the acceleration coil.

Comparing the two data sets in Fig. 4.8, we see how the induced field waveforms are affected by changing the applied magnetic field configuration. As in the higher and lower pressure cases, there is no observable ‘knee’ for the $B \downarrow$ configuration in the $z = 1.3$ cm

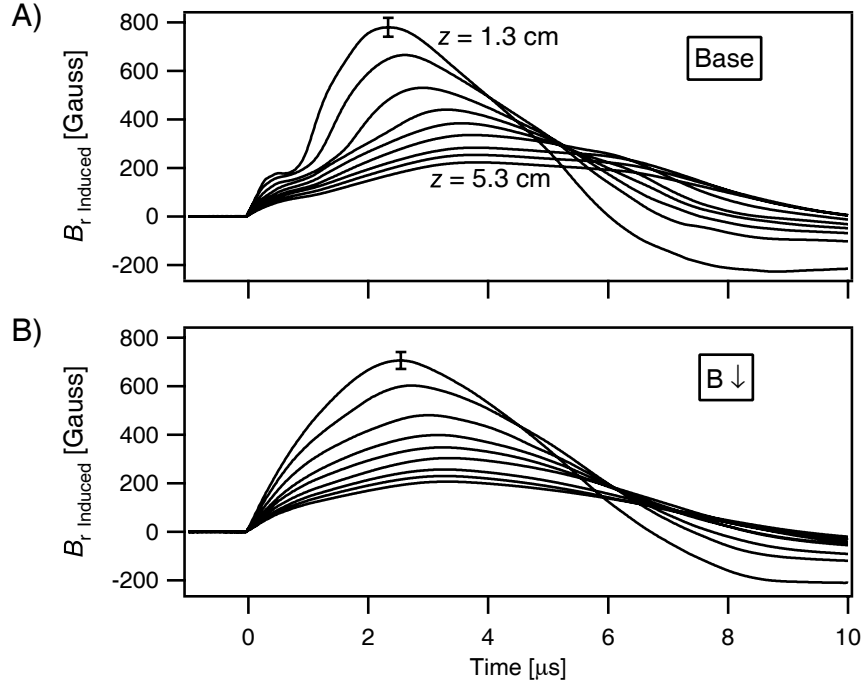


Figure 4.8: Time histories of the induced radial magnetic field strengths (with a typical error bar) for different applied magnetic field configurations at a radius of 66 mm. The axial positions are spaced evenly every 5 mm.

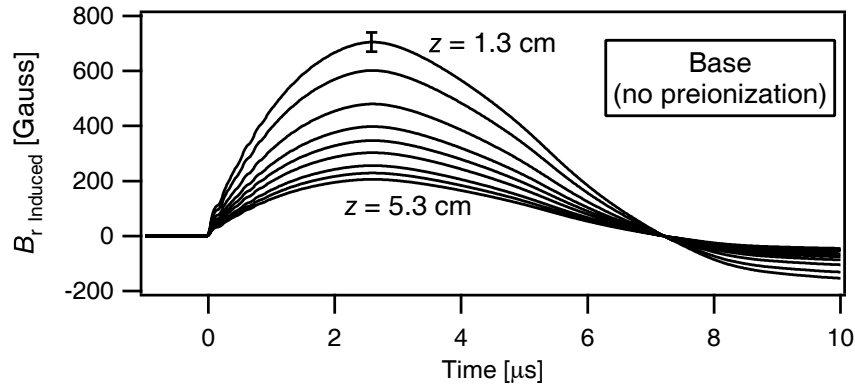


Figure 4.9: Time histories of the induced radial magnetic field strengths (with a typical error bar) for the baseline condition with no RF preionization obtained at a radius of 66 mm. The axial positions are spaced evenly every 5 mm.

waveform, indicating that the sheet forms downstream of this axial location. Moreover, there is only a slight inflection in the waveforms acquired at downstream axial locations, implying weak current sheet formation compared to the baseline case.

4.4 Current Density Contours

Magnetic field maps, like those presented in Figs. 4.6, 4.7 and 4.8, provide a good qualitative indication of the presence and effect of a current sheet. However, as the induced magnetic field is a linear superposition of the fields radiated by two separate current sources, the acceleration coil and the current sheet, there is a great deal of ambiguity involved in the interpretation of field data acquired along a single, axial line. This difficulty is bypassed by measuring the magnetic field in a two-dimensional r - z plane and using Ampère's law,

$$\nabla \times \mathbf{B} = \mu_0 \mathbf{j}$$

to compute the current density, j_θ , in the sheet. This works because the only portion of the magnetic field in the region of interest that is not curl-free is attributable to the current sheet.

Azimuthal current density profiles for the various cases tested in the FARAD POCX are presented in Figs. 4.10, 4.11 and 4.12. To numerically compute the curl of B , data on a two-dimensional, r - z grid are required. The axial spacing, Δz , between the magnetic field data points is 5 mm and the radial spacing, Δr , is 4 mm (measurements obtained at $r = 66 \pm 2$ mm). The error bars are a combination of the errors on the magnetic field measurements and the uncertainty on the B -dot probe positions.

The initial peak in the current density profile at each axial station represents the current sheet. We observe a weakening of the sheet as it reaches axial stations located further away from the acceleration coil. The current sheet velocity can be estimated based upon the time

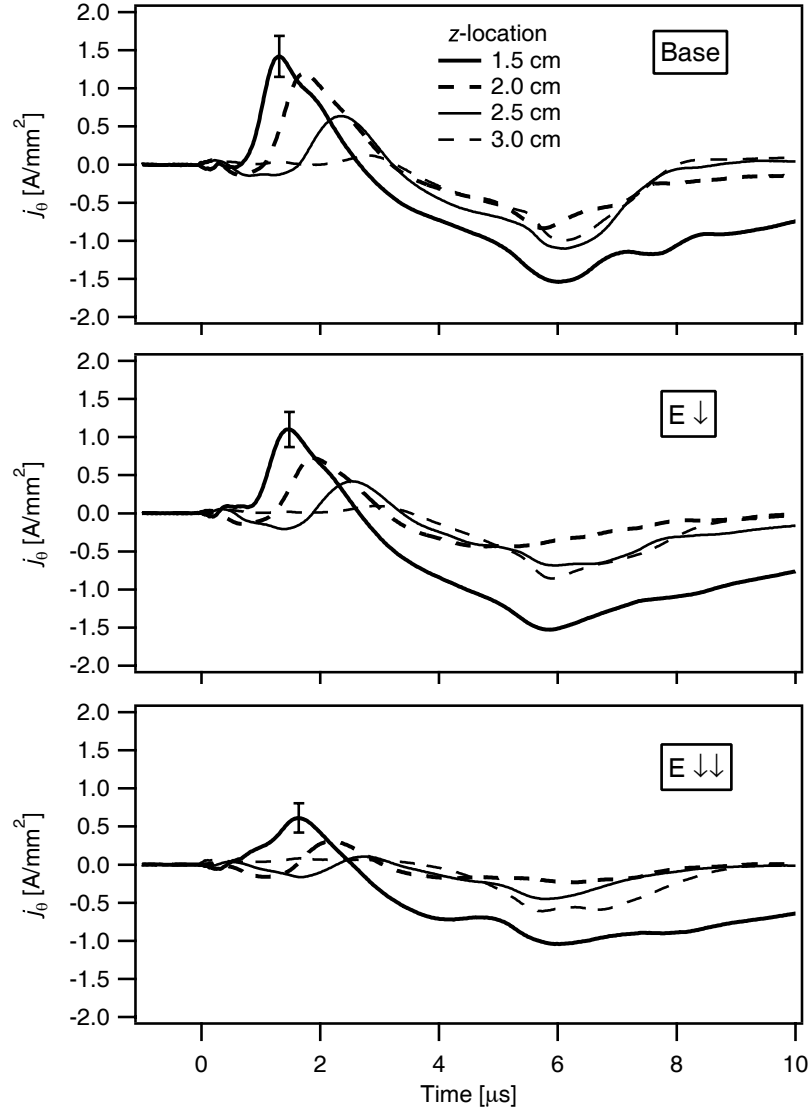


Figure 4.10: Time histories of the induced plasma current densities (with typical error bars) for different discharge energies at various axial stations at a radius of 66 mm.

the peak current passes the different axial stations. For example, the inferred sheet velocity in the baseline case between $z = 1.5$ cm and $z = 2.0$ cm is 12 km/s, while the velocity between $z = 2.0$ cm and $z = 2.5$ cm is 8 km/s. The maximum inferred sheet velocities for the other cases are given in Table 4.2. We do not observe a second current sheet (or ‘crowbar’ discharge) forming after dJ_{Coil}/dt changes sign, leading us to conclude that the

threshold dJ_{Coil}/dt level necessary to form a current sheet is not reached during the second half-cycle in the POCX.

In Fig. 4.10 the leading edge of the current sheet passing a given axial location becomes less sharp and pronounced as the discharge energy is reduced. Also, at a given axial location the magnitude of the passing peak is decreased. These observations can be explained by recalling that current in the sheet is driven by Faraday induction, which scales with dJ_{Coil}/dt and is lower for decreasing initial capacitor voltage (energy for constant capacitance). Thus, at lower initial energy we obtain a current sheet that forms slower and possesses a lower current density level. We also find in Table 4.2 that the speed of the current sheet is lower as the discharge energy is reduced. This is because both the peak plasma current density, which scales with dJ_{Coil}/dt , and the peak induced magnetic field, which scales with J_{Coil} , decrease with decreasing initial discharge energy. Consequently, at lower capacitor energies both the induced current density and the induced magnetic field are smaller, resulting in a significantly decreased $\mathbf{j} \times \mathbf{B}$ body force and lower current sheet speeds.

The current sheet broadens as the background pressure is increased (Fig. 4.11). A pronounced sheet is observed passing $z = 1.5$ cm in all three cases. However, in both the $P\downarrow$ and $P\uparrow$ cases, the sheet passing the $z = 2.0$ and 2.5 cm locations has dissipated faster than the sheet in the baseline case. In addition, the data in Table 4.2 suggest that the average sheet speed is greatest in the moderate pressure baseline case. These data, in conjunction with the B -dot probe data, provide evidence that there exists a background pressure in the proof-of-concept experiment between 7.5 and 48 mTorr at which current sheet strength and speed are optimized.

The data in Fig. 4.12 show a poorly formed current sheet in the $B\downarrow$ case. Comparing to the baseline case, the current in the sheet in the $B\downarrow$ case is lower in magnitude, moves

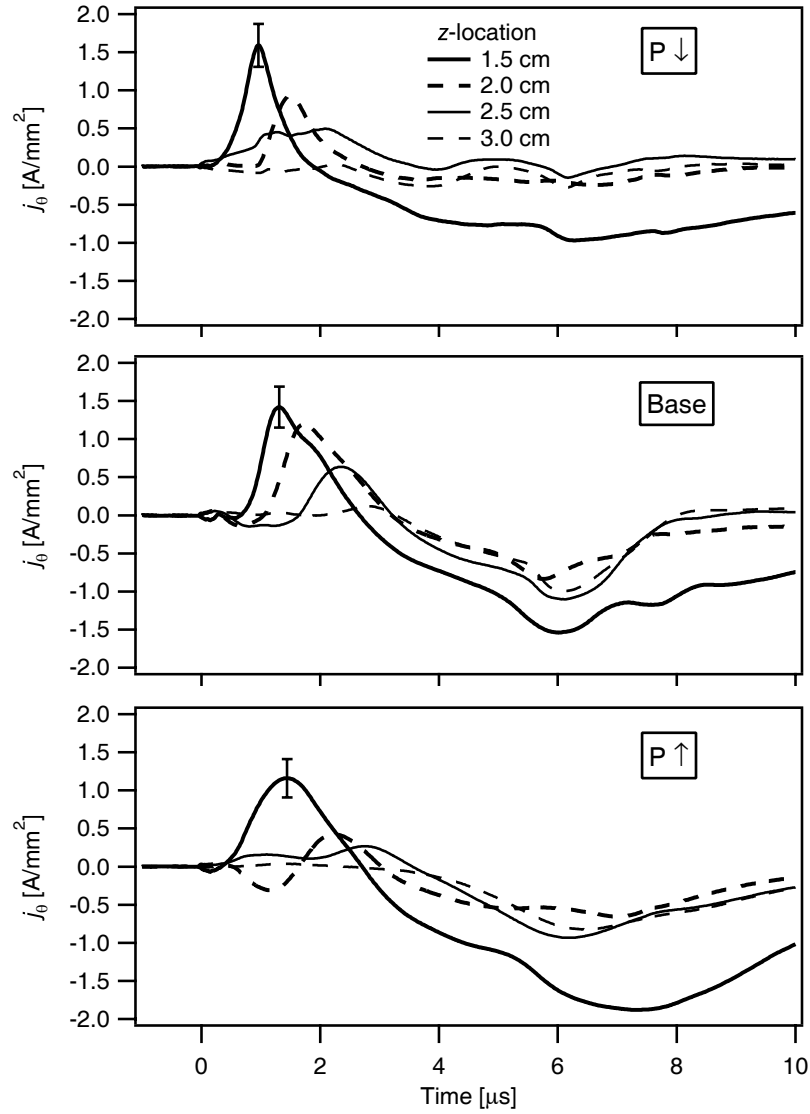


Figure 4.11: Time histories of the induced plasma current densities (with typical error bars) for different backfill pressures at various axial stations at a radius of 66 mm.

slower and is less concentrated. In addition, it has nearly disappeared by the time it reaches the $z = 2.0$ cm location. This serves to confirm our B -dot probe observation that the current sheet is weaker in this case than the baseline case.

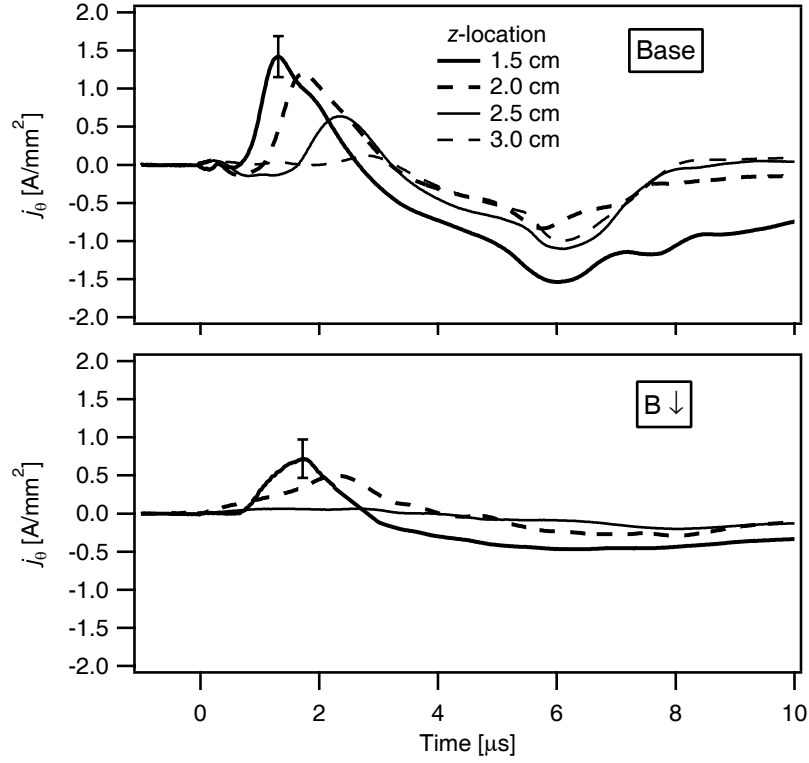


Figure 4.12: Time histories of the induced plasma current densities (with typical error bars) for different applied magnetic field configurations at various axial stations at a radius of 66 mm.

Table 4.2: Maximum sheet velocities inferred from the j_θ measurements presented in Figs. 4.10, 4.11 and 4.12.

Case	Base	E↓	P↓	E↓↓	B↓	P↑
Inferred Sheet Speed [km/s]	12.2	11.0	9.3	8.6	8.6	6.0

4.5 Current Sheet Visualization

Representative, contrast-enhanced photographs of the current sheet at several instances in time are presented in Fig. 4.13. The unfiltered images were obtained for the baseline case

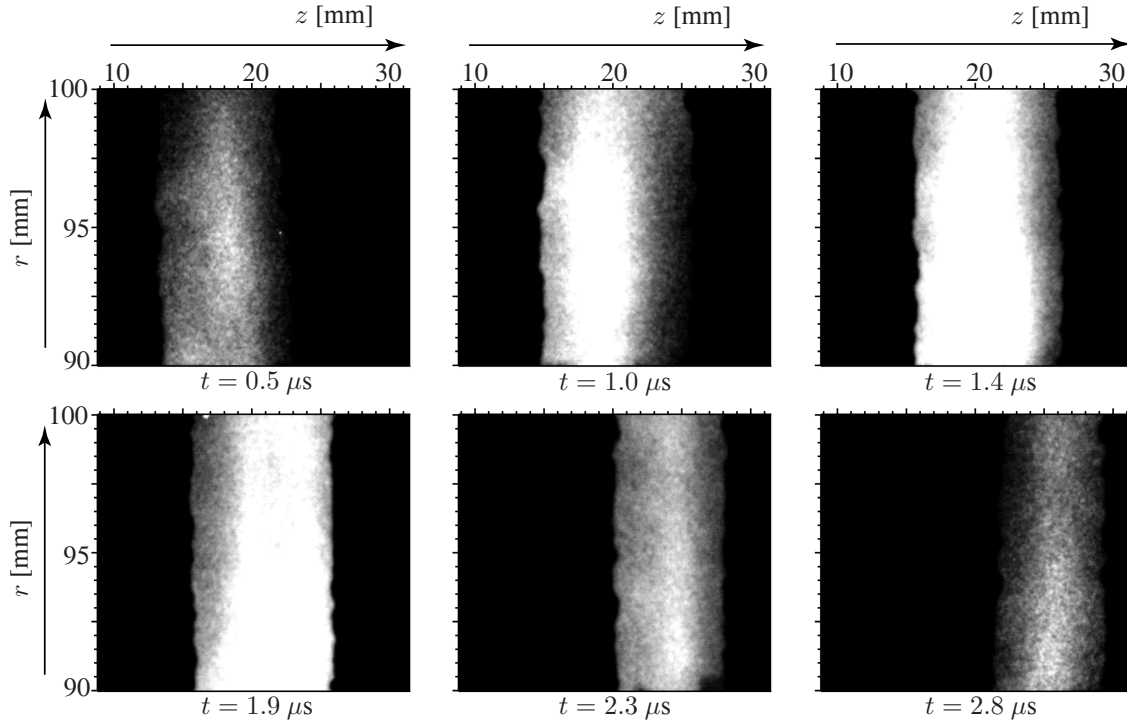


Figure 4.13: Representative high-speed photographs acquired using a fast-framing camera at a framing rate of 20 million frames per second. These photos show the sheet initiation ($t = 0.5 \mu\text{s}$), acceleration ($t = 1.0 \mu\text{s}$ to $t = 2.3 \mu\text{s}$) and termination ($t = 2.8 \mu\text{s}$). (The contrast in these photographs has been enhanced through digital image processing.) The pictures represent the baseline case. The drive coil is located at $z = 0 \text{ mm}$.

and show that the current sheet goes through three separate phases during the discharge; initiation, acceleration, and termination. Each of these phases is labeled in the caption of Fig. 4.13.

The current sheet locations are determined as follows. Digitized frames are loaded into a program capable of performing image processing operations (Igor Pro, Wavemetrics Inc.). The intensity values of the individual pixels are summed in the vertical, r , direction yielding a waveform comprised of summed intensity as a function of z . A Gaussian distribution is then fit to the intensity waveform,

$$\text{Intensity} = A \exp \left[- \left(\frac{z - z_0}{\sqrt{2}\sigma} \right)^2 \right],$$

where A is a constant, z_0 is taken to be the current sheet center and σ is taken as a measure of the current sheet's axial width about the position z_0 . Note that the raw images were not contrast enhanced before analysis.

Resulting current sheet position histories for different experimental operating conditions are presented in Figs. 4.14, 4.15 and 4.16. Each data point represents data extracted from a curve fit to the intensity data from one photographic frame. The various position histories clearly show the discharge progressing through the initiation, acceleration and termination phases. For example, in the baseline case the current sheet initiates at $z = 18.4$ mm and remains stationary, with its light emission increasing and intensifying until $t \approx 1.1$ μ s. It then quickly accelerates, reaching a constant velocity which it maintains between 1.1 and 2.4 μ s. A linear curve fit of this portion of the data yields a sheet speed of approximately 4.6 km/s. The sheet speeds corresponding to the other cases are given in Table 4.3. Finally, between 2.4 and 3 μ s, the current sheet's motion ceases and its light emission decreases. The termination phase occurs as dJ_{Coil}/dt in the external circuit approaches zero, mirroring the result of the current density measurement.

We observe in Fig. 4.14 that the initial position of the sheet is the same (within the error bars) for all three discharge energies. While the location is the same, the duration of the initiation phase (constant initial position) is longer in the lower energy cases. As expected, we see in Table 4.3 that the sheet experiences less acceleration when the discharge energy is lowered. However, the position histories also show that in the baseline case the sheet slows sooner than in the lower energy cases. While the baseline current sheet still travels a greater overall distance, the sheets in the $E\downarrow$ and $E\downarrow\downarrow$ cases narrow the gap at the end of the discharge cycle.

In Fig. 4.15, we see that the initial current sheet position is approximately the same in both the baseline and $P\uparrow$ cases while sheet formation in the $P\downarrow$ case occurs further down-

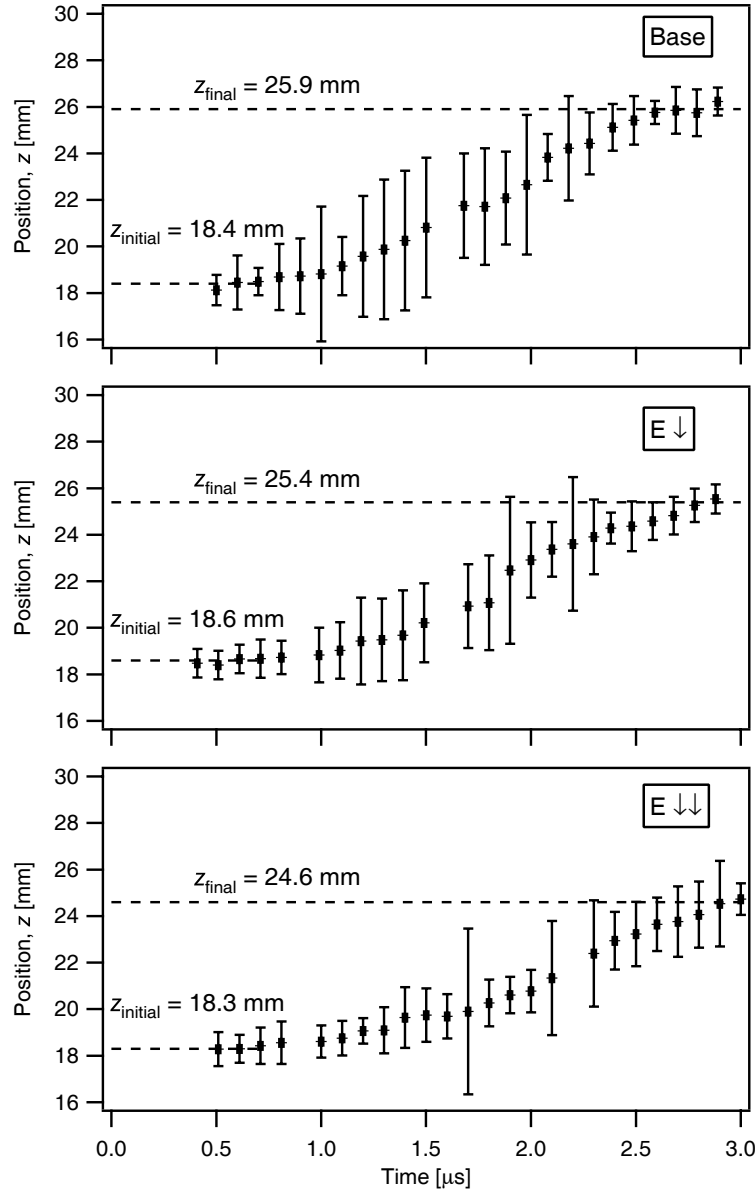


Figure 4.14: Photographically measured current sheet position histories for different discharge energies.

stream (further from the acceleration coil). Current sheet speed (Table 4.3) is generally greater at lower pressures, which is expected since resistance to current sheet motion scales with the density of the gas that must be entrained by the sheet. However, while the initial

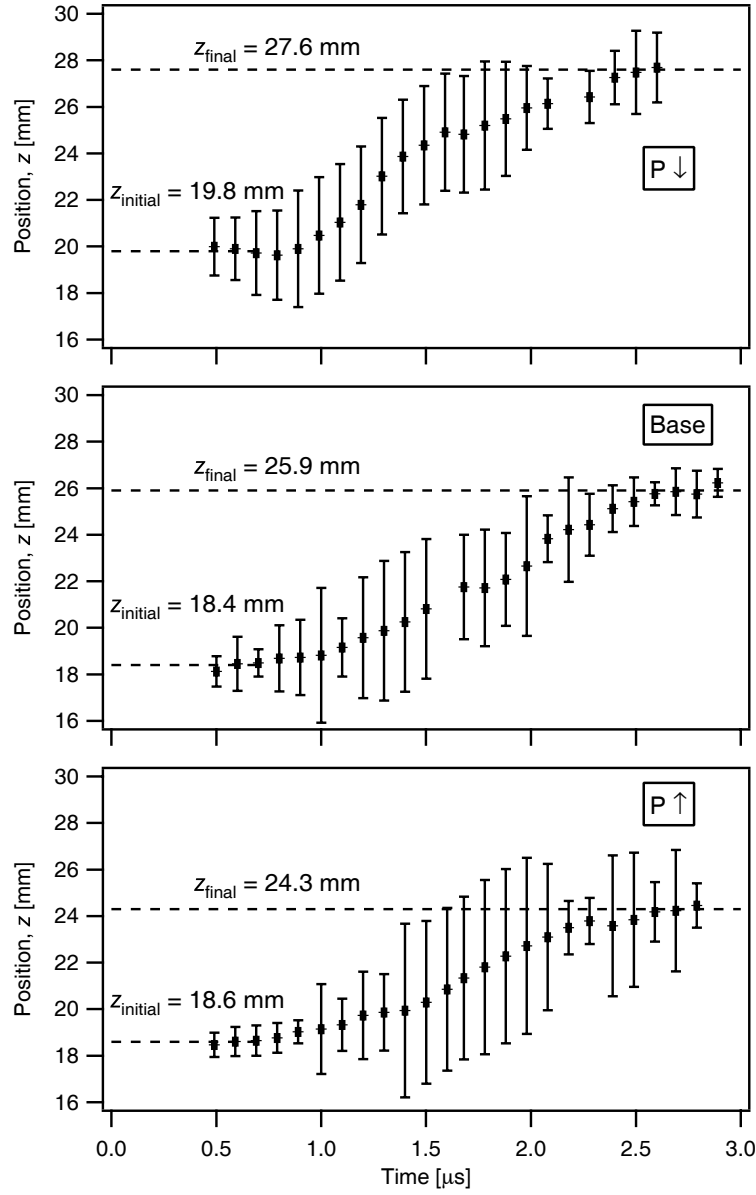


Figure 4.15: Photographically measured current sheet position histories for different back-fill pressures.

sheet speed in the $P\downarrow$ case is significantly greater than in the other cases, beyond $t = 1.6 \mu\text{s}$ we observe an abrupt deceleration to a speed slower than in either the baseline or $P\uparrow$ cases. The sheet travels furthest downstream in the $P\downarrow$ case, and while this is partly due to

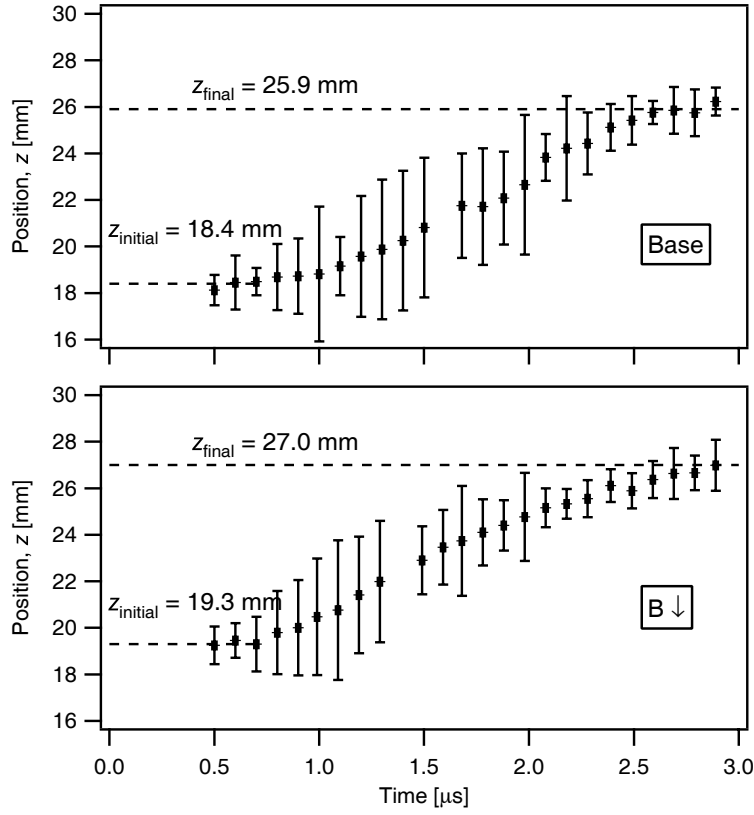


Figure 4.16: Photographically measured current sheet position histories for different applied magnetic field configurations.

it having a greater velocity before $t = 1.6 \mu\text{s}$, it is also due to the fact that it started further downstream than in the other two cases.

In terms of applied field variation, the current sheet in the B_{\downarrow} case is observed in Fig. 4.16 forming further downstream than in the baseline case. We also see a slower sheet in the B_{\downarrow} case (Table 4.3). Somewhat surprising is the fact that the sheet begins moving sooner in the B_{\downarrow} case (compare the relative position changes in the third and fourth points of each graph) and it remains in motion beyond $2.6 \mu\text{s}$, which is when the baseline case current sheet motion ceases. This may be due to the longer time it takes (at constant discharge energy) to generate an induced field capable of driving the current sheet across the stronger

Table 4.3: Sheet velocities found from linear curve fits of the data presented in Figs. 4.14, 4.15 and 4.16. Fit was performed between $t = 1.1 \mu\text{s}$ and $t = 2.4 \mu\text{s}$ except in the case of $\text{P}\downarrow$ where the fits were performed for: ^(a) $1.1 \leq t \leq 1.6 \mu\text{s}$ and ^(b) $1.6 \leq t \leq 2.4 \mu\text{s}$.

Case	Base	$\text{E}\downarrow$	$\text{E}\downarrow\downarrow$	$\text{P}\downarrow$	$\text{P}\uparrow$	$\text{B}\downarrow$
Inferred Sheet Speed [km/s]	4.6	4.3	3.0	$7.9^{(a)}, 2.9^{(b)}$	3.8	4.0

applied field found in the baseline case. In addition, the induced field most likely drops below the threshold for sheet motion later in the $\text{B}\downarrow$ case implying that the current sheet remains in motion longer relative to the baseline.

We note finally that there are discrepancies between the current sheet velocities inferred from the current density measurements (Table 4.2) and those found in Table 4.3 of this section. These discrepancies are discussed in Sect. 4.8.

4.6 Plasma Density

Plasma density measurements (time histories of ion saturation currents) were acquired using the circuit described in Sect. 3.5. A 9V battery was used to apply a bias voltage to the probe. This produced repeatable results for discharge energies at or below 44 J. However, difficulties were encountered when measurements were attempted for the baseline and $\text{E}\downarrow$ cases (possibly due to either low frequency response of the battery or its inability to supply the required current). Consequently, the only data which completely match the experimental conditions of the previous data sets correspond to the $\text{E}\downarrow\downarrow$ case (Fig. 4.17). For the three other data sets found in this section, we employ the slightly modified shorthand given in Table 4.4.

Measurements were performed at a radius of 66 mm and the axial, z , locations were evenly spaced every 5 mm between 1.3 cm and 4.3 cm from the coil face. The raw data

Table 4.4: Summary of the experimental conditions tested in the FARAD POCX using a Langmuir probe.

Designation	V_0 (E_0) [V (J)]	p_0 [mTorr]	B_r [Gauss]
E↓↓	1500 (44)	23	160
E↓↓ P↓	1500 (44)	7.5	160
E↓↓ P↑	1500 (44)	48	160
E↓↓ B↓	1500 (44)	23	80

have been smoothed to remove the 13.56 MHz RF signal. In addition to the plasma density, the floating potential was also measured for each case to determine if our biased probe was actually near the ion saturation regime.

In Fig. 4.17, a plasma sheet can be seen forming close to the acceleration coil and then propagating in the z -direction for the first 4 to 5 μs of the discharge. The number density grows rapidly at the beginning of the discharge and begins dropping after $t \approx 3 \mu\text{s}$. This decrease in number density is expected in all trials since the current density in the sheet, which allows for inductive energy coupling between the acceleration coil and the plasma, goes to zero at this time. The initial inductive current sheet does not totally dissipate though, and at $t \approx 6 \mu\text{s}$ (time of greatest dI/dt in the second half-cycle of the external circuit) a second lower density plasma discharge forms filling nearly the entire axial region. It is likely that this secondary discharge is the result of the reversal current in the acceleration coil coupling to a slow-moving plasma wake left behind by the initial current sheet.

As the pressure is lowered (Fig. 4.18) the plasma density waveforms rise and fall more sharply than in the E↓↓ case. In addition, the peak number density occurs sooner in time at a given axial location in the E↓↓ P↓ case. This is especially true at the $z = 1.3$ and 1.8 cm locations. These data, combined with the current sheet visualization for the P↓ case, may

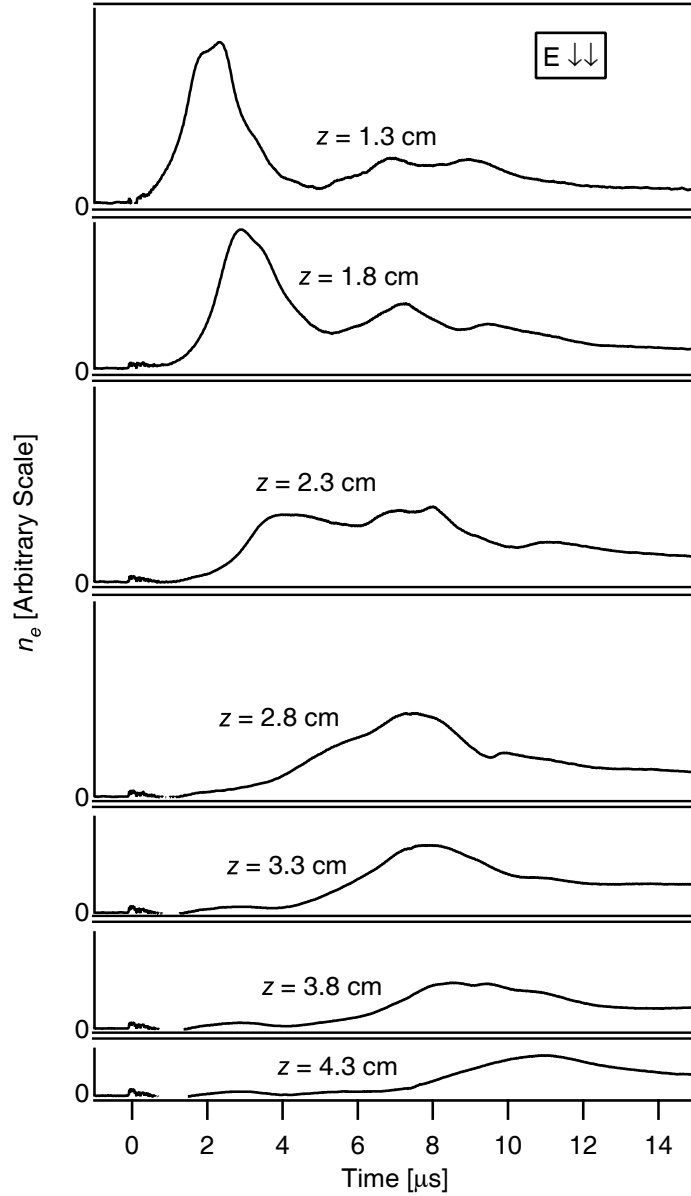


Figure 4.17: Plasma density measurements for the $E\downarrow\downarrow$ case at various axial locations at a radius of 66 mm. For reference, the peak value in this case is expected to be less than the value of $n_e = 7 \times 10^{14} \text{ cm}^{-3}$ that was obtained in the baseline case using laser interferometry.

imply that the current sheet is moving much more quickly at the lower pressure. However, we also have evidence supporting the more likely conclusion that in the $P\downarrow$ case the current

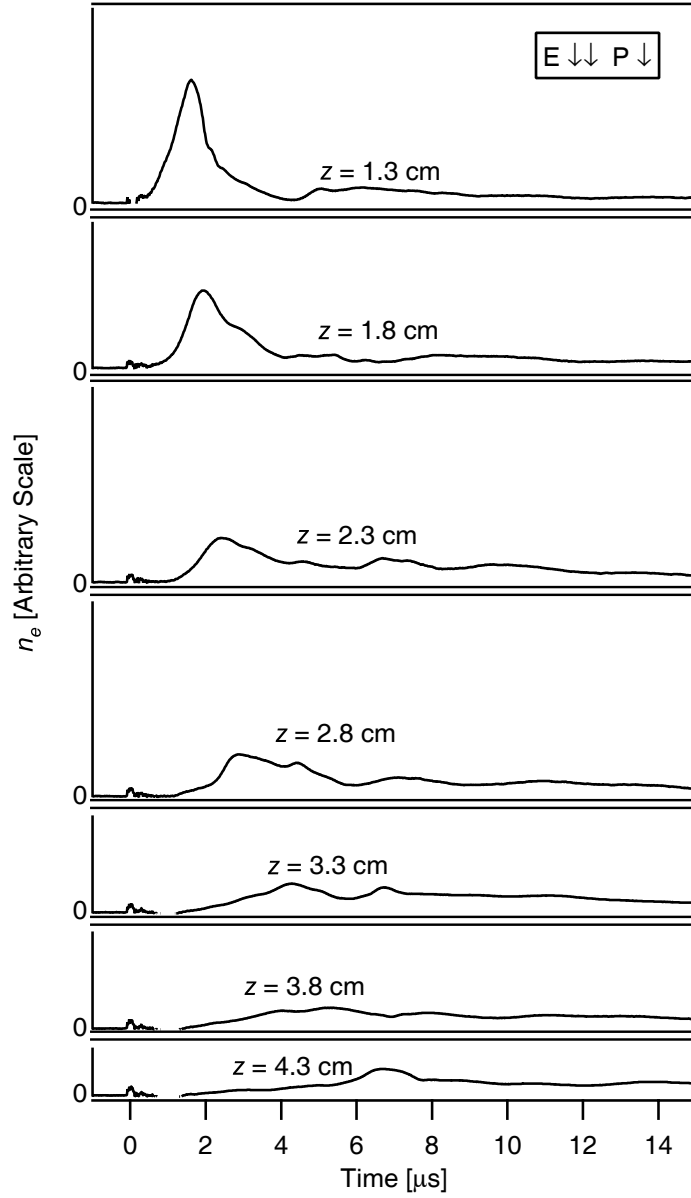


Figure 4.18: Plasma density measurements for the $E \downarrow \downarrow P \downarrow$ case at various axial locations at a radius of 66 mm.

sheet forms further from the acceleration coil than in the baseline case. It is not difficult to see why that should also be the case for the $E \downarrow \downarrow P \downarrow$ case. The nearly coincident (in time) peaks at $z = 1.3$ and 1.8 cm may be due to the sheet forming between those two locations.

Since the probe tip is a 3 mm in length, the data in both waveforms could represent current collection from the newly forming, but still mostly stationary, sheet. The initial plasma is greatly diminished beyond $t \approx 3 \mu\text{s}$, but it does continue to propagate downstream. Unlike in Fig. 4.17, an appreciable secondary discharge does not occur beyond $t \approx 6 \mu\text{s}$. This could imply that the current sheet more effectively sweeps the plasma in the lower density case, leaving very little plasma behind to couple with the ringing coil current and form a secondary discharge.

The waveforms in Fig. 4.19 indicate that it takes longer in the $E \downarrow P \uparrow$ case for the peak plasma density to reach a given location and that the plasma then maintains an elevated density at that location much longer than the previous two cases. These observations imply that the sheet is moving more slowly in this case. The result is not surprising since resistance to current sheet motion should increase with increased background density due to neutral drag. Moreover, the elevated density after the peak passes may be evidence that the sheet is leaving a substantial amount of ionized propellant behind as it passes an axial location. Like in the other cases, the number density decreases beyond $t \approx 3 \mu\text{s}$ at all locations. The density increases again during the second half-cycle of the external discharge ($t > 6 \mu\text{s}$), forming a highly ionized plasma located in a broad region between $z = 1.3$ and 2.8 cm. The secondary discharge is long lived and eventually fills the entire test region. The small gap in the waveform for $z = 1.3$ cm is a time where the bias voltage was not low enough to consider even the qualitative ion current measurement accurate. (The arbitrary condition $V_{\text{bias}} - V_{\text{float}} > -5$ volts was employed to determine if the bias voltage was low enough to allow use of the ion current measurement. This is somewhat justified since the difference between the floating potential and the potential at which ion saturation of a Langmuir probe occurs is typically small (5-10 volts).)

In Fig. 4.20, a much larger portion of the data between 4 and 8 μs has been discarded

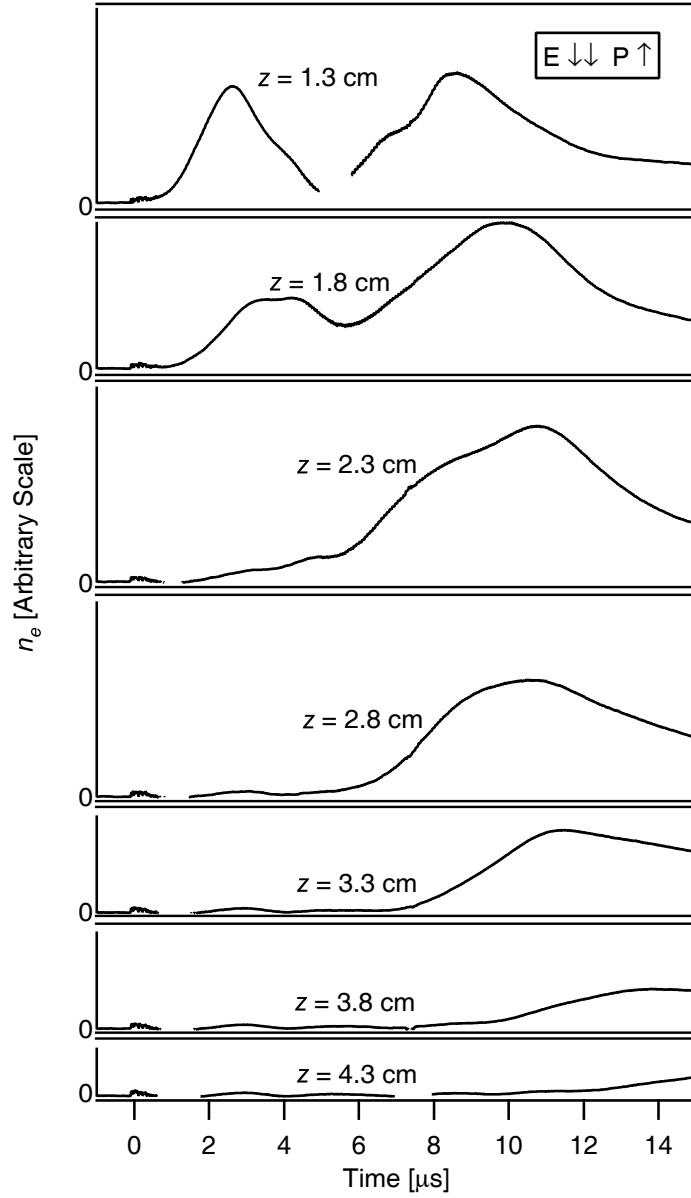


Figure 4.19: Plasma density measurements for the $E \downarrow \downarrow P \uparrow$ case at axial locations spaced 5 mm apart at a radius of 66 mm.

in the region where the voltage threshold condition was not met. Comparing Figs. 4.20 and 4.17, we see that the density rise at the first few axial locations occurs sooner in the $E \downarrow \downarrow B \downarrow$ case. Like in the $E \downarrow \downarrow P \downarrow$ case, this could be indicative of current sheet formation

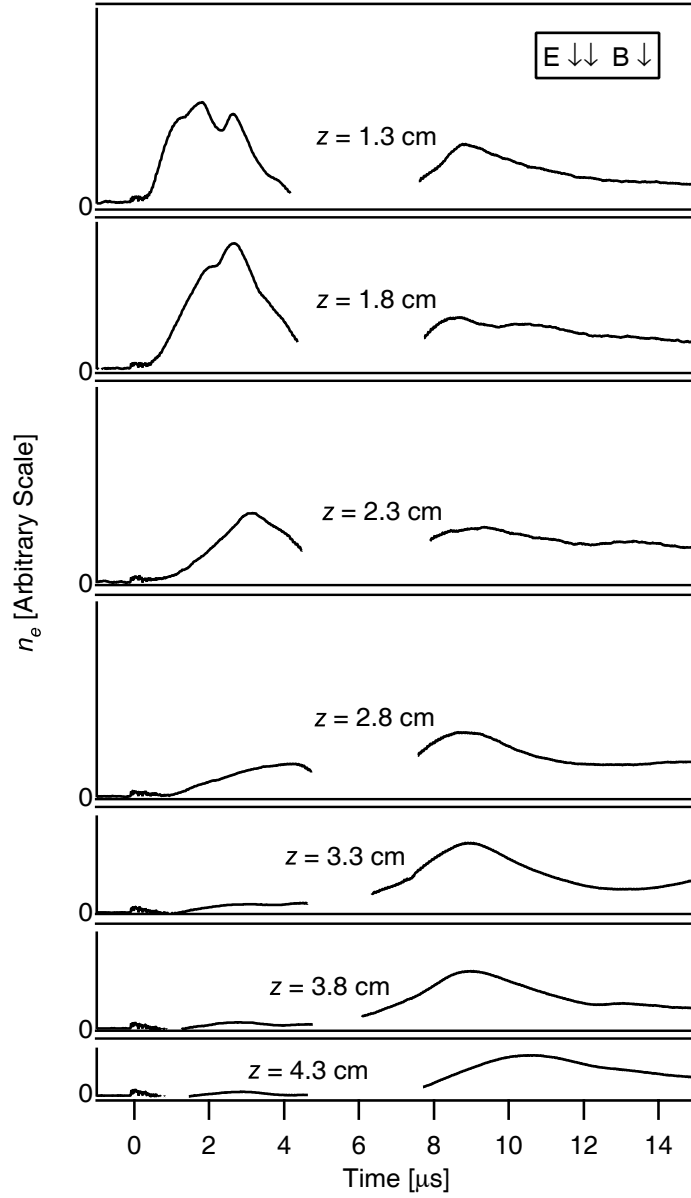


Figure 4.20: Plasma density measurements for the $E \downarrow \downarrow B \downarrow$ case at axial locations spaced 5 mm apart at a radius of 66 mm.

occurring further downstream from the acceleration coil or it could be that the weaker applied field provides less resistance to current sheet motion. The initial plasma density rise at the $z = 1.3$ cm position in Fig. 4.20 appears truncated relative to the other data sets

presented in this section. The cause of this truncation is not well understood. Except for the the gap in the data set, the $E \downarrow \downarrow B \downarrow$ waveforms are qualitatively similar to those previously presented for the $E \downarrow \downarrow$ case.

4.7 Calculated Plasma Parameters

Before proceeding with any further discussion of the experimental data, it is important to estimate the length and time scales of various plasma processes in the proof-of-concept experiment. These estimates are computed using the values presented in Table 4.5. The values are meant to be representative of the plasma conditions before and during the FARAD discharge pulse. As was described in Sect. 3.5, the peak number density in the sheet ($7.4 \times 10^{14} \text{ cm}^{-3}$) was found using the laser interferometry system described in Refs. [19, 23] while the number density in the preionized plasma (10^{11} cm^{-3}) was measured using an RF-compensated Langmuir probe[15, 33]. The largest unknown in our calculations is the ion temperature, T_i , in the current sheet, which is probably much greater than 300 K but somewhat less than the electron temperature. The time-averaged ion temperature given by detailed numerical simulations of an argon current sheet in the PIT MkV is in the neighborhood of 1.4 eV[34], which will suffice for the order of magnitude calculations pre-

Table 4.5: Estimated plasma parameters for the helicon generated preionized plasma and the FARAD current sheet. ($\alpha \equiv$ ionization fraction.)

	Preionized Plasma	Sheet Plasma
$n_e [\text{cm}^{-3}]$	10^{11}	7.4×10^{14}
$T_e [\text{eV}]$	2.5	2.5
T_i	300 K	1.4 eV
$B [\text{gauss}]$	160	700
α	$\sim 10^{-4}$	$\sim 10^{-1}$

sented here. The ambient argon gas pressure and temperature for these calculations were 23 mTorr and 300 K. The parameters were all computed using their standard definitions[35]-[37]. The cross-section for an ion-neutral collision is taken as $1.4 \times 10^{-18} \text{ m}^2$ while the value for an electron-neutral collision is $4 \times 10^{-20} \text{ m}^2$ [38].

The time scales of various processes in the FARAD are presented for both the preionized helicon plasma (Fig. 4.21A) and the inductive current sheet (Fig. 4.21B). We see that both immediately before and during the FARAD pulse, all of the various plasma phenomena (except for ion cyclotron motion) are occurring on much shorter timescales than the FARAD pulse.

Relevant length scales in the FARAD plasma are presented for the preionized plasma (Fig. 4.22A) and the current sheet (Fig. 4.22B). The ‘probe radius’ in these plots refers to the Langmuir probe used to measure the relative plasma densities. In the helicon plasma, all the collisional length scales are much greater than the probe (and its associated sheath and presheath which are $\mathcal{O}(10 - 100)$ Debye lengths, λ_D , in thickness). Consequently, the sheath formed by the preionized plasma around the probe tip can be considered collisionless. In addition, the probe tip is much smaller than both the ion and electron cyclotron radii implying that the helicon-generated plasma can be considered as unmagnetized in the probe sheath. Recall that both conditions are necessary if any reliable quantitative data regarding the plasma density is to be extracted from the Langmuir probe (see section 3.5 for the list of assumptions necessary for proper to extract useful quantitative data from a Langmuir probe). This assumption is violated in the current sheet, where the electron cyclotron radius is smaller than the probe dimension, implying that the current sheet plasma must be considered as magnetized on the length scale of the probe.

Several important dimensionless plasma parameters and characteristic plasma velocities are presented for completeness in Table 4.6. Some of these parameters will be useful

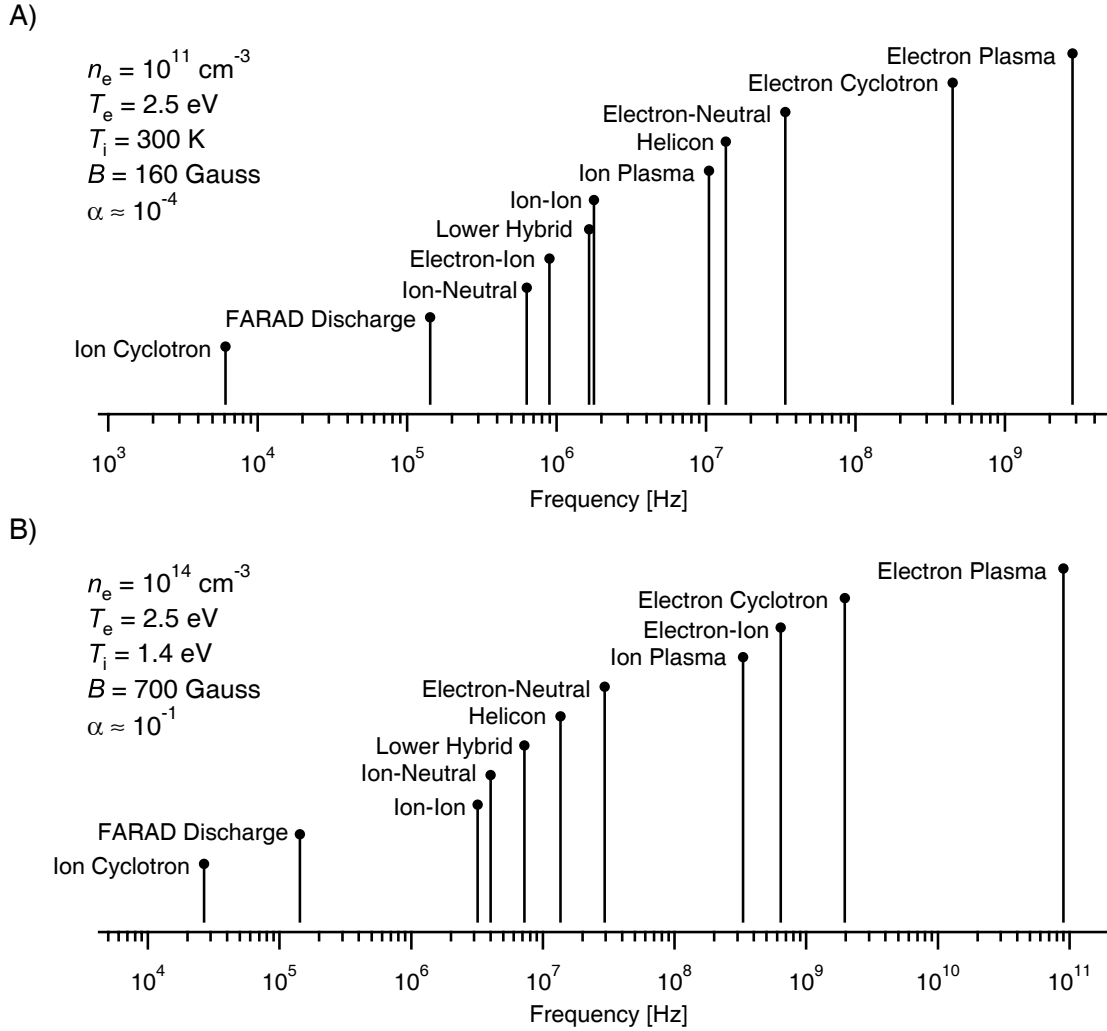


Figure 4.21: Characteristic frequencies for different plasma processes in: A) the preionized plasma and B) the inductive current sheet. Calculations are performed using the assumptions given in the text.

for the ensuing discussion section. The Alfvén velocity is defined as $v_A = B/\sqrt{\mu_0 m_i n_i}$ and the critical ionization velocity is $v_{CIV} = \sqrt{2\varepsilon_i/m_i}$, where ε_i is the ionization potential of a neutral background atom.

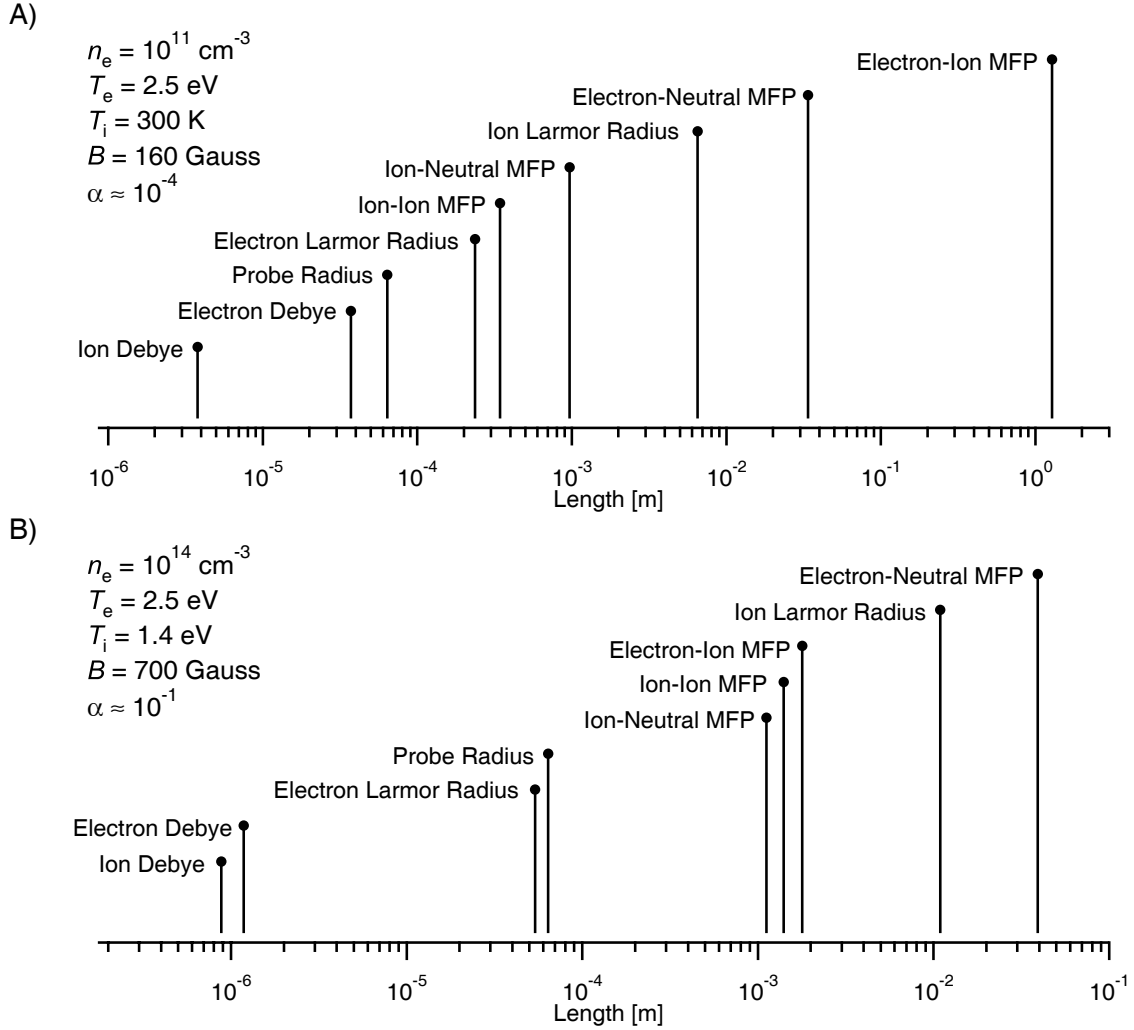


Figure 4.22: Computed length scales for different plasma processes in: A) the preionized plasma and B) the inductive current sheet. Calculations are performed using the assumptions given in the text. The ‘probe radius’ refers to the Langmuir probe.

Table 4.6: Estimated dimensionless parameters and characteristic plasma velocities in both the helicon generated preionized plasma and the FARAD current sheet.

	Preionized Plasma	Sheet Plasma
Electron Hall Parameter (Ω_e)	12	3
Ion Hall Parameter (Ω_i)	1×10^{-3}	4×10^{-5}
Plasma Energy/Mag. Field Energy (β_e)	$\mathcal{O}(10^{-4})$	$\mathcal{O}(10^{-2})$
Electron Thermal Velocity ($v_{th,e}$) [m/s]	6.6×10^5	6.6×10^5
Ion Thermal Velocity ($v_{th,i}$) [m/s]	2.5×10^2	1.8×10^3
Ion Acoustic Velocity [m/s]	3.1×10^3	3.1×10^3
Alfvén Velocity (v_A) [m/s]	1.7×10^5	2.4×10^4
Critical Ionization Velocity (v_{CIV}) [m/s]	8.7×10^3	8.7×10^3

4.8 Discussion

One may wonder if the current sheet is actually accelerating any mass. Since no thrust stand measurements were performed, this is a valid concern. If the entire fill density was accelerated by the $\mathbf{j} \times \mathbf{B}$ body force ($j_\theta = \mathcal{O}(1 \text{ A/mm}^2)$, $B_r = 0.06 \text{ T}$ at $r = 66 \text{ mm}$, $\rho_0 = 5 \times 10^{-5} \text{ kg/m}^3$, $t = \mathcal{O}(1 \text{ } \mu\text{s})$ in the baseline case) it would only reach a speed on the order of 1 km/s. However, this assumes that the sheet perfectly entrains all the mass available to it. Research in pulsed plasma thrusters has shown that the current sheet is, in fact, permeable and a certain amount of gas can slip behind the sheet[19] and we even observe this in the data sets presented in Figs. 4.17, 4.19 and 4.20. We can see in Fig. 4.22B that the electron-ion momentum exchange coulomb mean free path is 1-2 mm. This implies momentum coupling between the electron and ion fluids on the length scale of the observed motion. The luminous front can only be emission from excited argon and argon-ion states. However, the electron-neutral collision mean free path in the sheet (which corresponds to collisional excitation) is greater than the length scale of the observed motion. We must therefore conclude that the motion of the luminous front is not merely the result of an

ionization front going through the gas, but a manifestation of a current sheet entraining at least some ions that are coupled to the electrons by momentum exchange collisions (which on a macroscopic scale is equivalent to a neutral plasma gaining acceleration via a $\mathbf{j} \times \mathbf{B}$ body force).

The characteristic plasma parameter calculations presented in the previous section can be used to determine how the preionized plasma emerging axially from the helicon source turns to cover the face of the acceleration coil. The electrons are magnetized (r_{ce} much less than the length scale of the transition from the helicon source to the acceleration stage). In addition, $\Omega_e > 1$, so we expect that electrons are generally tied to the field lines and follow them into the acceleration region. To maintain quasineutrality, ions must either be created in the acceleration stage through ionizing collisions with the magnetized electrons or the ions emerging from the helicon source must be turned. Furthermore, quasineutrality must be maintained on length scales greater than the Debye length. From Fig. 4.22A, we see that electron-neutral collisions have a mean free path of 3 cm, which is much greater than λ_D . Consequently, it is not likely that there are enough ionizing collisions in the acceleration stage to create ‘enough’ additional plasma to shield the potential generated by the electrons turning to follow the magnetic field, implying that the ions in the acceleration region are instead created in the helicon stage. These ions could be turned by direct momentum-transfer collisions with the electrons or through ambipolar diffusion. The average force felt by an ion due to collisions with electrons is given by[35]:

$$|F_{i(\text{coll})}| = m_e \nu_{ei} |u_e - u_i|,$$

where u_e and u_i are taken as the thermal velocities of the electrons and ions for the purpose of bounding our result. For the plasma conditions given in Table 4.5 we estimate

$$|F_{i(\text{coll})}| \sim \mathcal{O}(10^{-19}) \text{ N}.$$

The force on an ion due to ambipolar diffusion is[35]:

$$|F_{i(\text{ambipolar})}| = |e E| = \left| k T_e \frac{\nabla n_e}{n_e} \right|.$$

We can estimate that the gradient length scale is approximately equal to λ_D . This leads to

$$|F_{i(\text{ambipolar})}| \sim \mathcal{O}(10^{-14}) \text{ N},$$

which allows for the conclusion that the dominant mechanism turning the ions into the acceleration region is ambipolar diffusion.

The measurements of the induced magnetic field and azimuthal current density (referred to as the field measurements throughout this discussion) compare quite well with the current sheet visualization and analysis (referred to hereafter as the optical measurements). Both measurements indicate that, after an initial delay, a current sheet forms and moves a finite distance. Since the coil's inductance, and consequently the mutual inductance, M , between the coil and the sheet, are relatively small in the experiment, the plasma sheet dynamics are effectively driven only by dJ_{Coil}/dt . Consequently, the sheet terminates as dJ_{Coil}/dt approaches zero. Increasing the coil inductance in a real thruster will result in a current sheet with longer lifetime that also experiences additional acceleration (both processes are driven by dJ_{Coil}/dt and dM/dt).

There are two apparent discrepancies between the field and optical measurements. Examination of these apparent discrepancies leads to additional physical insight into the current sheet evolution.

The first discrepancy is the difference between the sheet velocities obtained from the magnetic field probe data (Table 4.2) and that inferred from the photographs (Table 4.3). These discrepancies may be qualitatively explained in light of the observed induced magnetic field gradient, $\partial B_r / \partial r$, which implies a weakening of the induced magnetic field, and thus a lowering of the sheet velocity, at the outer radial location (90-100 mm) where the

photographic observations were obtained, as compared to the radial location ($r = 66$ mm) where the magnetic probe measurements were made.

The second discrepancy is the difference between the axial positions of the current sheet when determined optically and from the probe data at a given time. For instance, in the baseline case at $t \approx 1.4 \mu\text{s}$, the sheet axial position is observed optically to be at about $z \approx 20$ mm from the backplate (Fig. 4.14) while the probe data (Fig. 4.10) give $z \approx 15$ mm. This can be explained by first noting from Fig. 4.5 that the applied magnetic field lines in the acceleration stage are not purely radial but are in fact tilted by about 20 degrees with respect to the backplate. This canting of the applied magnetic field should be expected to lead to a canted current sheet when the latter is initially formed. It is therefore not surprising that the initial axial position of the sheet at outer radii (where the optical measurements were made) leads the axial location of the sheet at inner radii (where the probe is located). The radially decreasing axial sheet velocity discussed in the previous paragraph may compensate somewhat for this initial canting as the sheet evolves in time.

Ideally we would like to compare the data obtained using the B -dot probes and the Langmuir probes. This comparison would yield a clear picture of the temporal and spatial evolution in both the current density and the plasma density. Unfortunately, this direct comparison is only possible for $E_{\downarrow\downarrow}$ case since we were not able to obtain Langmuir probe data for any of the higher discharge energy cases. These data are replotted in Fig. 4.23 where the current densities are plotted as solid lines and the number densities are plotted as dashed lines. Even though the B -dot probe data were acquired at the same axial locations as the number density data, the current density data, which are derived from the computation of the curl of \mathbf{B} , are located *between* the B -dot probe axial locations. This effect is somewhat mitigated by the fact that while the tip of the Langmuir probe was positioned coincident with the B -dot probe head, the Langmuir probe has a finite length equal to 2

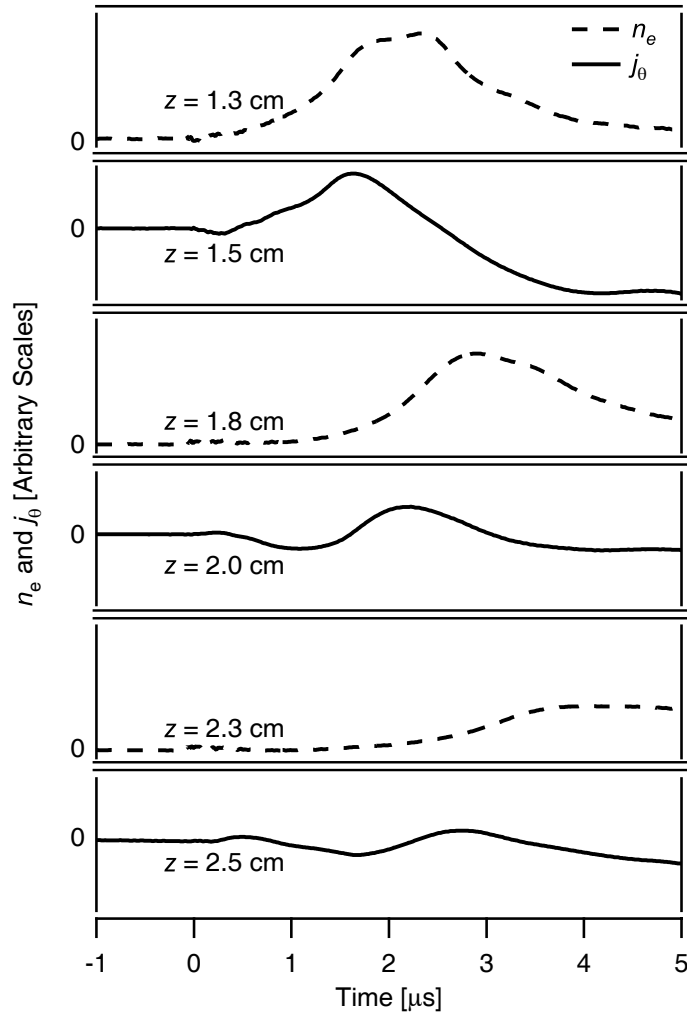


Figure 4.23: Comparison of current density measurements (from Fig. 4.10C) and plasma density measurements (from Fig. 4.17) for the E_{\parallel} case.

mm. Consequently, we can still make some meaningful observations from a comparison of the data sets in Fig. 4.23. Comparing each current density waveform to the n_e waveform plotted for the previous location (e.g. j_θ for $z = 1.5$ cm compared to n_e for $z = 1.3$ cm), we observe that both begin rising at approximately the same time. Also, even after the peak current density passes, the number density continues to rise until j_θ goes to zero, indicating that there is substantial ionization taking place in the back half of the current sheet.

The data presented in this chapter show changes in the current sheet's intensity, thickness, initial position and speed as the discharge energy, ambient background pressure and applied magnetic field are independently varied. Current sheet variations with discharge energy were explained by recalling that both J_{Coil} and dJ_{Coil}/dt directly affect the acceleration and initiation processes and that reducing the initial energy directly results in a lowering of both the coil current and the current rise rate. Up to this point, we have not offered any explanation for the following variations observed in the other cases:

- Relative to the baseline case, the sheet forms further from the acceleration coil in both the $P\downarrow$ and $P\uparrow$ cases. While the sheet is weaker in both cases, it appears to be weakest (moves slowest, is least concentrated) in the $P\uparrow$ case.
- Relative to the baseline case, the sheet forms further from the acceleration coil and is weaker (moves slower, is less concentrated) in the $B\downarrow$ case.

Even with the data we have ‘in-hand’ we can only make the following qualitative arguments to explain the observed trends. However, it seems plausible that the explanation must be tied to the initial preionized plasma distribution in the acceleration stage since the discharge energy is fixed in these cases. We begin by conjecturing that in the presence of a preionized gas, the following rules govern the inductive current sheet formation process:

1. There exists a threshold number density value (for a given dJ_{Coil}/dt) above which a strong (concentrated and localized) inductive current sheet will form. This strong sheet threshold is denoted as $(n_e)_{\text{ss}}$.
2. There exists a second threshold for weak, more diffuse current sheet formation. This threshold is denoted as $(n_e)_{\text{ws}}$ and is smaller than the strong sheet threshold.
3. The acceleration coil will inductively couple its energy into the portion of the plasma nearest the coil which fulfills the condition $n_e > (n_e)_{\text{ss}}$. If no such region exists, the

coil will inductively couple with a broad region of the plasma where $(n_e)_{ws} < n_e < (n_e)_{ss}$.

Next, we must make some assumptions regarding the preionized plasma density distributions for the various test cases. These assumptions are summarized as follows:

- The peak density in the preionized plasma's axial distribution generally follows the applied field, implying that the axial separation between the peak and the acceleration coil/coil coverplate increases with increasing radius in the proof-of-concept experiment.
- As the pressure is increased, collisions serve to both broaden the n_e distribution and lower its peak level.
- Decreasing the value of the applied magnetic field broadens and weakens the distribution of n_e , causing a drop in the peak level. Essentially, the weaker field is not as effective at turning the plasma. In the limiting case where the radial magnetic field goes to zero, none of the plasma is turned towards the acceleration coil face and no inductive current sheet forms.

Preionized plasma axial distributions (at a fixed radius) have been generated according to the assumptions listed above for the baseline, $P\downarrow$, $P\uparrow$ and $B\downarrow$ cases. These distributions, which are plotted in Fig. 4.24 along with the locations of the acceleration coil and the coil coverplate in the FARAD POCX, *are not based upon any quantitative plasma measurement*. The profiles are, however, loosely based upon the qualitative observations made in Sect. 4.2 regarding the preionized plasma density distributions for the different cases and are useful as a visual aid in our explanation of the observed trends in the data. Note that for a constant magnetic field the axial location of the peak value of n_e remains fixed. Also, as the applied magnetic field strength is reduced, the axial location of the peak density value

moves further from the acceleration coil. This is because the weaker field is less effective in turning the plasma. In addition to the plasma densities, lines corresponding to the plasma density thresholds for strong and weak current sheet formation are plotted in the figure.

The quantitative observations we made in Sect. 4.4 regarding the initial current sheet locations and relative current levels in each experimental case can be explained as follows. In the baseline case, the initial current sheet forms at the location indicated in top-left panel of Fig. 4.24 where the number density curve first intersects the line representing

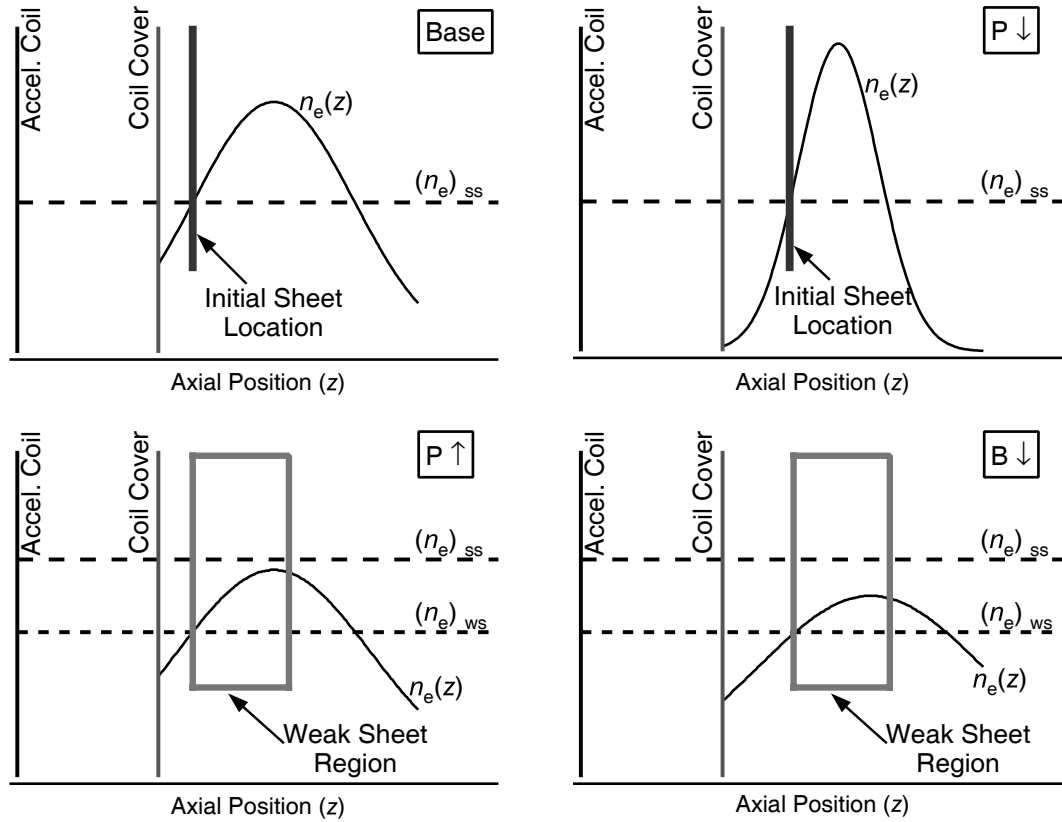


Figure 4.24: Assumed preionized plasma density axial profiles, $n_e(z)$ (at a given radial location), and initial current sheet locations for each of the listed POCX cases. The lower limit for strong current sheet formation is $(n_e)_{ss}$ and the lower limit for weak (more diffuse) current sheet formation is $(n_e)_{ws}$.

the threshold for strong sheet formation. Relative to the baseline, the peak density in the $P\downarrow$ case is greater. However, the collisionality of the plasma (specifically collisions with neutrals in the POCX) is lower, so the higher-density plasma ($n_e > (n_e)_{ss}$) extends over a smaller axial range (as indicated in top-right panel of the figure) and intersects the line representing $(n_e)_{ss}$ further downstream. Consequently, the current sheet forms further from the acceleration coil in the $P\downarrow$ case than in the baseline case. The preionized plasma in the $P\uparrow$ case (lower-left panel) is more collisional than in the baseline case. While the increased collisionality causes the plasma density to extend over a greater axial range, it also decreases the peak in the density distribution to a level that never surpasses the $(n_e)_{ss}$ threshold. Consequently, a broader, more diffuse current sheet forms beginning at the location where $n_e = (n_e)_{ws}$ and extending some axial distance away from the acceleration coil. The same reasoning can be used to explain the diffuse current sheet observed in the $B\downarrow$ case. However, in that case it is the reduced ability of the applied field to effectively turn the preionized plasma towards the acceleration coil face that results in the density distribution found in the lower-right panel. Relative to the baseline case, this distribution occupies a greater axial range and possesses a peak density which is both lower in magnitude and axially translated further downstream.

The differences in the current sheet speeds inferred for the different cases can be understood in the context of the previous arguments regarding the initial position and strength of the sheet. The induced magnetic field, and the associated Lorentz force which accelerates the current sheet, decrease with increasing axial separation from the acceleration coil. This implies that the electromagnetic force applied to the current sheet should be greater in the baseline case than the $P\downarrow$ case. It is also likely, though outside of the scope of the assumptions and discussion presented above, that the ‘strong’ sheet in the $P\downarrow$ case is weaker (more permeable to the induced field) than the ‘strong’ sheet in the baseline case because it initi-

ates further from the acceleration coil. In the cases where the current sheet is more diffuse ($P\uparrow$, $B\downarrow$), more of the induced magnetic field (relative to the baseline) should resistively diffuse through the current sheet without doing any work, leading to lower sheet speeds relative to the baseline and $P\downarrow$ cases.

4.9 Summary of Findings

A detailed experimental study was performed in the FARAD POCX to demonstrate the main features of the FARAD concept and gain physical insight into the operation of FARAD by varying different, controllable parameters. The experiment results and analysis allow us to state the following:

- The applied magnetic field allows for turning of both electrons and ions emerging from the helicon source towards the acceleration coil face.
- The presence of a preionized plasma over the acceleration coil face is essential to the formation of an inductive current sheet at discharge energies and capacitor voltages which are much lower than in previous pulsed inductive acceleration schemes (44 J/pulse versus 4 kJ/pulse in the PIT).
- Magnetic field probing allows us to infer a peak sheet speed of 12 km/s in the baseline case.
- To the extent that comparisons can be made, current sheet strengths and speeds inferred plasma density measurements generally agree with the current density measurements.
- The axial location at which the current sheet forms (relative to the glass plate covering the acceleration coil face) and the magnitude of the sheet are dependent upon the

initial preionized plasma density distribution, which, in turn, is dependent upon the background pressure and applied magnetic field strength.

- There must be a threshold preionized plasma density level above which a concentrated, magnetically impermeable current sheet will form. Furthermore, this threshold must be a function of current rise rate.

Chapter 5

Inductive Acceleration Modeling

In PPT research, there has been substantial effort devoted to the development of simple one-dimensional acceleration models (c.f. Ref. [2]). These models typically consist of a circuit equation coupled to a one-dimensional momentum equation in which propellant is accumulated, or ‘snowplowed’, by a current sheet that is accelerated by a Lorentz body force. This analysis technique has led to the identification of nondimensional scaling parameters that have proved insightful in PPT research[2, 39].

There also exists a one-dimensional pulsed inductive acceleration model similar to the type used in PPT analysis[3, 40]. This model differs from its PPT counterpart in that it must account for a second, inductively coupled circuit in the circuit equations. The nondimensionalization leads to the identification of a set of scaling parameters that are similar to those found for PPTs. There are no analytical solutions to the full set of non-dimensional governing equations, but it can be solved numerically, and accelerator performance can be predicted from the results. While this type of modeling neglects some of the more detailed physics, it is still useful in gaining a basic understanding of the scaling parameters in a pulsed inductive accelerator[41, 42]. In addition, solutions to special, limiting cases provide additional insight into the physical meaning of the scaling parameters.

We proceed with a review of the pulsed inductive acceleration model. The model is then nondimensionalized and the scaling parameters are identified and analyzed to determine how they influence the acceleration process. To further extract insight, solution sets are generated numerically by varying the parameters and computing the accelerator performance. This helps to confirm our initial physical interpretations of the scaling parameters. Finally, the model is compared with the FARAD POCX data presented in the previous chapter and used to extract additional insight.

5.1 Governing Equations

5.1.1 Circuit Equations

A lumped-element circuit model of a pulsed inductive accelerator is presented in Fig. 5.1A. This model directly applies to both the PIT and FARAD variants of a pulsed inductive accelerator. The external circuit (left side of the figure) possesses capacitance C , external inductance L_0 , resistance R_e , and acceleration coil inductance L_C . The plasma also has an inductance equal to L_C and a resistance R_p . The two circuits are inductively coupled through the acceleration coil, which acts as a transformer with mutual inductance M . The value of M is a function of the current sheet position z .

The circuit drawn in Fig. 5.1A is redrawn as an equivalent circuit in Fig. 5.1B. A set of circuit equations are written, through the application of Kirchoff's law to each loop, as:

$$\begin{aligned} (L_0 + L_C) \frac{dI_1}{dt} - \left(M \frac{dI_2}{dt} + I_2 \frac{dM}{dt} \right) + I_1 R_e &= V, \\ - \left(M \frac{dI_1}{dt} + I_1 \frac{dM}{dt} \right) + L_C \frac{dI_2}{dt} + I_2 R_p &= 0, \end{aligned} \quad (5.1)$$

where V is the voltage on the capacitor. After rearranging the equations and adding a statement for the time-rate of change of charge on the capacitor, the following coupled set

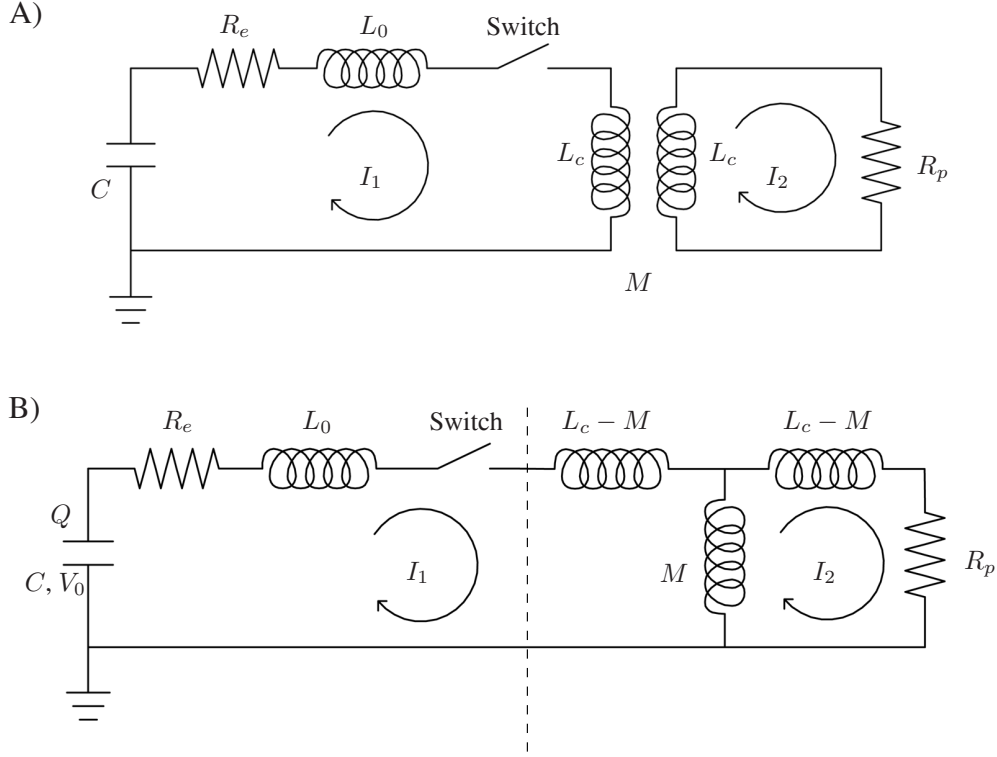


Figure 5.1: A) General lumped element circuit model of a pulsed inductive accelerator. B) Equivalent electrical circuit model (after Ref. [40])

of first-order ordinary differential equations is obtained:

$$\begin{aligned}
 \frac{dI_1}{dt} &= \frac{VL_C + (MI_1 + I_2L_C)(dM/dt) - I_2MR_p - I_1R_eL_C}{L_C(L_0 + L_C) - M^2}, \\
 \frac{dI_2}{dt} &= \frac{M(dI_1/dt) + I_1(dM/dt) - I_2R_p}{L_C}, \\
 \frac{dV}{dt} &= -\frac{I_1}{C}.
 \end{aligned} \tag{5.2}$$

In a pulsed inductive accelerator, the circuit inductance changes through the value of the time changing mutual inductance term, $M(z(t))$. The inductance downstream of L_0 and R_e (i.e. to the right of the dashed line in Fig. 5.1B), referred to as the coil terminal inductance, can be written as

$$L_{\text{term}} = (L_C - M) + \frac{1}{(1/(L_C - M)) + (1/M)},$$

which after some algebraic manipulation becomes

$$L_{\text{term}} = L_C - \frac{M^2}{L_C}. \quad (5.3)$$

The inductance of a planar, spiral inductive coil coupled to a plasma current sheet is difficult to compute analytically. However, based on experimental measurements, it has been found[40] that the inductance can be modeled using the simple exponential function

$$L_{\text{tot}}(z) = L_0 + L_C (1 - \exp(-z/z_0)), \quad (5.4)$$

where z_0 is defined as the decoupling length. Using Eqs. (5.3) and (5.4) we arrive at a solution for M as

$$M = L_C \exp\left(-\frac{z}{2z_0}\right), \quad (5.5)$$

which, when differentiated, results in the following equation that governs the changing mutual inductance of the circuit:

$$\frac{dM}{dt} = -\frac{L_C}{2z_0} \exp\left(-\frac{z}{2z_0}\right) \frac{dz}{dt}. \quad (5.6)$$

5.1.2 Momentum Equation

In the idealized ‘snowplow’ model, as the current sheet moves forward, it entrains and accelerates any gas that it encounters. The propellant mass in the current sheet as a function of time can be written as

$$m(t) = m_0 + \int_{t=0}^t \rho_A v_z dt, \quad (5.7)$$

where $\rho_A = \rho_A(z(t))$ is the linear mass density distribution and v_z is the sheet velocity. The term m_0 represents the initial mass of propellant in the sheet while the integral term represents the mass accumulated by the sheet as it moves away from the acceleration coil. Note that while the ideal snowplow model is often employed in pulsed plasma modeling,

the current sheet in a real accelerator entrains only a fraction of the total available propellant, depending largely upon the plasma properties in the current sheet.

It is well known that a magnetic force applied to a system always acts to minimize its potential energy,

$$F_j = -\frac{\partial U_m}{\partial x_j}, \quad (5.8)$$

where U_m is the magnetic potential energy defined as,

$$U_m = \frac{\Phi^2}{2L},$$

where Φ is the magnetic flux (defined as $L \cdot I$ and considered constant) and the derivative is taken in the j -th direction. Since Φ is not a function of position, the circuit will always act to maximize its inductance.

In the previous section Eq. (5.4) was written to relate the circuit inductance to the position of the current sheet. Using Eqs. (5.4) and (5.8), we can write the momentum equation as

$$\frac{L_C I_1^2}{2 z_0} \exp(-z/z_0) = \rho_A v_z^2 + m(t) \frac{dv_z}{dt}. \quad (5.9)$$

The left hand side represents the self-field electromagnetic force generated through the interaction of the current and the magnetic field. The first term on the right hand side in Eq. (5.9) represents the momentum investment associated with entraining the propellant and the second term involves further acceleration of the already entrained propellant.

5.1.3 Plasma Model

We shall not employ a plasma model in this study. However, in general, a model of the plasma is required to close the set of equations. Such detailed modeling is the subject of ongoing work in inductive plasma acceleration[43]-[45], but it is beyond the scope of the present study, which instead aims at gaining a basic understanding of the scaling in a

pulsed inductive accelerator. In previous studies[3] using the simplified, one-dimensional model described in this section, the energy equation was eliminated by explicitly assuming a value for the electron temperature that yielded a quantitative match between experimental performance data and numerical simulations. This can be done by using a Spitzer resistivity

$$\eta = 6 \times 10^{-4} T_e,$$

where T_e is in eV, and approximating the total plasma resistance as

$$R_p \simeq \frac{\pi \eta (b + a)}{\delta (b - a)},$$

where a and b are the inner and outer coil radii, respectively, and δ is the current sheet thickness. Using this same prescription, we estimate a plasma resistance between $\mathcal{O}(10\text{-}100 \text{ m}\Omega)$ in the PIT MkV.

5.1.4 Addition of an Applied Magnetic Field

The preceding acceleration model derivation is applicable to self-field pulsed inductive accelerators. However, in addition to the induced magnetic field, FARAD also possesses an applied magnetic field. To determine the applied field's effect on the acceleration process, it must be included in both the momentum and circuit equations.

The applied magnetic field interacts with the induced current to yield an additional Lorentz force on the current sheet in FARAD. The average force is written as

$$F_{\text{Applied}} = \oint_{\Gamma} I_{\theta} B_r dl = I_2 B_r \pi (b + a), \quad (5.10)$$

where $B_r = B_r(z(t))$ is an average applied radial magnetic field strength and $[\pi(b + a)]$ is the circumference based upon an average radius. Including Eq. (5.10) in the momentum equation yields:

$$m(t) \frac{dv_z}{dt} = \frac{L_C I_1^2}{2z_0} \exp(-z/z_0) - \rho_A v_z^2 + I_2 B_r \pi (b + a). \quad (5.11)$$

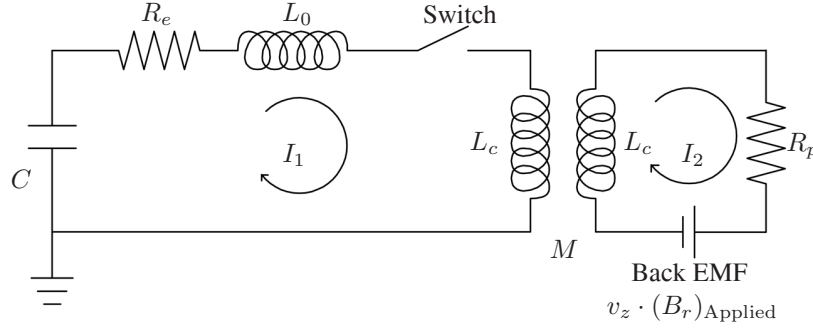


Figure 5.2: General lumped element circuit model of a pulsed inductive accelerator with the addition of an applied field back-EMF $[v_z \cdot (B_r)_{\text{Applied}}]$ term.

The acceleration arising from F_{Applied} involves the expenditure of a finite amount of power equal to $F_{\text{Applied}} \cdot v_z$. To first-order, the energy for this work comes from the stored electrical energy in the capacitor and manifests itself as a back-EMF in the plasma circuit model. This is represented as the $v_z \cdot B_r$ term in the updated circuit schematic presented in Fig. 5.2.

The addition of a back-EMF term alters the circuit equations, which are now written as:

$$\begin{aligned} \frac{dI_1}{dt} &= \frac{VL_C + (MI_1 + I_2L_C)(dM/dt) - I_2MR_p - I_1R_eL_C - v_zB_rM\pi(b+a)}{L_C(L_0 + L_C) - M^2}, \\ \frac{dI_2}{dt} &= \frac{M(dI_1/dt) + I_1(dM/dt) - I_2R_p - v_zB_r\pi(b+a)}{L_C}, \\ \frac{dV}{dt} &= -\frac{I_1}{C}, \end{aligned} \quad (5.12)$$

where the back-EMF term has been integrated over the average circumference to obtain a total voltage drop.

5.1.5 Additional Shortcomings of the Acceleration Model

We have already discussed some of the differences between the acceleration model and a real pulsed inductive thruster. The most important additional assumptions embedded in the model are that current sheet formation is immediate (at $t = 0$) and complete (does not allow the induced magnetic field to diffuse through it for all time). In experiments, while

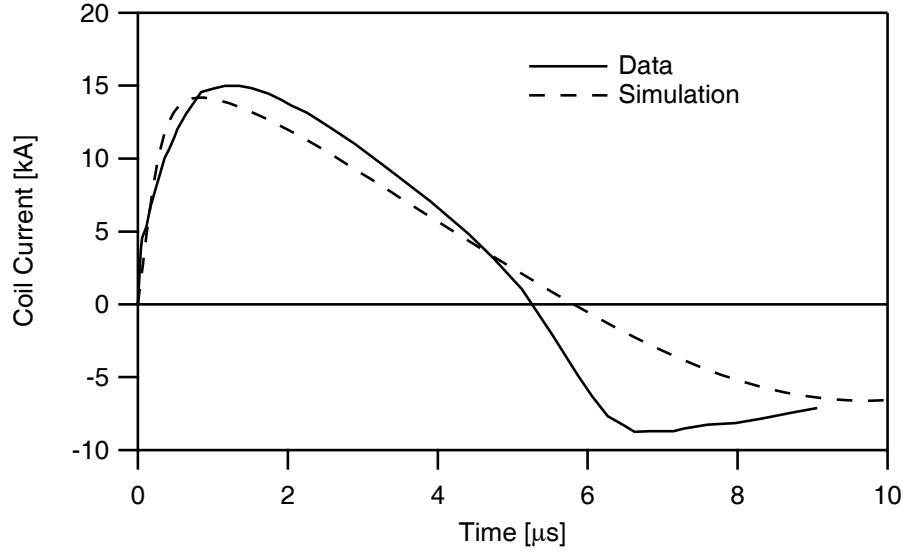


Figure 5.3: Comparison of experimentally acquired (solid line, from Ref. [46]) and numerically generated (dashed line) current waveforms in the Pulsed Inductive Thruster.

the current sheet does form quite early during the first half-cycle of the discharge, it does not form ‘immediately’ nor is it perfectly impermeable to the induced magnetic field[5]. The lack of an ionization model results in an inability to capture transient plasma physics phenomena. This is especially important during the breakdown stage, where the assumption of constant-value lumped circuit elements is violated. Evidence of this idealization is presented in Fig. 5.3 where we compare experimental data from Ref. [46] with a numerical solution to the governing equations. Though the waveforms show reasonably good agreement, we do note some departure during the initial rise which persists throughout the first half-cycle. An even greater departure starting at around $t = 5 \mu s$ is likely due to a second, ‘crowbar’ discharge forming at the coil face.

In the present work we sidestep many of the model’s shortcomings, only using it as a tool to search for relevant nondimensional scaling parameters and performance trends. We do note, however, that exhaust velocities and thruster efficiencies predicted by one-

dimensional, circuit-based acceleration models, even with all their shortcomings, show good qualitative and quantitative agreement with experimental performance data for both inductive thrusters[3] and PPTs[39].

5.2 Nondimensional Equations

Following Ziemer and Choueiri's modeling of a PPT[39], we nondimensionalize the inductive accelerator's set of governing equations in an attempt to identify relevant scaling parameters and find their optimum values. However, differences between the models for these two accelerators arise due to the following:

1. In the inductive accelerator there are two dependent current loops while there is only the one loop in the PPT.
2. The mutual inductance term also does not appear in PPT modeling; however it is essential to the coupling between the two current loops in an inductive accelerator.
3. The model presented here has an applied magnetic field which gives rise to an additional Lorentz force acceleration term in the momentum equation and a back-EMF term in the plasma circuit equation.

We also recall that the inductive acceleration model we are employing lacks a model of the plasma. Our strategy of finding non-dimensional scaling parameters and searching for physical insight instead of attempting to exactly model an accelerator allows us to bypass this issue. As an exercise, we could simply vary any dimensionless parameter which contains R_p to determine the sensitivity of the acceleration process.

The following dimensionless terms can be readily selected as a starting point based upon prior knowledge of PPT scaling laws:

$$\begin{aligned} I_1^* &= \frac{1}{V_0} \sqrt{\frac{L_0}{C}} I_1, & I_2^* &= \frac{1}{V_0} \sqrt{\frac{L_0}{C}} I_2, \\ t^* &= \frac{t}{\sqrt{L_0 C}}. \end{aligned} \quad (5.13)$$

In the course of nondimensionalizing the governing equations the following additional nondimensional variables naturally appear in the equation set:

$$\begin{aligned} z^* &= \frac{z}{z_0}, & V^* &= \frac{V}{V_0}, \\ M^* &= \frac{M}{L_C}, & v_z^* &= \frac{\sqrt{L_0 C}}{z_0} v_z. \end{aligned} \quad (5.14)$$

In the framework of Eq. (5.7), the propellant can either be loaded as a slug mass ($\rho_A = 0$ for all z) or as some function of position ($\rho_A = \rho_0 f(z)$). If the propellant is loaded as a slug mass and we nondimensionalize by the propellant mass per shot, m_{bit} , the non-dimensional mass accumulation statement can be written as

$$m^* = \frac{m(t)}{m_{\text{bit}}} = 1 \quad \text{for all time.} \quad (5.15)$$

For a propellant loading which is a function of z we obtain the statement

$$m^* = m_0^* + \int_0^{t^*} \rho^* f(z^*) v_z^* dt^*, \quad (5.16)$$

where $m_0^* = m_0/m_{\text{bit}}$ and $\rho^* = \rho_0 z_0/m_{\text{bit}}$.

Writing Eqs. (5.6), (5.11), (5.12) and (5.16) in terms of the dimensionless variables and in differential form, we obtain

$$\frac{dI_1^*}{dt^*} = \frac{L^* V^* + (M^* I_1^* + I_2^*) (dM^*/dt^*) - I_2^* M^* L^* \psi_2 - I_1^* L^* \psi_1 - L^* v_z^* M^* \nu}{(L^* + 1) - (M^*)^2}, \quad (5.17a)$$

$$\frac{dI_2^*}{dt^*} = M^* \frac{dI_1^*}{dt^*} + I_1^* \frac{dM^*}{dt^*} - I_2^* L^* \psi_2 - v_z^* L^* \nu, \quad (5.17b)$$

$$\frac{dV^*}{dt^*} = -I_1^*, \quad (5.17c)$$

$$\frac{dM^*}{dt^*} = -\frac{1}{2} \exp\left(-\frac{z^*}{2}\right) v_z^*, \quad (5.17d)$$

$$\frac{dz^*}{dt^*} = v_z^*, \quad (5.17e)$$

$$\frac{dv_z^*}{dt^*} = [\alpha (I_1^*)^2 \exp(-z^*) - \rho^* f(z^*) (v_z^*)^2 + \gamma I_2^*] / m^*, \quad (5.17f)$$

$$\frac{dm^*}{dt^*} = \rho^* f(z^*) v_z^*. \quad (5.17g)$$

The relevant scaling parameters which emerge from the system of equations are defined as:

$$\begin{aligned} L^* &= \frac{L_0}{L_C}, & \psi_1 &= R_e \sqrt{\frac{C}{L_0}}, \\ \psi_2 &= R_p \sqrt{\frac{C}{L_0}}, & \alpha &= \frac{C^2 V_0^2 L_C}{2 m_{\text{bit}} z_0^2}, \\ \nu &= \frac{\pi (a+b) B_r z_0}{V_0 \sqrt{L_0 C}}, & \gamma &= \frac{\pi (a+b) B_r V_0 C^{3/2} L_0^{1/2}}{m_{\text{bit}} z_0}. \end{aligned} \quad (5.18)$$

The initial conditions for the set of nondimensional differential equations are:

$$\begin{aligned} I_1^*(0) &= 0, & I_2^*(0) &= 0, \\ V^*(0) &= 1, & M^*(0) &= 1, \\ z^*(0) &= 0, & v_z^*(0) &= 0, \\ m^*(0) &= \frac{m_0}{m_{\text{bit}}}. \end{aligned}$$

Note that when the propellant is loaded like a slug, the right hand side of Eq. (5.17g) and the second term on the right hand side of Eq. (5.17f) disappear ($\rho^* = 0$).

5.3 Interpretation of the Scaling Parameters

5.3.1 Inductance Ratio: L^*

It is well known[47] that the efficiency of a pulsed electromagnetic accelerator cannot exceed the fractional change of inductance, $\Delta L/L_0$. This ratio is a measure of the fraction of energy that can be deposited into electromagnetic acceleration of the gas. Recognizing from Eq. (5.4) that L_C is equal to the total inductance change available to the accelerator (i.e. $L_C = \Delta L$) allows us to write $(L^*)^{-1} = \Delta L/L_0$. Consequently, we expect the value of L^* to be less than unity in an efficient pulsed inductive accelerator.

5.3.2 Critical Resistance Ratios: ψ_1 and ψ_2

Like their counterpart found in the gas-fed PPT literature[39], the ratios ψ_1 and ψ_2 appear in the circuit equations and control the nature of the current waveforms.

To determine the physical meanings of ψ_1 and ψ_2 , we attempt to find limiting solutions to Eqs. (5.17a)-(5.17c). Decoupling the current sheet dynamics (i.e. the acceleration and sheet motion) from the problem allows us to apply the following condition:

$$M^* = 1,$$

which dramatically simplifies the circuit equations. Under this assumption the circuit equations can be rewritten as:

$$\begin{aligned} \frac{d^2 I_1^*}{dt^{*2}} + (\psi_1 + \psi_2) \frac{dI_1^*}{dt^*} + I_1^* &= \psi_2^2 L^* I_2^*, \\ \frac{dI_1^*}{dt^*} - \frac{dI_2^*}{dt^*} &= \psi_2 L^* I_2^*. \end{aligned} \quad (5.19)$$

If the right hand side of the first equation is small (≈ 0), then the solution for I_1^* is

$$I_1^* = A_0 \exp(-\Psi t^*) \sin\left((1 - \Psi^2)^{1/2} t^*\right),$$

where we have introduced the new dimensionless parameter $\Psi \equiv (\psi_1 + \psi_2)/2$. The solution is underdamped (ringing) for $\Psi < 1$, critically damped for $\Psi = 1$, and overdamped for $\Psi > 1$. If the right hand side in the second of Eqs. (5.19) is also small, then the induced current in the plasma mirrors the current in the coil:

$$I_2^* = I_1^*.$$

The fact that the current waveform depends on the sum of ψ_1 and ψ_2 implies that within a portion of the (ψ_1, ψ_2) parameter space, contours of constant performance should generally follow the contours given by the equation

$$(\psi_1 + \psi_2)/2 = \text{constant}.$$

To neglect the non-linearities present in the circuit equations and arrive at the limiting solutions given above, the values of L^* and ψ_2 must be such that

$$\begin{aligned}\psi_2^2 L^* &\ll 1, \\ \psi_2 L^* &\ll 1.\end{aligned}$$

Therefore, we expect a feature or transition in a contour plot of accelerator performance as either $\psi_2^2 L^*$ or $\psi_2 L^*$ approaches unity.

5.3.3 Dynamic Impedance Parameter: α

The dynamic impedance parameter α is similar to the one found in the PPT literature[2, 39]. Following Jahn[2], we can write α as the product of several important ratios:

$$\alpha = \frac{C^2 V_0^2 L_C}{2m_{\text{bit}} z_0^2} = \frac{1}{8\pi^2} \frac{C V_0^2/2}{m_{\text{bit}} v_z^2/2} L^* \left(\frac{2\pi\sqrt{L_0 C}}{L_0/\dot{L}} \right)^2,$$

where \dot{L} is the dynamic impedance which is defined as $v_z L'$ and L' is defined as an effective inductance per unit length equal to L_C/z_0 . The ratios written on the right hand side of the first line are identified as:

- The ratio of the initial stored energy to the plasma kinetic energy, which is also the inverse of thrust efficiency. This term will always be greater than one.
- The inductance ratio, L^* , which will typically be less than one in an efficient electromagnetic accelerator.
- The ratio of the resonant period of the unloaded circuit, $2\pi\sqrt{L_0C}$, to the time it takes for the circuit to increase its inductance by L_0 , which is equal to L_0/\dot{L} .

The term L_0/\dot{L} is essentially the timescale on which the current sheet remains in the acceleration region before decoupling from the coil (i.e. residence time). The term $2\pi\sqrt{L_0C}$ is the timescale on which the external circuit naturally operates. When the ratio of the circuit timescale to the residence time is small ($\ll 1$), the external circuit attempts to transfer its energy faster than the current sheet can accept it, leading to an inefficient acceleration process. On the other hand, when the ratio of the timescales is large ($\gg 1$), the sheet moves away from the acceleration coil quickly, exiting the acceleration region and decoupling before the external circuit can transfer the maximum amount of energy to the sheet. Between these two cases exists an optimum value of α where the current sheet's residence timescale is matched to the external circuit, allowing for optimum transfer of stored electrical energy into directed kinetic energy.

5.3.4 Applied Field Acceleration Parameter: γ

The applied field acceleration parameter is a new term that has not been included in previous pulsed plasma acceleration models. In keeping with the spirit of the analysis performed to understand α , we can recast γ as a set of important ratios. Following this strategy, we write:

$$\gamma = \frac{\pi (b + a) B_r V_0 C^{3/2} L_0^{1/2}}{m_{\text{bit}} z_0} = \frac{1}{4\pi^2} \frac{C V_0^2 / 2}{m_{\text{bit}} v_z^2 / 2} L^* \left(\frac{2\pi\sqrt{L_0C}}{L_0/\sqrt{\dot{L}_B \dot{L}}} \right)^2,$$

where \dot{L}_B is the dynamic impedance due to the applied field and is defined as $v_z \dot{L}'_B$. The term \dot{L}'_B is an effective applied field inductance per unit length equal to L_B/z_0 . The effective applied field inductance is defined as

$$L_B \equiv \frac{B_r}{V_0 \sqrt{C/L_0}} [z_0 \pi (b + a)] = \frac{B_r}{I_{\text{char}}} \cdot \text{Area},$$

and represents the ‘inductance’ added to the system by the applied magnetic field. The characteristic current I_{char} is that previously used to nondimensionalize I_1 and I_2 .

There is a remarkable degree of symmetry between the ratios identified in γ and those previously identified in α . The only difference is the term $L_0/\sqrt{\dot{L}_B \dot{L}}$. This term is still representative of the time it takes for the circuit to increase its inductance by L_0 . However, the appearance of an average dynamic impedance, $\sqrt{\dot{L}_B \dot{L}}$, indicates that this time is now a function of both the acceleration due to the induced magnetic field through \dot{L} and the applied field acceleration through \dot{L}_B .

5.3.5 Applied Field Back-EMF Parameter: ν

The term ν arises from the inclusion of an applied-field induced back-EMF in the circuit equations. Based upon the analysis of γ , we notice that a collection of terms similar to those comprising in L_B previous section can be identified in ν . This allows us to write:

$$\nu = \frac{\pi (a + b) B_r z_0}{V_0 \sqrt{L_0 C}} = \frac{L_B}{L_C} \frac{1}{\dot{L}^*}.$$

It is interesting that ν can be recast as the ratio of the effective applied magnetic field inductance to the coil inductance. As was found in the analysis of γ , we see that the relative magnitudes of the effective applied field inductance, L_B , and the coil inductance, L_C , are the primary indicator of the importance of the applied field to the acceleration process.

5.4 Nondimensional Solutions

5.4.1 Solution Strategy

The set of coupled first-order ODEs given in Eqs. (5.17) can be solved numerically once the mass distribution and the set of scaling parameters given in Eqs. (5.18) are specified. The performance metrics chosen for this study are the exhaust velocity, v_z^* , and the thrust efficiency, which is written in terms of nondimensional parameters as

$$\eta_t = \frac{m^* v_z^*}{2L^* \alpha}.$$

In solving any set of first-order (in time) differential equations, it is important to know when the time histories of the computed variables (specifically v_z^* in our case) should be queried to calculate performance. This question is, in fact, critical to the evaluation of these accelerators. For our non-dimensional model, the integration period will end when one of the two following conditions is reached:

1. The end of the first half-cycle of the accelerator coil discharge is reached and the current I_1^* reverses in sign.
2. The sheet travels three characteristic lengths, $z^* = 3$.

The first condition above is based on the fact that when the accelerator current goes through zero, it is going through a point of high dI_1/dt . While the acceleration model doesn't incorporate any ionization physics, it is well known that a new current sheet can form at the face of the coil when I_1 reverses, causing what is known as a “crowbar discharge”. If this occurs, the initial current sheet ceases to undergo acceleration.

The second condition stems from the existence of a finite axial distance between the current sheet and the coil, beyond which the two are essentially decoupled electrically. The separation distance $z^* = 3$ is chosen as our cutoff for electromagnetic coupling as it

represents an inductance change in the circuit of 95% of the coil inductance. Above this cutoff value, the integration yields no significant change to the calculated performance.

If the propellant is not loaded as a slug mass, more effort may be required to include propellant utilization inefficiencies in the total thrust efficiency. To do this, the velocity must be allowed to continue to evolve until all the available mass is entrained by the sheet. However, it should be clear from the above conditions that the calculation may halt before this occurs. If this is the case, the unentrained mass represents a mass utilization inefficiency in the acceleration scheme and the final values of v_z^* and m^* must be corrected to reflect this fact.

The correction begins by realizing that once the sheet is “decoupled”, there is no mechanism by which it can transfer impulse to the thruster. However, we shall assume that the sheet continues to entrain the mass it encounters. When the computation is halted, the current sheet has entrained an amount of mass equal to m_f^* and moves at a velocity equal to $(v_z^*)_f$, where the subscript f is used to indicate that these values are the final data points obtained from the numerical solution. The total mass available to the sheet is m_{bit}^* . Conservation of linear momentum is used to compute the corrected sheet velocity as

$$v_z^* = \frac{m_f^*}{m_{\text{bit}}^*} (v_z^*)_f. \quad (5.20)$$

5.4.2 Solutions

We present contour plots of computed performance (v_z^* and η_t) found by solving the nondimensional governing equations while varying the values of the various similarity parameters. The results are presented primarily for a slug mass loading ($\rho_A = 0$). The slug mass loading, while not physically realizable in a gas-fed system, allows for the exploration of the parameter space while minimizing the effects of the mass distribution on the acceleration scheme. The results from the slug mass loading are compared to a uniform fill

($\rho_A = \text{constant}$ for z^* between zero and three) and a triangular mass distribution equivalent to that found in the PIT[3] and given by

$$\rho_A = \begin{cases} \rho_0 (1 - z/\delta_m) & z \leq \delta_m \\ 0 & z > \delta_m \end{cases}$$

where $\delta_m/z_0 \approx 0.53$ in the PIT MkV. In all data sets, the baseline values of the nondimensional parameters are $L^* = 0.121$, $\psi_1 = 0.05$, $\psi_2 = 0.13$ and $\alpha = 2.1$. These values roughly correspond to those found in the PIT MkV accelerator[3].

Contour plots of computed efficiency and nondimensional exhaust velocity are presented for varying values of α and ψ_1 (Fig. 5.4A-B), α and ψ_2 (Fig. 5.4C-D), ψ_1 and ψ_2 (Fig. 5.5A-B), and ψ_2 and L^* (Fig. 5.5C-D). We observe several important trends in these data.

First, in Figs. 5.4A,C, we see that the efficiency possesses a local maximum with respect to α . Also, Figs. 5.4B,D show increasing sheet velocity with increasing α , implying a decrease in the residence timescale of the current sheet in the acceleration region. These observations are consistent with our interpretation of α as a dynamic impedance matching parameter.

Efficiency and exhaust velocity increase with decreasing ψ_1 and ψ_2 (Figs. 5.5A-B). This trend will be discussed in more detail in the next section. In addition, efficiency also increases with decreasing L^* showing the importance of increasing the fractional inductance change in a pulsed electromagnetic accelerator.

In Figs. 5.4C-D and 5.5A-B, we observe a transition point in the solution near $\psi_2 = 3$. This transition is marked by a dashed line in the plots. Similarly, a transition in the solution form is marked by a dashed line in Figs. 5.5C-D. In Sect. 5.3 we discussed the physical meanings and interrelationships between ψ_1 , ψ_2 and L^* by linearizing the circuit equations and finding solutions to a limiting case. We found that this linearization held when $\psi_2^2 L^* \ll$

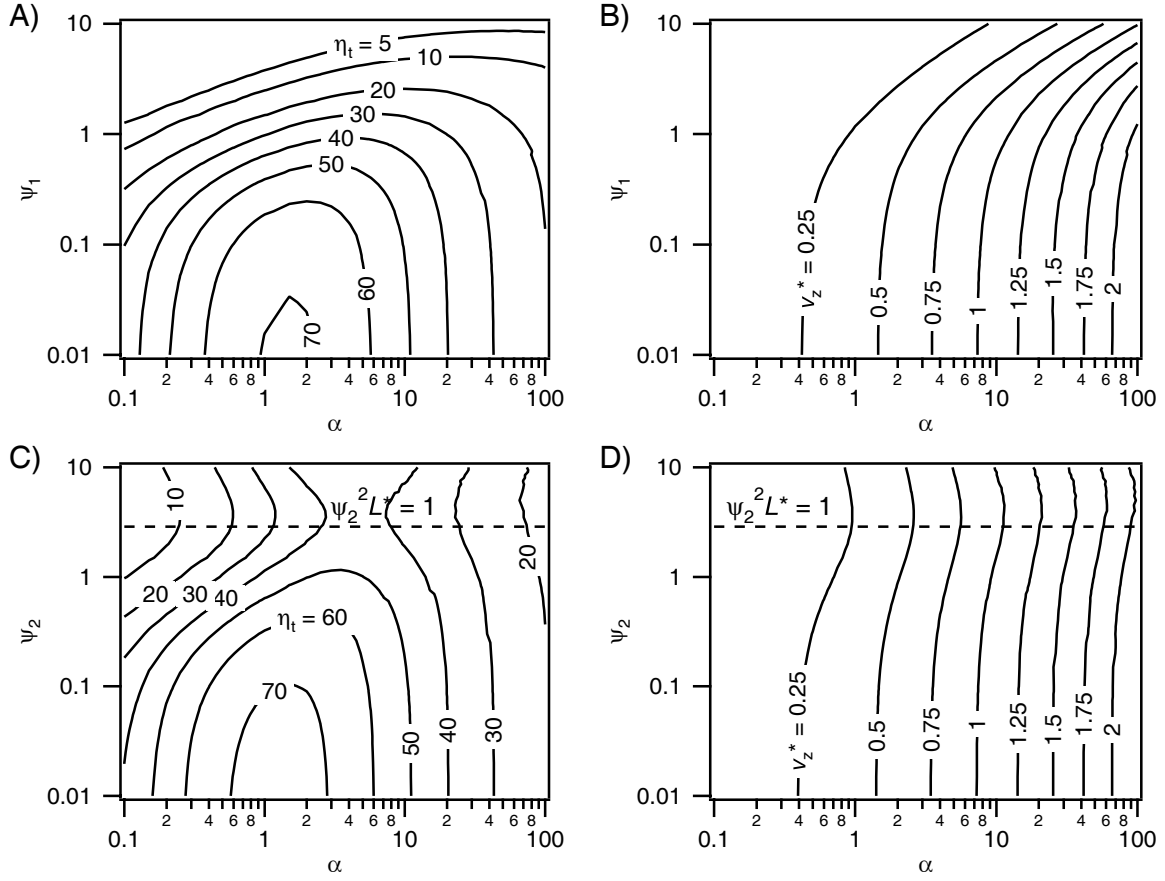


Figure 5.4: Contour plots of inductive accelerator efficiency and non-dimensional exhaust velocity for a slug mass loading found while varying: A) and B) α and ψ_1 , C) and D) α and ψ_2 . The other nondimensional values used to compute these data are: plots A) and B) $\psi_2 = 0.13$, $L^* = 0.121$; plots C) and D) $\psi_1 = 0.05$, $L^* = 0.121$. In all plots, $\gamma = \nu = 0$.

1 and $\psi_2 L^* \ll 1$. For the present value of L^* , the former requirement is more stringent. In Figs. 5.4C-D and 5.5A-D, a dashed line given by the equation $\psi_2^2 L^* = 1$ is plotted. As the values of either ψ_2 or L^* increase, the non-linear interactions between I_1 and I_2 increasingly affect the solution causing the time-history of I_2 to increasingly deviate from that of I_1 . The same analysis showed that the quantity $\Psi = (\psi_1 + \psi_2)/2$ was important in determining the oscillatory nature of the current waveforms. We speculated that so long as the linearizing assumptions held, contours of constant performance should follow contours

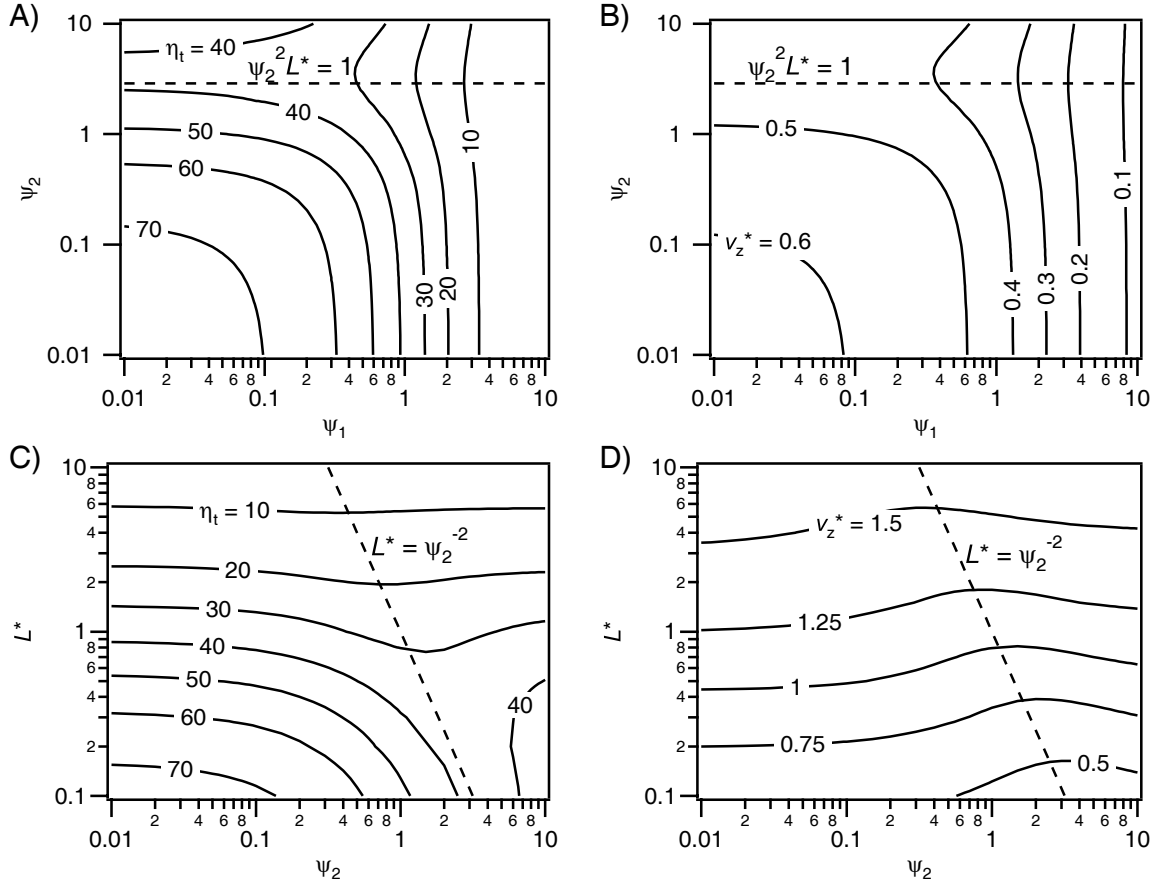


Figure 5.5: Contour plots of inductive accelerator efficiency and non-dimensional exhaust velocity for a slug mass loading found while varying: A) and B) ψ_1 and ψ_2 , C) and D) ψ_2 and L^* . The other nondimensional values used to compute these data are: plots A) and B) $\alpha = 2.1$, $L^* = 0.121$; plots C) and D) $\alpha = 2.1$ and $\psi_1 = 0.05$. In all plots, $\gamma = \nu = 0$.

of Ψ equal to a constant. In general, we observe this to be true in the lower left hand corners of Figs. 5.5A-B.

Additional contour plots showing performance variation for different propellant loadings are presented in Fig. 5.6. We observe that propellant loading has a large influence on the thrust efficiency, going from a maximum of 70% for a slug mass (Fig. 5.4A) to 50% for a triangular mass loading (Fig. 5.6A) and 16% for a uniform fill (Fig. 5.6B). These extreme cases help emphasize the detrimental effects of drag on the current sheet as it en-

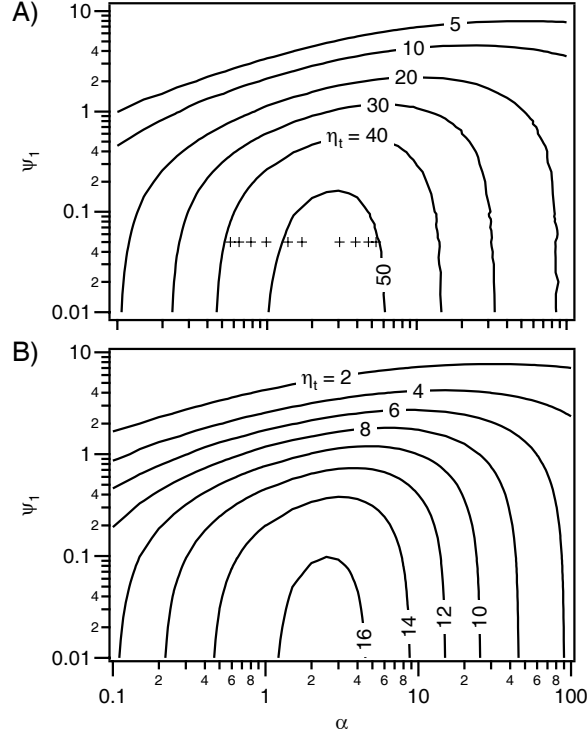


Figure 5.6: Contour plots of inductive accelerator efficiency for A) a triangular mass distribution and B) a uniform mass distribution. The fixed nondimensional parameters in these computations are $\psi_2 = 0.13$, $L^* = 0.121$. Points corresponding to the nondimensional parameters found in the PIT MkV[3] are plotted in A) and are indicated by “+” symbols. The measured thrust efficiencies associated with these points compare quite favorably with the computed performance contours. In all plots, $\gamma = \nu = 0$.

trains propellant. The performance is especially poor in the uniform fill case since much of the propellant is acquired after the circuit experiences a significant increase in inductance. Consequently, a current sheet with substantial velocity but little momentum propagates into the remaining propellant and experiences significant drag (drag force $\propto (v_z^*)^2$) while at the same time the driving force is decreasing exponentially with increasing axial position.

It is interesting to note that there is only a small amount of variation in the value of α that yields peak efficiency when comparing Figs. 5.4A and 5.6. The peak slowly shifts from α between 1 and 2 for a slug mass loading to between 2 and 3 for the uniform fill. The corresponding nondimensional parameters for PIT MkV data are plotted as “+” symbols in

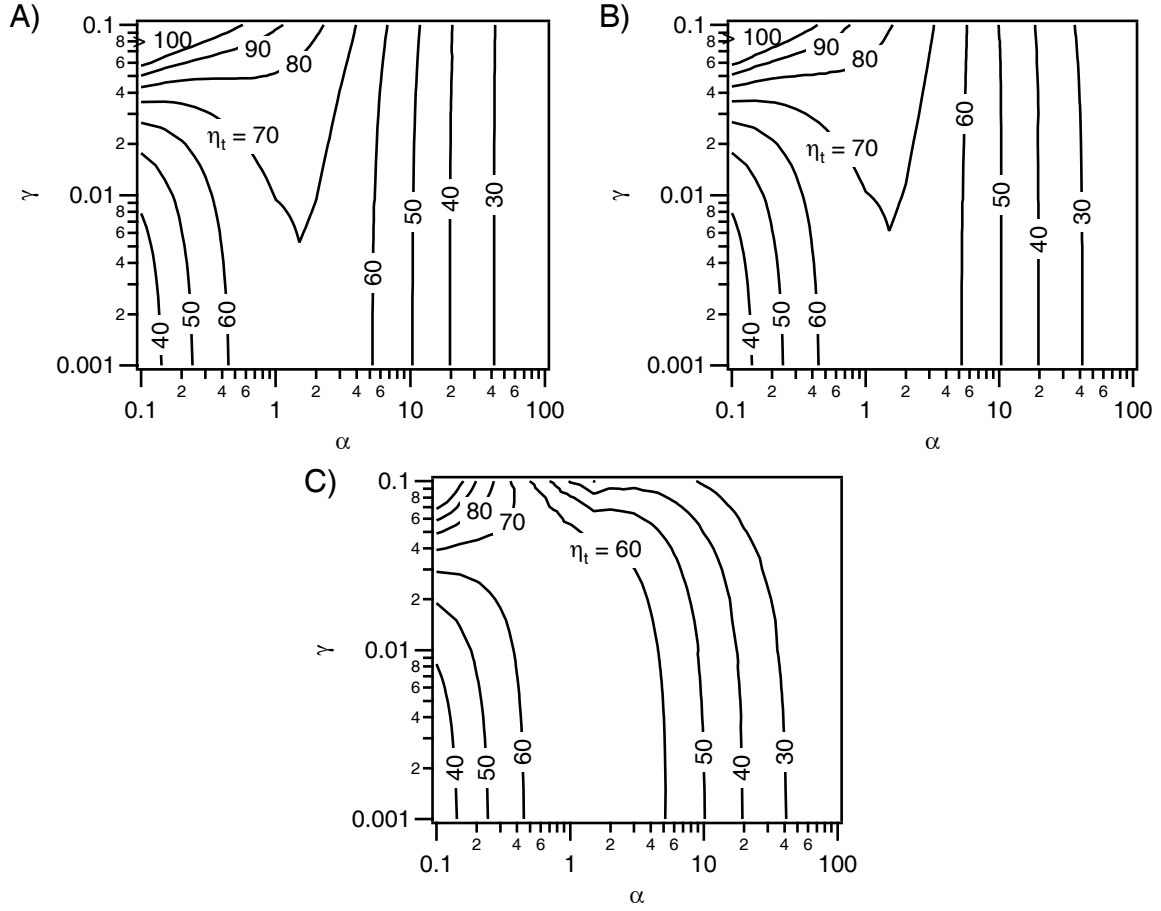


Figure 5.7: Contour plots of inductive accelerator efficiency for a slug mass loading found while varying γ and α . The plots have been generated for the cases A) $\nu = 0.1\gamma$, B) $\nu = \gamma$ and C) $\nu = 10\gamma$. The other nondimensional values used to compute these data are: $L^* = 0.121$, $\psi_1 = 0.05$, $\psi_2 = 0.13$.

Fig. 5.6A and the measured thrust efficiencies associated with these points compare quite favorably with the computed performance contours in that graph. These data also show that the optimum α values are easily accessible experimentally.

In Fig. 5.7, contour plots of computed thrust efficiency are presented for cases in which there is an applied radial magnetic field. These plots were generated for three separate cases in which we assumed that the dimensionless parameter ν was proportional to γ , with $\nu = 0.1\gamma$ in Fig. 5.7A, $\nu = \gamma$ in 5.7B and $\nu = 10\gamma$ in 5.7C. These plots show for all

three cases that there is very little change in the performance as the applied magnetic field is increased (increasing γ). In fact, the only region which exhibits any effect at all is where γ is high and α is low. Here, we observe efficiencies increasing dramatically to values over 100%. Obviously, in this region the assumptions of the model are violated. Specifically, we did not include the energy to generate such a strong magnetic field in our acceleration model or efficiency calculation.

The conclusion we can draw from Fig. 5.7 is that, in general, the induced magnetic field and subsequent acceleration dominate any additional acceleration which may arise due to the induced current interacting with the applied field. Physically, the region of low α can be thought of as representing either a low initial energy per unit mass of propellant or a low rate of electromagnetic acceleration. In regions of very high γ and low α , the current level in the acceleration coil is most likely too low to induce a sufficient azimuthal plasma current across the applied magnetic field lines for a current sheet to form. In this part of the parameter space, the one-dimensional modeling assumptions are not valid and no further inferences from the trends should be drawn.

5.5 Implications of the Results

Several observations made in the previous section lead directly to ways in which the performance of a pulsed inductive accelerator can be improved. First, an accelerator can achieve maximum efficiency when operated at or near values of α which allow for a good dynamic impedance match. It was shown in Figs. 5.4A and 5.6 that the optimum occurs when $1 \leq \alpha \leq 3$.

The value of L^* should be as low as possible to allow for as much electromagnetic acceleration as possible. In addition, the exhaust velocity can be increased by increasing the value of α .

The scaling with ψ_1 and ψ_2 is somewhat counterintuitive based on previous experience with pulsed plasma thrusters[48]. In PPTs the thrust efficiency decreases as a function of an increasing critical resistance ratio, which is similar to what we observe in Figs. 5.4A,C and 5.5A. However, unlike the trends in PPT scaling where the thruster exhaust velocity decreases with decreasing ψ [48], the dimensionless exhaust velocity remains fairly constant as either ψ_1 or ψ_2 are varied independent of each other (Figs. 5.4B,D). This is because the term that really matters in controlling the discharge waveform is Ψ (see Sect. 5.3.2). In addition, the dimensionless exhaust velocity actually *increases* as *both* ψ_1 and ψ_2 (or Ψ) decrease in value (Fig. 5.5B). Based on this scaling we must ask ourselves if we should attempt to operate a real pulsed inductive accelerator in the low ψ_1, ψ_2 regime.

Plotted in Fig. 5.8 are computed time histories of the various nondimensional parameters. To generate these curves, the equation set was integrated for different values of $\psi_1 = \psi_2$ while maintaining α and L^* constant. We observe two features in these data. The first is that the current waveforms do ring more as the values of ψ_1 and ψ_2 are decreased. This is evidenced in the peak currents achieved (both I_1^* and I_2^*) and the amount of voltage reversal after the first half-cycle and is an expected result based upon the analysis which yielded Eq. (5.20) and the dimensionless parameter Ψ . However, even though the circuit rings more (i.e. more energy returns to the capacitor at the end of the first half-cycle) the directed kinetic energy of the sheet and the thrust efficiency also increase as ψ_1 and ψ_2 decrease.

To explain this, we first note that α is invariant in these solution sets. Taking the interpretation of α as the dynamic impedance allows us to state, in rough terms, that the source (driving circuit) and the load (current sheet) are still approximately matched in all three cases plotted in Fig. 5.8. Consequently, we still obtain a high degree of energy transfer between the circuit and the load, even as ψ_1 and ψ_2 are decreased in value. This is why the

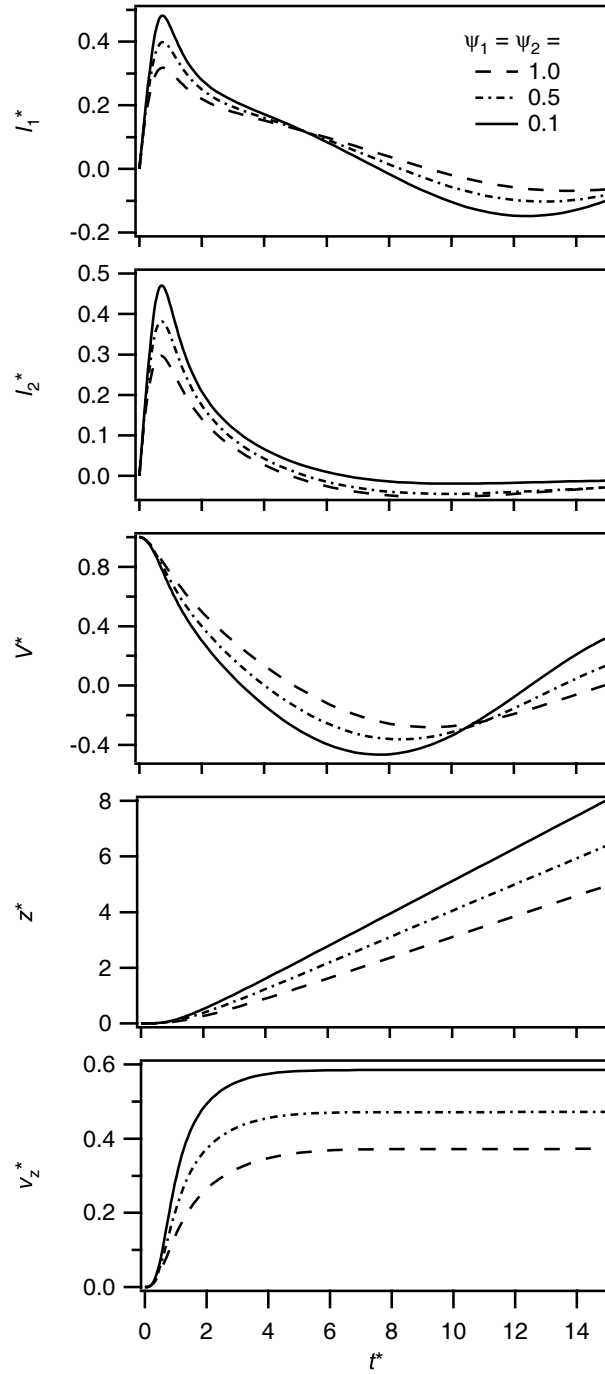


Figure 5.8: Time histories of the various computed parameters in a pulsed inductive accelerator for different values of $\psi_1 = \psi_2$. The slug mass loading is employed and the values of α and L^* are 2.1 and 0.121, respectively. ($\gamma = \nu = 0$)

solutions for the three cases, especially those for I_1 and I_2 , while differing in magnitude, qualitatively behave in a similar fashion.

To explain the increase in exhaust velocity and thrust efficiency with decreasing ψ_1 and ψ_2 , we first recall that in pulsed plasma thrusters

$$\text{Impulse Bit} \sim \int I^2 dt.$$

As the PPT circuit is adjusted from underdamped to critically damped, the peak current decreases. However, the total integral, and hence the impulse bit, and to some extent the thrust efficiency, can be conserved. On the other hand, in a pulsed inductive accelerator

$$\text{Impulse Bit} \sim \int I_1^2 e^{-z(t)} dt.$$

This indicates that to improve the impulse bit and thrust efficiency, the current must peak while the sheet is still close to the back-end of the accelerator (i.e. near $z = 0$). The force accelerating the sheet drops exponentially as the sheet moves away from $z = 0$, *even if the peak current is maintained*. Therefore, to achieve efficient pulsed inductive acceleration, the highest possible peak current must be reached before the sheet moves far from $z = 0$. This implies that any attempts to lower the peak current and extend the current pulse length (either by increasing ψ_1 and ψ_2 to obtain a critically damped circuit or through the use of solid-state switching technology) will result in a less efficient acceleration process with a higher fraction of the total energy lost in the circuit through resistive dissipation.

There are several reasons why PPTs typically avoid the low critical resistance ratio, underdamped circuit regime. The missions for which PPTs are best suited require high specific impulse, so the exhaust velocity must be high. Also, the ringing circuit can result in a large voltage reversal, which can be damaging to the lifetime of the capacitor. In addition, ringing circuits can result in crowbar discharges, which short-circuit the acceleration process before the current sheet reaches the ends of the electrodes.

In pulsed inductive accelerators, the problem of crowbar discharges can be avoided by maintaining a good dynamic impedance match. High specific impulses and efficiencies are realized in the low ψ_1, ψ_2 circuit configuration. The only remaining concern pertains to the capacitor voltage reversal. The voltage reversal for the data presented in Fig. 5.8 ranges from 20% of the maximum charge for $\psi_1 = \psi_2 = 1$ to 40% of the maximum charge for $\psi_1 = \psi_2 = 0.1$. It may be possible to reduce this by adjusting the values of L^* and α slightly. This implies that for high performance, a pulsed inductive accelerator should be operated in a highly underdamped mode. This may require the capacitor to handle a higher voltage reversal than in the critically damped mode.

5.6 Comparison with FARAD POCX Results

We attempt to use the acceleration model to simulate the FARAD experimental data presented in Chapter 4. The aim is to see if the acceleration model provides any additional physical insight into the trends in the data.

A matrix of the experimental conditions, which were previously presented in Table 4.1, are repeated for convenience in Table 5.1. The fixed circuit parameters used in modeling the

Table 5.1: Summary of the experimental conditions tested in the FARAD proof-of-concept experiment (repeated from Table 4.1).

	Designation	$V_0 (E_0)$ [V (J)]	p_0 [mTorr]	B_r [Gauss]
Case #1	Base	2000 (78.5)	23	160
Case #2	E↓	1750 (60)	23	160
Case #3	E↓↓	1500 (44)	23	160
Case #4	P↓	2000 (78.5)	7.5	160
Case #5	P↑	2000 (78.5)	48	160
Case #6	B↓	2000 (78.5)	23	80

Table 5.2: Fixed parameters used to simulate the acceleration process in the FARAD proof-of-concept experiment and the corresponding nondimensional parameters for the baseline case.

L_0	90 nH	L^*	4.5
L_C	20 nH	ψ_1	0.9
R_e	43 m Ω	ψ_2	0.2
R_p	10 m Ω	α	5.5
C	39.2 μ F	γ	0.16
z_0	2 cm	ν	3.3×10^{-3}
		m_0^*	0.1

FARAD data are given in the left-hand column of Table 5.2. The non-dimensional parameters representative of the baseline case are given in the right-hand column of the same table. The parameters L_0 , L_C , R_e , C , and z_0 are known to a great degree of certainty because they are relatively easy to measure. It is much more difficult to measure the plasma resistance, R_p , because it can change during the discharge (recall that we assumed a constant value of R_p in the course of our acceleration modeling). However, we have a reasonably high degree of confidence that the order of magnitude is accurate[23] and we know from our previous modeling that the performance is relatively insensitive to variations in R_p (through ψ_2).

5.6.1 Accelerator Coil Current

The easiest portion of the experimental data to simulate is the accelerator coil current, I_1 . This simulation is significantly simplified in the FARAD POCX because the coil inductance, and consequently the change in inductance over the acceleration stroke length, is small relative to the parasitic inductance. Note that this results in a high value for L^* , which degrades the efficiency of an electromagnetic accelerator. It also yields essentially the same coil current profile for every experimental case. As in the experimental data set, lowering the discharge energy only results in a decrease of the peak coil current. In Fig.

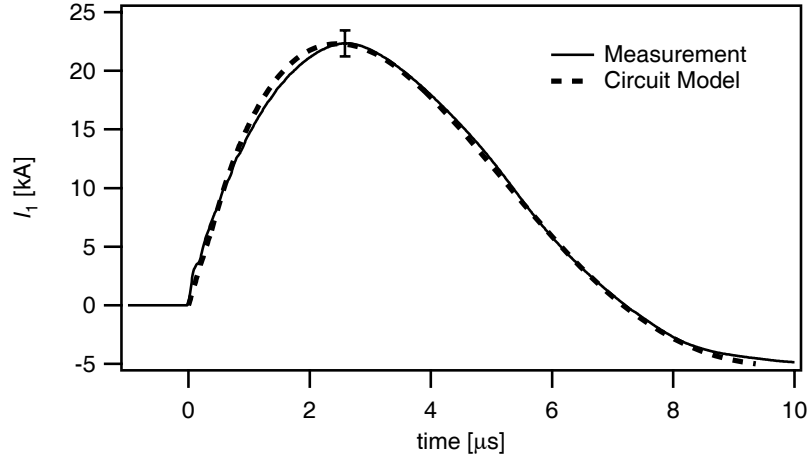


Figure 5.9: Measured (solid line) and predicted (dotted line) coil currents, I_1 , for the baseline case.

5.9, the experimental discharge current for the baseline case is plotted as a solid line, while the dashed line representing our simulated coil current shows excellent agreement.

5.6.2 Acceleration Model Modifications for FARAD Simulations

There are two major assumptions in the acceleration model, which are obviously violated in the FARAD proof-of-concept experiment, and which lead to less efficient electromagnetic acceleration. The first assumption is that the plasma current, I_2 , begins flowing immediately at time $t = 0$. The induced magnetic field data (see Figs. 4.6, 4.7 and 4.8) clearly show that there is a delay between $t = 0$ and the time when current sheet formation occurs. This was primarily inferred from the high magnetic field diffusion rates observed in the induced field measurements just after $t = 0$ and the subsequent “knees” in the same waveforms indicative of current sheet formation. The second violated assumption is that the current sheet forms coincident with the acceleration coil (at the location $z = 0$). There is a glass coverplate of finite thickness positioned over the coil which protects it from the plasma. Fortunately, we can modify the model to more accurately reflect the proof-of-

concept experimental setup.

Using the experimental data found in Figs. 4.6, 4.7 and 4.8, we can estimate when the current sheet forms based upon the temporal location of the “knees” in the magnetic field traces. The delay times, t_{delay} , are plotted in Fig. 5.10 for each experimental case. The model can be modified such that there is no I_2 equation, and consequently no current sheet dynamics or mutual inductance, until $t = t_{\text{delay}}$. Before this time, only the temporal evolution of the coil current, I_1 , is computed. After this time, the entire set of equations is solved with the initial condition $I_1 = I_1(t_{\text{delay}})$.

The glass coverplate thickness is taken into account by altering the initial position of the current sheet, $z(0)$, to match the standoff distance in the FARAD, which is equal to 8.8 mm. However, we previously inferred from experimental data that the current sheet actually forms at a different axial location in each experimental case due to the various preionized plasma distributions associated with those cases. We do not account for this additional offset in the present work.

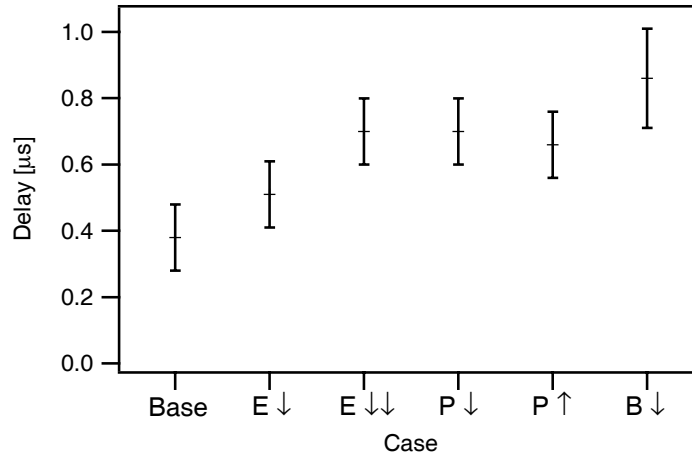


Figure 5.10: Delay times from $t = 0$ before the current sheet forms as determined by from Figs. 4.6, 4.7 and 4.8.

5.6.3 Plasma Current

Plasma current densities, both experimentally measured and estimated based upon the results of the acceleration model, are presented in Fig. 5.11 for each experimental condition. Of all the measured parameters, this is the most difficult one to compare with the results

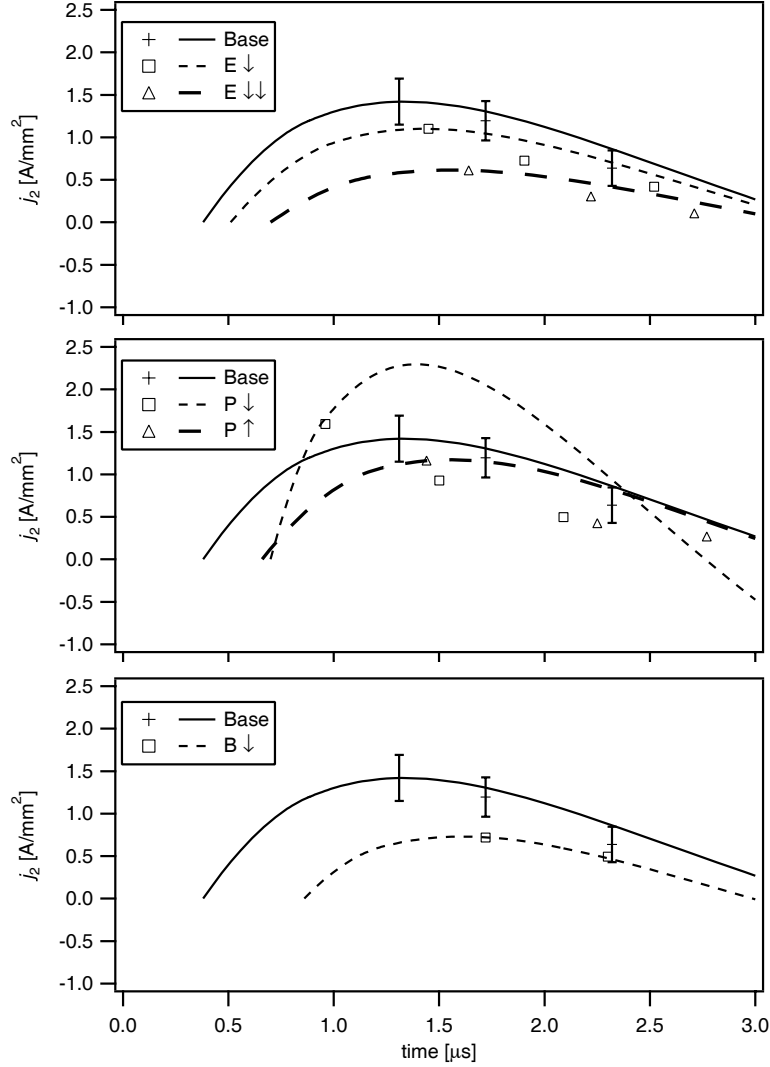


Figure 5.11: Current density measurements in the FARAD (markers) and estimated current densities computed based upon the acceleration model (lines). Current densities estimated by choosing a sheet width, Δz , such that the first data point falls on the curve. Values of Δz for each case are given in Table 5.3.

Table 5.3: Current sheet widths, Δz , used to compute the current density profiles found in Fig. 5.11.

Case	Δz [cm]
Base	7.5
E↓	7.6
E↓↓	9.6
P↓	2.5
P↑	7.3
B↓	7.9

of the model. This is because the measurements yield a measure of current density, j_2 , while the computation yields only a measure of the total plasma current, I_2 . Furthermore, the model assumes that all the current comprising I_2 is located at a single axial position (i.e. zero sheet thickness). In order to make a comparison one must either integrate over the measured current density profile or divide the total computed plasma current by a given current channel width. In Fig. 5.11, the latter technique is employed. The current sheet width, Δz , is chosen such that the first current density point for each data set lies on the line given by the curve $I_2(t)/(\Delta z \Delta r)$, where Δz is the current sheet thickness and Δr is the distance from the inner to the outer edge of the coil. The values of Δz used for each experimental condition are given in Table 5.3. The value of $\Delta r = 70$ mm.

In general, the computed current density time histories agree in form with the measured values of j_2 . Note that this agreement is only possible when the computation of j_2 is delayed by the values given in Fig. 5.10. The exception, which will be discussed in more detail in Sect. 5.6.4, is the noticeably poor agreement in the lower pressure case, P↓. However, Table 5.3 reveals that the current sheet widths used to compute the current densities are much too high to be realistic (especially given that the spatial resolution of our own current sheet measurements is 5 mm). Thus, we see that the model overpredicts the plasma current by roughly an order of magnitude. This reveals that a substantial portion of the magnetic

field induced by the acceleration coil is not directed into the formation or maintenance of the current sheet. This correlates with our experimental magnetic field data (Figs. 4.6, 4.7 and 4.8) in which we observed relatively high induced field strengths beyond the current sheet (i.e. for z greater than the current sheet location) and stated that this was indicative of continuing magnetic field diffusion through the plasma even after the current sheet forms. This experimental observation violates the implicit circuit modeling assumption that the accelerator coil and current sheet perfectly couple through the mutual inductance term. In the model, there is no mechanism which allows the magnetic field to diffuse through the plasma without performing work. Unfortunately, the limited nature of a lumped element circuit model makes it difficult to incorporate this effect into our circuit equations.

5.6.4 Current Sheet Trajectory

Experimentally measured and simulated current sheet trajectories are presented in Fig. 5.12. In all cases, the simulated sheet initial position corresponds to $z = 8.8$ mm (glass coverplate thickness) and the calculation for the sheet position evolution is delayed in time until $t = t_{\text{delay}}$. In general, we observe remarkably good agreement, especially given the major discrepancies between the computed and measured current densities. It is, in fact, extremely surprising that the dynamics of a weakly ionized current sheet could be predicted by a model that essentially assumes a fully ionized sheet. The most likely explanation for the agreement between the calculated and measured sheet trajectories, given the disagreement in j_2 , is as follows.

As previously mentioned, the acceleration modeling implicitly assumes that the current sheet perfectly couples with the coil current through the mutual inductance term. We have already discussed how resistive diffusion of the magnetic field across the plasma in the proof-of-concept experiment serves to invalidate this assumption and leads to measured

current densities which are much lower than calculations predict. The lower measured current density would normally imply slower measured sheet speeds relative to the model's predictions. However, the model also assumes that the current sheet entrains and accelerates all the mass it encounters (perfect snowplow). In the previous chapter we showed that the current sheet in the proof-of-concept experiment is porous, only entraining a fraction of

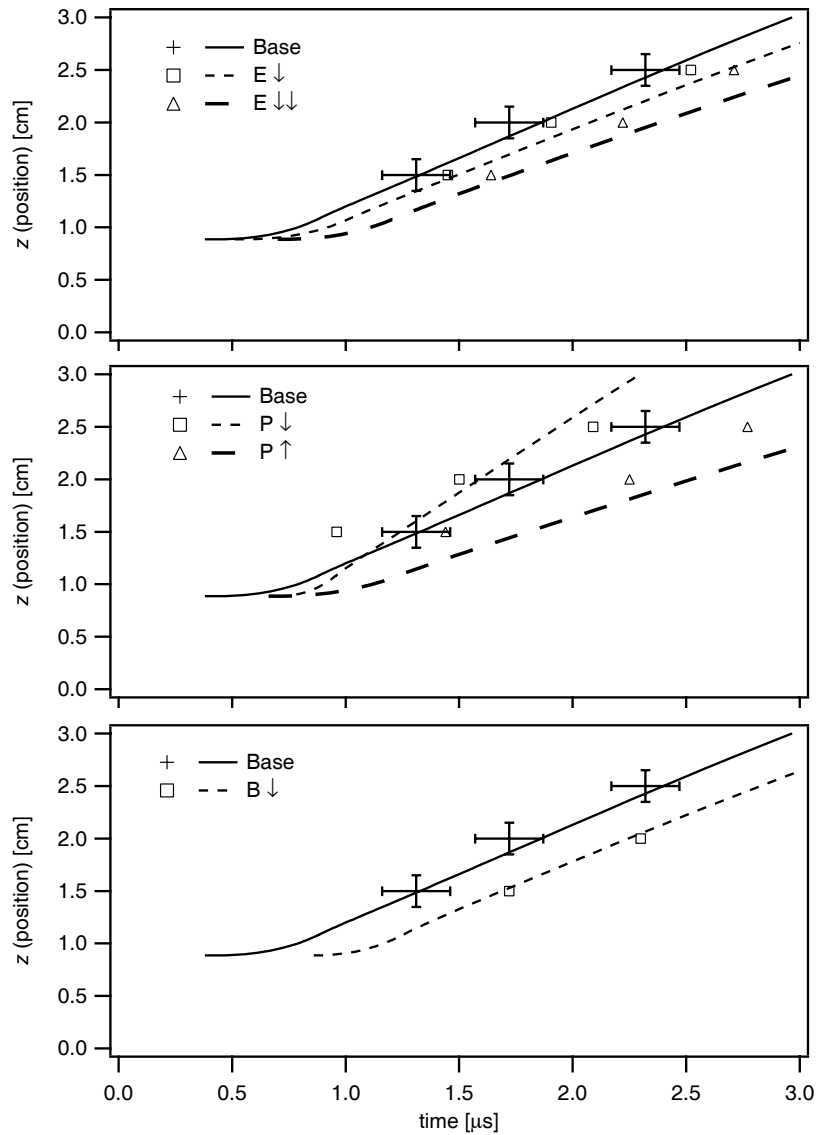


Figure 5.12: Current sheet trajectories in the FARAD as measured (markers) and computed predicted using the acceleration model (lines).

the total mass it encounters and reducing the drag felt by the sheet to levels far below those predicted by the model. It may be that these two effects (porosity of the sheet to encountered propellant and induced magnetic field) are related and proportional to each other and could, in effect, cancel each other. While we do not definitively prove this to be the case, it does explain the agreement we observe in the trajectories plotted in Fig. 5.12.

The P_{\downarrow} experimental data exhibit the worst agreement with the model, deviating significantly in both the computed current density and the sheet trajectory. We know from the experimental data presented in the previous chapter that the sheet forms further downstream in this case and the data in Fig. 5.12 corroborate this conclusion. The data also cause us to suspect that the sheet is much weaker in this case than in the baseline case because it forms further away. It seems reasonable to expect that if the actual initial sheet position were known and could be used in the model, then the agreement with the experimental data would improve.

5.7 Summary of Findings

Below, we summarize the major finding of this chapter. These are broken into two categories. The first represent general insights and conclusions which arise from the nondimensional modeling while the second are the additional insights obtained through a comparison of the experimental data with results generated using the acceleration model.

Observations from the nondimensional modeling

- There exists a value of the dynamic impedance parameter, α for which thrust efficiency is maximized. This value is between 1 and 2 for a slug mass loading and 2 and 3 for the uniform fill. The optimum corresponds to a matching of the driving circuit's natural oscillation timescale to the residence timescale of the current sheet

in the acceleration zone.

- Efficiency increases for decreasing values of the inductance ratio, L^* , as this represents an increase in the fraction of energy which can be deposited into electromagnetic acceleration of the propellant.
- Efficiency and exhaust velocity increase when both ψ_1 and ψ_2 (or equivalently Ψ) are decreased in value. This implies that underdamped circuits are preferable for increased performance in pulsed inductive accelerators.
- Performance increases as a greater fraction of the propellant is loaded close to the back-end of the accelerator and is maximized for a slug mass loading.
- The addition of a static magnetic field does not have an effect on accelerator performance as long as it is much weaker than the induced magnetic field, which was the case in our POCX.

Insights from comparing modeling results with experimental data

- The axial location at which the current sheet forms is a function of the background pressure.
- Larger delays in current sheet formation have an adverse effect on current sheet formation and lead to lower peak current densities.
- The model significantly overestimates current density in the POCX current sheet, implying non-ideal electromagnetic coupling between the acceleration coil and the sheet.
- The current sheet in the POCX is not entraining all the propellant it encounters. General agreement between the simulated and measured current sheet trajectories

leads us to conclude that the sheet's porosity to propellant and permeability to the induced magnetic field are proportional.

Chapter 6

Conclusion

In this work we have presented the FARAD, a new pulsed inductive acceleration scheme which employs an RF-discharge stage to preionize the propellant. While the acceleration mechanism employed by the FARAD is the same as that found in other concepts like the PIT, one of its novelties lies in its ability to produce an inductive current sheet at much lower capacitor voltages and initial discharge energies due to the presence of the preionized plasma. This reduces one of the primary constraints placed upon the design of a pulsed inductive plasma accelerator, namely that the current pulse in the acceleration coil must both completely ionize and accelerate the propellant. An additional conceptual difference is that in the FARAD the propellant is fed as a plasma from upstream of the acceleration stage instead of as a neutral gas fed from downstream by a sizeable nozzle.

The research presented in this dissertation consisted of two major branches. The first sought to demonstrate, through a proof-of-concept experiment, that using a separate preionization mechanism allows for the formation of an inductive current sheet at much lower discharge energies and voltages than those used in the PIT, even though our experiment was not optimized for inductive current sheet formation and acceleration. Parametric variation of the controllable parameters in the system yielded insight into the physics of inductive

current sheet formation and acceleration in the presence of a preionized plasma. As an aside, the data leading to our conclusions concerning the effects of background pressure and the applied field on the preionized plasma distribution and initial current sheet location were subtle. It is quite likely that if the POCX formed a more highly ionized current sheet, as is desired in a real thruster, this effect would have been missed altogether. However, there appears to be no physical reason the insights gained from the POCX would not hold for a more highly ionized current sheet and, in fact, many of our observations will be used in this chapter to put us on the path towards a more efficient accelerator.

The second branch of this dissertation consisted of the nondimensionalization of a one-dimensional acceleration model for the purposes of revealing the relevant acceleration scaling parameters and providing additional insight into the acceleration process. The model was used to explore the dimensionless parameter space to determine how varying the values of the different scaling parameters affected the performance of a pulsed inductive accelerator. In addition, we applied the model to our proof-of-concept data to gain additional understanding of the experimental observations.

The conclusions and insights obtained through the experimental study and the acceleration modeling were summarized at the ends of Chapters 4 and 5, respectively. In this chapter, we distill the results of this dissertation into a set of rules for the design of an optimized FARAD thruster and then conclude by proposing future research directions.

6.1 FARAD Design and Optimization Ruleset

In this section, we state a set of rules and guidelines which can be directly applied to the design of a FARAD thruster[49]. These rules are based upon existing empirical prescriptions as well as the insight resulting from the experimental, theoretical and numerical investigations contained within this dissertation. Some of the rules apply to pulsed inductive

accelerators in general, while others are specific to the FARAD concept and geometry. The subsections are organized along the lines of the physical processes present in a FARAD thruster:

1. Plasma acceleration,
2. Current sheet formation,
3. Applied magnetic field generation,
4. Mass injection and preionization.

In each subsection, a set of rules governing the optimization of the design will be outlined. Qualitatively, the rules fall roughly into one of three separate categories, depending upon the level of confidence and theoretical or experimental understanding of the physical processes.

- **Category A:** Rules which are directly derived from combining actual experimental results and first principles.
- **Category B:** Rules for which no direct experimental confirmation exists but can be supported by results of theoretical modeling.
- **Category C:** Rules which are speculative, or for which only inconclusive or ancillary evidence exists.

The rules pertaining to each particular physical process are summarized and categorized according to these definitions at the end of their respective subsections.

6.1.1 Plasma Acceleration

The rules governing plasma acceleration optimization are listed below and follow directly from the dimensionless acceleration model studies found in the previous chapter. For the sake of brevity, we simply collect all of the valuable insights gained throughout the course of the previous discussions into one location for quick reference.

- The dynamic impedance parameter α should be used to adjust the specific impulse, I_{sp} , and the impulse bit to the desired levels. **(Category A)**
- The Lovberg criterion[47], $\Delta L/L_0 = L^{*-1} > 1$ must be met for efficient electromagnetic acceleration. **(Category A)**
- The thickness of the propellant layer over the acceleration coil face should be much less than the characteristic electromagnetic coupling distance z_0 to increase the efficiency. Efficiency is maximized for a slug mass loading. **(Category A)**
- If the capacitor can handle higher levels of voltage ringing, the circuit parameters should be optimized such that the circuit is underdamped [$\Psi \equiv (\psi_1 + \psi_2)/2 < 1$] for greater thrust efficiency. **(Category B)**
- Exploration of the nondimensional parameter space for typical conditions has indicated that the thrust efficiency tends to be highest in the vicinity of $\alpha \approx 2$. **(Category B)**

6.1.2 Current Sheet Formation

The most important assumption in the acceleration model discussed in the previous chapter is that current sheet formation is both immediate (at $t = 0$) and complete (does not allow the induced magnetic field to diffuse through it). This condition has proved most difficult to

achieve experimentally. Unfortunately, when current sheet formation is delayed, data (both in this dissertation and in the literature[4]) show that a significant amount of the magnetic field energy radiates away from the acceleration coil and escapes without performing any useful acceleration.

Current sheet formation occurs more quickly as the accelerator coil current rise rate, dI/dt , is increased[4]. The increasing rise rate leads to the formation of a current sheet that more effectively contains the magnetic pressure radiating from the acceleration coil, leading to a more efficient acceleration process

For a given coil geometry, the simplest way to increase the current rise rate is to increase the ratio of the initial voltage to the initial (parasitic) inductance because the initial current rise rate scales like

$$\frac{dI}{dt} \propto \frac{V_0}{L_0}.$$

However, we are interested in a general rule that can be applied to a coil of arbitrary size. For this, we need to look not at the total current rise rate in the coil, but the linear current density rise rate. If we assume that the linear current density in the coil, j_θ , is radially uniform over the coil face, then for a given coil dimension, \mathcal{L} (see Fig. 6.1), the current density rise rate scales as

$$\frac{dj_\theta}{dt} \propto \frac{V_0}{L_0 \mathcal{L}}.$$

In the PIT, the value of $V_0/(L_0 \mathcal{L})$ is approximately equal to 1.5×10^{12} A/(m s). At this value, the current sheet in the PIT forms with little or no delay and is relatively impermeable to the induced magnetic field. The corresponding maximum value of $V_0/(L_0 \mathcal{L})$ found in the FARAD POCX was 2.6×10^{11} A/(m s). At this current density rise rate, a current sheet formed in the FARAD, but it did not form very quickly and the experimental data show that it was still somewhat porous to both the propellant it encountered and the magnetic field induced by the acceleration coil. This indicates that the rise rate should be further

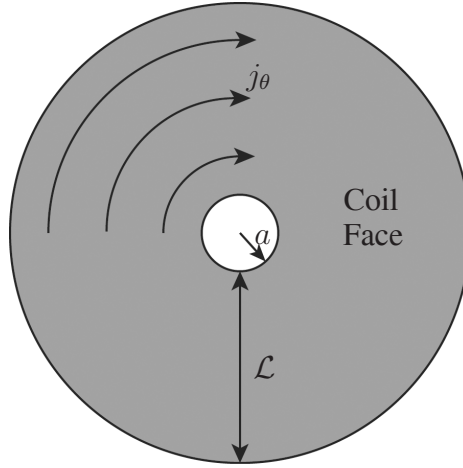


Figure 6.1: Schematic of a pulsed inductive accelerator coil face.

increased in future FARAD designs to levels closer to those found in the PIT to promote faster current sheet formation.

The rules governing current sheet formation in the FARAD are summarized as follows.

- Increasing the current rise rate in the coil leads to faster current sheet formation. For a given geometry, this is accomplished by increasing the ratio V_0/L_0 . (**Category A**)
- The linear current density rise rate in the coil, which scales like $V_0/(L_0 \mathcal{L})$, should have a value approaching 10^{12} A/(m s). (**Category C**)

6.1.3 Applied Magnetic Field Generation

Optimization of the applied magnetic field is difficult because it is intimately connected to many of the physical processes in the FARAD, each having its own requirements. The applied field is necessary to generate a helicon plasma. It is also used to guide charged particles from the helicon source to the acceleration stage. Finally, it must not impede current sheet formation and must allow for plasma detachment at the end of the acceleration coil pulse. In the present section, we discuss how each of these processes impacts the field optimization problem.

Helicon Source

To support the helicon discharge mode, the field must be in the axial direction. We need not delve too deeply into the magnetic field scaling issues associated with the helicon discharge as they are beyond the scope of this dissertation and are, in fact, the subject of much research (see Refs. [4,5] and the references within). We should note, however, that helicon discharges at low pressures ($p < 5$ mTorr) have been sustained in a 50 G applied field while discharges at higher pressures ($p > 10$ mTorr) typically require field strengths on the order of several hundred gauss[50].

Turning the Plasma

One of the challenges inherent in the FARAD concept is transporting the propellant from the helicon source to the acceleration coil face. We envisioned that this difficulty could be overcome by exploiting the plasma's natural tendency to follow field lines, and employing an appropriately tailored magnetic field topology. This is accomplished by creating an axial field in the helicon source that transitioned to a radial field and then passed over the face of the acceleration coil.

As we saw in the POCX, ambipolar diffusion keeps the motion of the electrons and ions emerging from the helicon source coupled. Consequently, we need only worry about keeping the electrons magnetized to turn them using the applied magnetic field. To accomplish this, the electron cyclotron radius, r_{ce} , should be smaller than the characteristic device length scales at every location in the system. In FARAD, the relevant length scales are: A) the helicon source radius, R_H , B) the acceleration stage propellant depth, δ_m , and C) the radius of curvature of the transition between the two stages, R_c (see Fig. 6.2). To minimize the effects of collisions on the electrons, we should also attempt to fulfill the condition

$$\Omega_e = \frac{\omega_{ce}}{\nu_e} > 1.$$

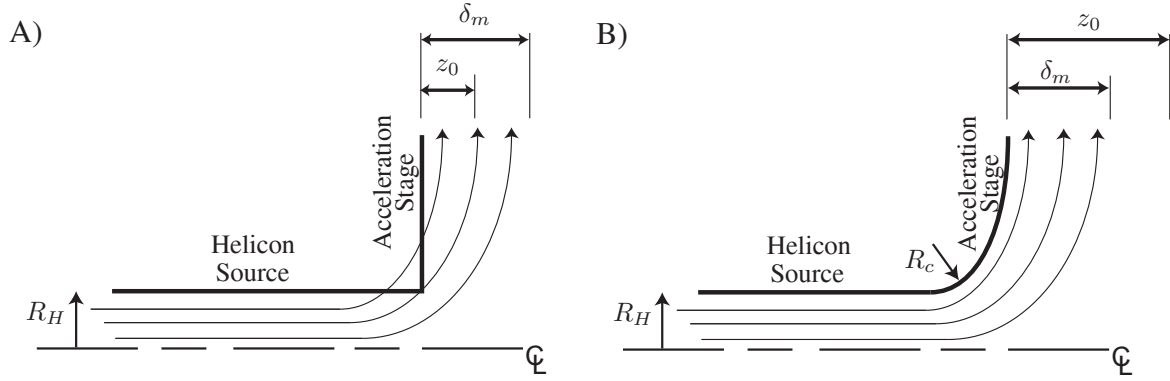


Figure 6.2: A) Schematic of the magnetic field topology in the FARAD POCX. B) Optimized thruster geometry/magnetic field topology

Two issues arose in the POCX which impeded the efficient transfer of plasma from the helicon source to the acceleration coil face, both of which are illustrated schematically in Fig. 6.2A. The first was that many of the magnetic field lines intersected with the sidewalls of the containment vessel. This resulted in a reduction of the number of electrons turned towards the coil face and led to a decrease of the preionized plasma density in the acceleration stage. The second problem was that the preionized plasma translated in the axial direction as it was moving radially over the acceleration coil, distributing itself over a wide volume of thickness δ_m in the acceleration stage. The acceleration modeling showed that preionized plasma distributed outside the acceleration region (having length z_0) does not couple with the acceleration coil and is essentially wasted.

A more optimized design which seeks to address the problems listed above is presented in Fig. 6.2B. In this design, the transition between the helicon source and the acceleration stage is contoured so that the sidewalls do not intersect with the magnetic field lines. In addition, we assume that the acceleration coil can be redesigned to increase the length of the electromagnetic coupling region to the point where $z_0 \geq \delta_m$, thus ensuring all the propellant in the acceleration region receives at least 'some' acceleration.

As an aside, even if the conditions listed above are fulfilled, the axial field lines located near the centerline of the helicon stage may prove quite difficult to turn. These field lines represent a weaker magnetic field strength and their tendency is to travel well beyond the acceleration stage before gradually sweeping around and reconnecting back on themselves. These factors make it particularly difficult to turn the plasma located on the centerline towards the face of the acceleration coil and represent significant challenges which must be addressed in a real thruster design.

Sheet Formation and Detachment

As a general rule, the applied field in the acceleration region must not impede the formation of the current sheet and should not affect the acceleration process. In the previous chapter, acceleration modeling resulted in the identification of a dimensionless parameter, γ , which could be recast to contain the apparent ‘inductance’ presented to the circuit by the applied magnetic field. Calculations revealed that the applied field does not have an effect on the acceleration process except in the region of parameter space where $\alpha < 1$ and $\gamma > \mathcal{O}(0.01)$. Essentially, this corresponds to operation in a regime where the applied magnetic field strength approaches that of the induced field. It can also be thought of as a regime where the inductance presented to the circuit by the applied field approaches the acceleration coil’s inductance. This implies that the accelerator should operate in the regime where $\gamma < 0.01$ so that the applied field does not affect the motion of the current sheet. This is equivalent to stating that the applied and induced magnetic field strengths should fulfill the inequality

$$B_{r \text{ Applied}} \ll B_{r \text{ Induced}}.$$

We know from the discussion on current sheet formation that added inductance in the circuit slows the current sheet formation process and that this can lead to acceleration inefficiencies. We can assume that the applied field inductance affects the acceleration and

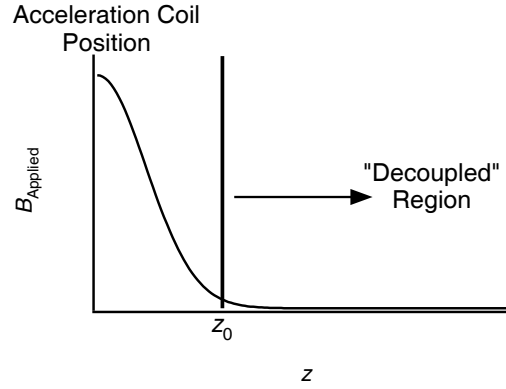


Figure 6.3: Conceptual sketch showing the desired applied field strength as a function of position that will allow for plasma detachment.

current sheet formation processes equally (which is likely a good assumption since both processes are linear functions of inductance). Consequently, to maintain the current rise rate in the circuit, the applied field parameter should not exceed the threshold of $\gamma = 0.01$.

In an efficient accelerator, the current sheet should detach from the applied magnetic field and continue propagating away from the acceleration coil after the current pulse terminates. This will occur if by the end of the pulse the plasma reaches a region of space where the value of the applied magnetic field is small (≈ 0). This implies that the applied field in the acceleration region must possess a maximum value at the coil face and quickly decrease in magnitude as one moves away in the axial direction. The length scale over which this decrease should occur is the characteristic electromagnetic coupling distance, z_0 . This condition can be stated succinctly through the inequality

$$\frac{B_{r \text{ Applied}}}{|\nabla B_{r \text{ Applied}}|} \ll z_0,$$

where the gradient is evaluated in the z -direction. A conceptual graph showing the field strength plotted as a function of position is presented in Fig. 6.3.

Summary of Design Rules for the Applied Field

We can compile the following design rules for the magnetic field to support a helicon discharge, turn the plasma effectively, and allow the current sheet to escape from the applied magnetic field once the acceleration coil is pulsed.

- To ensure that the preionized plasma is effectively turned by the applied magnetic field into the acceleration stage, the conditions $r_{ce} < R_H$, R_c , δ_m and $\Omega_e > 1$ should be satisfied everywhere in the device. **(Category A)**
- Thrust efficiency is increased when the current sheet forms very close to the acceleration coil face. Therefore, the depth of the magnetic flux tubes passing over the acceleration coil face (which governs the electron layer depth and sheet initiation location) should be less than the characteristic electromagnetic coupling distance, $d < z_0$, and spatially located close to the coil's face. **(Category A)**
- To reduce plasma losses at the wall of the helicon source, the field topology and the walls of the device should be contoured in such a way that they do not intersect. **(Category A)**
- The applied axial field in the helicon section must be of sufficient strength, $\mathcal{O}(100)$ G, to support the helicon discharge mode. **(Category B)**
- To allow the plasma to effectively cross the applied magnetic field lines, the applied magnetic field strength and the peak induced magnetic field strength should satisfy the criteria $B_{r \text{ Applied}} \ll B_{r \text{ Induced}}$. **(Category B)**
- To allow for plasma ‘detachment’ once the acceleration pulse is complete, the applied field in the acceleration region should conform to the condition $B_{r \text{ Applied}}/|\nabla B_{r \text{ Applied}}| \ll z_0$. **(Category B)**

- To reduce the chance that the field will adversely affect the current sheet formation and acceleration processes, the maximum applied field strength in the acceleration stage should be such that the condition $\gamma < 0.01$ is fulfilled. **(Category C)**

6.1.4 Mass Injection and Preionization

There are three major pulsed systems in the FARAD (aside from the applied B -field coils, which may be pulsed in a real thruster). These are the gas valve, which introduces the initial propellant pulse into the thruster, the helicon source, which preionizes the gas, and the acceleration coil. The pulse length for each system and the intra-pulse sequencing are important from the point of view of mass utilization efficiency and, potentially, total power consumption.

The timing of the different pulsed systems is, in general, difficult to handle analytically. The thruster's dimensions and the prevailing state of the propellant (e.g. density, temperature) could greatly affect the timing. The propellant valve and helicon source have finite response times which must be accounted for when determining the actual switch-on and switch-off times. Also, the convection speed of the propellant through the thruster may change, especially if it is appreciably heated in the helicon source. An additional complication arises if we were to consider that while the propellant pulse is convecting towards the acceleration stage, it is also expanding through thermal diffusion. Finally, if the ions are magnetized, the changing magnetic field strength, which decreases as the field expands radially in the acceleration stage, may greatly affect the speed at which the ions expand over the acceleration stage face. The ions would experience an increase in velocity parallel to the magnetic field due to conservation of the first adiabatic invariant, μ , defined as

$$\mu = \frac{mv_{\perp}^2}{2B},$$

where v_{\perp} is the velocity of an ion in the direction perpendicular to the applied magnetic

field.

We should mention that all the neutrals emerging from the helicon source must somehow be turned so that they propagate radially along the face of the acceleration coil. This could be accomplished, as in the PIT, using some sort of physical nozzle or duct. However, we must keep in mind that the nozzle's location in the plasma stream subjects it to constant bombardment and potential erosion, which is one of the PIT drawbacks that the FARAD design specifically seeks to avoid. While this technique would turn the flow, the object may become a source of impurities or, even worse, be the life-limiting component in the system.

Considering the difficulty of arriving at an analytical prescription for optimizing the timing scheme for FARAD, the timing is perhaps best optimized experimentally using fast diagnostics (fast-response pressure gauges and/or Langmuir probes) located throughout the apparatus to monitor the spatial and temporal extent of the gas pulse.

We proceed with a general set of design rules which seek to guide the optimization of the intra-pulse sequencing.

- The neutral gas pulse, of temporal extent Δt_g , precedes the other pulses. The pulse length should be such that when the propellant layer reaches the acceleration stage, it completely fills the region between the inner and outer coil radii. The amount of additional propellant remaining outside that region constitutes a mass utilization inefficiency since it will not be accelerated when the acceleration circuit is pulsed.

(Category B)

- The RF pulse length, Δt_{RF} , is the duration that power is supplied to the helicon stage. The RF pulse should not begin until the injected gas has filled the helicon stage. The pulse must remain active long enough to fill the entire acceleration stage with the preionized plasma but be deactivated before producing any extraneous plasma that may not reach the acceleration coil before it is pulsed. **(Category B)**

- The acceleration coil pulse, Δt_a , must not start until most of the preionized plasma has been guided to the back-end of the acceleration stage and completely fills the region between the inner and outer coil radii but it must begin before any significant portion of the leading edge of the preionized plasma begins escaping at the outer edge of the coil. **(Category B)**
- The thruster mass injection system should be spatially compact. This will not only reduce system mass, but it will allow for a more repeatable mass injection and pulsing scheme by reducing the effects of longer timescale processes, such as thermal diffusion or recombination. The compact construction should lead to an overlap of the neutral gas and RF pulses. **(Category C)**

Before leaving this process, we should mention a few additional techniques which may benefit a real thruster design. The demand for a fast gas valve can be alleviated by employing a burst-pulse scheme developed for gas-fed pulsed plasma thrusters[51, 52]. In this mode, a “slow” and sturdy valve is operated at a low duty cycle and the thruster is operated in a burst of discharge pulses. If the response time of the RF-matching network is too slow to switch the preionization pulse on and off for each individual acceleration pulse, it too can operate at the lower duty cycle associated with the “slow” valve. The time between each consecutive *pulse* is equal to the time it takes the current sheet to sweep the gas through the thruster and then refill the acceleration region while the time between the *bursts* is dictated by the available steady-state power and the required (average) thrust. This technique would increase not only the mass utilization efficiency, but would also extend the lifetime of the system through the use of a lower repetition rate valve.

6.1.5 Summary

We have presented a set of design rules and guidelines aimed at producing an efficient, high-performance thruster based upon the FARAD concept. The preceding discussion was organized along the lines of the various physical processes present in the accelerator, with rules pertaining to a particular process collected in a series of statements at the end of the respective subsection. The rules are based on a combination of experimental results, analytical and numerical modeling, and physical intuition, and we have assigned a qualitative measure of the level of confidence in each specific rule based upon the method of justification employed. A cursory examination of the various rules presented in each subsection show that some of the rules complement each other. Further experimental and theoretical studies would undoubtedly lead to a refinement of these rules.

6.2 FARAD Research Directions

There are certainly many issues pertaining to the FARAD specifically and pulsed inductive thrusters in general that deserve closer inspection and future research. In order to actually design and build a FARAD thruster, however, the rules presented in this chapter need to be experimentally validated. Work along this path should focus mostly on the category B and C rules since they are not as well tested. While the rules presented in this chapter form a basis to begin such a study, further experimental and theoretical studies would undoubtedly lead to a refinement of these rules and potentially allow for the formulation of additional rules not presented in this dissertation.

One of the next major steps in the development of an actual FARAD thruster is the construction of a version optimized using the rules stated above for the purpose of obtaining performance data using a thrust stand. Such a thruster may resemble the conceptual ren-

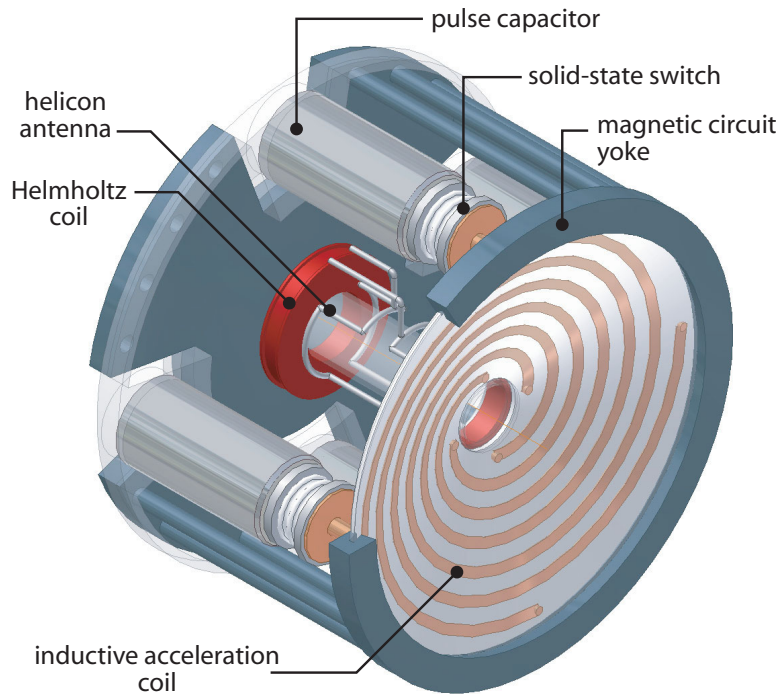


Figure 6.4: Conceptual rendering of a FARAD thruster (note: one section removed to reveal inner detail).

dering presented in Fig. 6.4. This research path would demonstrate the capabilities of the concept and advance its level of readiness to the point where we can begin its development for use on spaceflight missions. It would also present the opportunity to explore some of the design rules developed in the previous section. Specifically, the applied magnetic field and gas injection rules had to, for the most part, be developed using physical intuition and a first principles understanding of basic gas dynamics and plasma physics. Unfortunately, it is difficult to imagine a simple experiment to test these design rules since the field topology and propellant distribution in one region of the thruster are interconnected with the topologies and distributions in other regions. We recommend that a full thruster prototype be developed for experiments whose purposes would be to generate meaningful performance data to benchmark the concept and to investigate the interrelated physical processes and phenomena that can only be studied in the full thruster environment.

Aside from the more fundamental research outlined above, there are many interesting component-related issues which remain to be addressed. For example, the switches in pulsed inductive thrusters must be capable of holding off $\mathcal{O}(1000 \text{ V})$ while switching at least $\mathcal{O}(10 \text{ kA})$ of current and at the same time possessing an $\mathcal{O}(10 \text{ ns})$ response time. Moreover, they must be extremely long-lived to last for approximately 10^9 - 10^{10} pulses in order to allow for the delivery of an appreciable total impulse. Another issue pertains to the insulating material separating the acceleration coil from the plasma. This shield must be a dielectric to allow the induced field to pass through and interact with the propellant. The dielectric must not erode or fail in some way that allows the plasma to directly contact the inductive coil. However, it must also be very thin so that the plasma can initiate very close to the inductive coil for the purpose of maximizing efficiency. Tailoring the geometric shape of the thruster and the associated insulator materials introduces further complexities into the problem. In addition, ablation of the dielectric, which should be driven by radiative heat transfer, should be proportional to the energy per pulse. A dielectric that does not ablate, even at high temperature can be employed, if it exists. If such a material does not exist, we would need to design our accelerator to operate at relatively low discharge energies to minimize the heating. A thruster operating at $\mathcal{O}(100) \text{ J/pulse}$ may fulfill the requirement, and higher power operation may still be possible at a high duty cycle (10-100 Hz). However, too much energy may still be transferred to the dielectric in this case, which could prove to be a “show-stopper” for both high energy per pulse and high average power operation.

In summary, the FARAD concept requires significant additional development before it is ready for application to missions. The research presented in this dissertation serves as the starting point for future development, and we have suggested several paths which should advance the concept beyond its present state. It is suggested that refinement of

the design rules and construction of an actual thruster model should proceed in parallel with component-related development. As more advanced components become available, they can be incorporated into a FARAD thruster design. However, the present lack of components which are suitable for a space-qualified thruster should not preclude the pursuit of refinements on other research fronts.

Appendix A

Literature Review

In this appendix we review different concepts that could be used to inductively accelerate plasma and provide thrust for a spacecraft. Devices of this type generally fall into one of two classes. In one class a current sheet is formed which then directly accelerates the propellant to generate thrust. In the other class plasma structures known as plasmoids are formed and subsequently accelerated using external magnetic fields. We focus our review primarily on the Pulsed Inductive Thruster (PIT) which falls into the same class of inductive accelerators as FARAD (those employing current sheets) and, historically speaking, represents a majority of the research related to pulsed inductive thrust production. For completeness, we shall briefly describe other pulsed inductive accelerator concepts at the end of this appendix. The goal of this review is to describe the current state-of-the-art for inductive acceleration, compile a list of lessons learned from past experiments, and identify the remaining research problems.

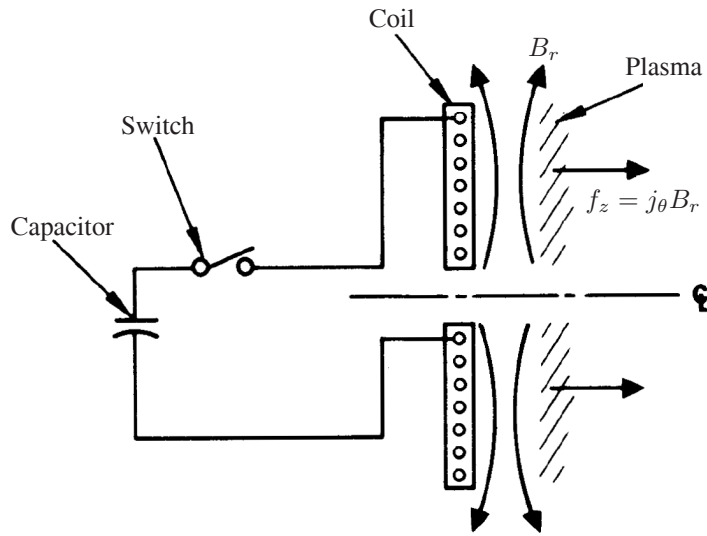


Figure A.1: Schematic showing the basic operation of a planar pulsed inductive plasma accelerator (after Ref. [40]).

A.1 The Pulsed Inductive Thruster (PIT)

The Pulsed Inductive Thruster (PIT) is a pulsed inductive plasma accelerator with a planar coil geometry. It essentially operates in the manner illustrated in Fig. A.1. The capacitor bank is charged to high voltage and propellant is injected over the face of the acceleration coil. The capacitor is discharged through the acceleration coil using a triggered spark gap. Current flowing in the coil first inductively ionizes the gas, forming a current sheet, and then couples with it to inductively accelerate the current sheet in the axial direction away from the face of the coil, thus generating thrust.

The development of the PIT has been primarily directed by C.L. Dailey and R.H. Lovberg with the work occurring at TRW Space Systems in Redondo Beach, CA (later acquired by Northrop-Grumman). The overarching theme of this work has been to develop an inductive thruster with high efficiency. Historically, the research effort can be broken down into three distinct phases. Research efforts during the first period (1965-1973) were aimed at understanding the structure of an inductive current sheet and evaluating differ-

ent concepts for propellant injection and preionization. In the second period (1979-1988), the focus shifted more towards developing a true propulsion system and increasing the performance of the base design through incremental design changes. The present period (1991-present) began with the introduction of a new PIT thruster base design, which, from a development standpoint, represents the state-of-the art in pulsed inductive plasma acceleration. While this base design has remained essentially fixed, many of the components and subsystems have been (and are presently being) reengineered for the purposes of increased lifetime and performance. We present the history and development of the PIT organized according to the research phases outlined above.

A.1.1 Early Research & Development: 1965-1973

Inductive Current Sheet Structure

Early research was directed towards understanding the basic microstructure of the current sheet in the planar inductive accelerator geometry. Specifically, the aim of the research was to determine the contribution of ion current to the total j_θ induced in the sheet[11, 53]. If the ion current contribution was sufficiently large, it would indicate the presence of appreciable plasma momentum in the azimuthal direction. This was an important research topic for a couple of reasons. First, it was not known whether the accelerated plasma was rotating. Second, it was unknown if the axial ion acceleration was due only to the polarization field (E_z) formed between the electrons and ions or a combination of that and a direct Lorentz body force ($j_\theta B_r$) on the ions. Finally, if energy was going into the azimuthal motion of ions, was it being recovered at some point downstream as axially-directed kinetic energy?

The approach used to answer these questions was similar to that employed by Lovberg when characterizing the microstructure of current sheets in PPTs and theta-pinch devices[54].

In that approach, the generalized Ohm's law

$$\mathbf{E} + \mathbf{u} \times \mathbf{B} - \frac{1}{n_e e} (\mathbf{j} \times \mathbf{B} - \nabla p_e) - \eta \mathbf{j} = 0,$$

is simplified by assuming that \mathbf{u} is equal to the ion velocity and that the contribution of ion current to \mathbf{j} is negligible. Under these assumptions, Ohm's law can be rewritten as a set of scalar equations in which the axial and azimuthal ion velocities are expressed in terms of the (measurable) vector components E_z , E_θ , B_r , j_θ and the axial plasma pressure gradient $\partial p_e / \partial z$. This technique allows not only for the determination of the plasma momentum in both the axial and azimuthal directions, but also a temporal and spatial breakdown of the relative contributions of each potential acceleration mechanism to the total momentum.

The results of the study[11] are summarized as follows. It was found that the axial electric field alone was sufficient to accelerate the ions to the observed sheet speed. This field was due to a combination of a) the charge separation (polarization field) between the accelerating electrons carrying the current, j_θ , and the ions, and b) the large negative electron pressure gradient at the leading front of the sheet which served to enhance the axial electric field. There is very little additional acceleration on the trailing side of the current sheet where the $j_\theta B_r$ force is mostly balanced by the positive electron pressure gradient and serves only to maintain the sheet's cohesiveness. The force exerted on the ions by the induced, azimuthal electric field, E_θ , was balanced by the resistive drag of the current carrying electrons. Consequently, it was deduced that the ions do not acquire momentum in the azimuthal direction and do not carry any current.

We should note here that an earlier study[53], which was superseded by the results given above, concluded that ions did carry a substantial portion of the current. In that study Stark broadening was used to measure n_e and the measurements appeared to indicate that the number density gradient (and consequently the electron pressure gradient) was less significant than in the later study where a laser light scattering technique was used. The

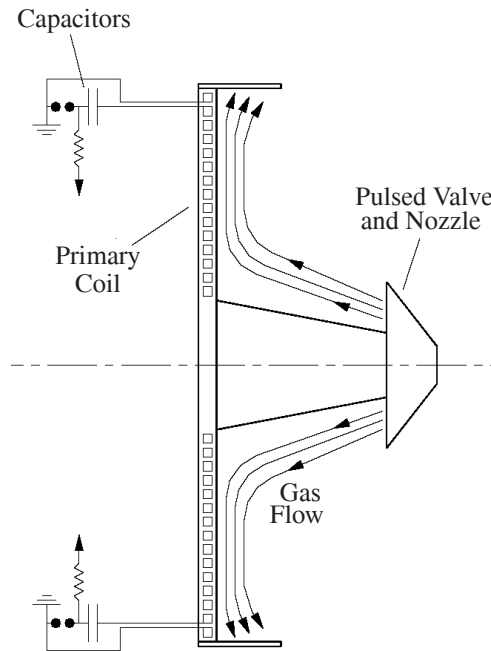


Figure A.2: Schematic showing a typical propellant injection scheme employed on pulsed inductive thrusters (after Ref. [1]).

authors discarded the results of the earlier study by noting that the assumptions made when analyzing the Stark broadening data[55] were violated in the inductive accelerator current sheet.

Proof-of-Concept Studies

Concurrent with their current sheet physics investigations, the TRW group initiated exploratory research in an attempt to develop a prototype pulsed inductive thruster and quantify its performance. The aim of this work was to study the effects of different propellant loading schemes on accelerator performance. Accelerator diameters of 20 cm[12] and 30 cm[13] were tested. In some cases, the propellant was injected onto the coil in the manner schematically illustrated in Fig. A.2. In other cases, an ambient propellant fill was employed.

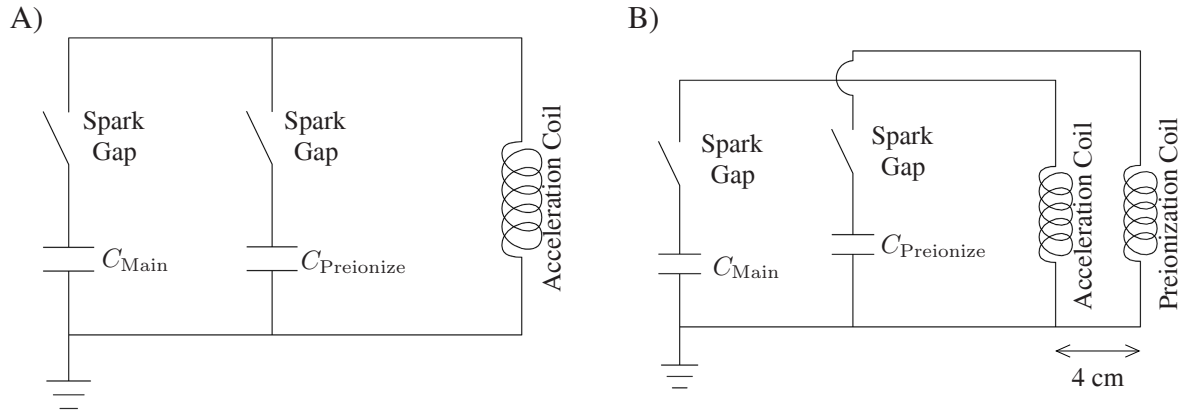


Figure A.3: Circuit schematics for an inductive accelerator pulsed preionization scheme where a second capacitor's is discharged A) through the main acceleration coil and B) through a second coil located axially downstream from the acceleration coil (after Ref. [12]).

Additional studies on the effects of propellant preionization were performed on the same 20 and 30 cm diameter accelerators. The technique used to preionize the gas, illustrated schematically in Fig. A.3, involved switching a smaller, lower energy capacitor across an inductive coil, which served to partially break down the gas. The purpose of this initial pulse was to increase the conductivity making it easier for the second, main current pulse to completely break down the gas and induce a current sheet. In Fig. A.3A, the preionization and main discharge pulses are both conducted through the same coil while in Fig. A.3B, the preionization pulse is conducted through a separate coil suspended in space 4 cm downstream from the primary acceleration coil.

The results of tests performed using the 20 and 30 cm accelerators are summarized in Table A.1. The total impulse of the 20 cm accelerator was measured using a thrust balance while the impulse of the 30 cm accelerator was calculated from field measurements.

When preionization was not employed, performance was higher with ambient gas fill than with the pulsed gas injection. Calculations of the total force as a function of time indicated that the force rose much more rapidly and to a much greater peak value in the

static fill case than in the case where pulsed injection was used. In addition, when the pulsed-injection gas density distribution was peaked near the outer radius, the force on the propellant rose much more slowly than in the case of uniform density pulsed injection; though the force eventually peaked at roughly the same value in both cases. The results of the study indicated that, in the pulsed gas injection case, the current sheet was not sweeping up the propellant it encountered but instead was acting as a permeable surface allowing propellant to slip through as it propagated. Consequently, the sheet moved away from the coil faster (encountering less drag), decoupled faster (yielding a lower peak current density) and produced less total impulse than in the ambient-fill case.

The data in Table A.1 also indicate that higher efficiencies and I_{sp} levels were realized when the propellant was preionized in the manner illustrated in Fig. A.3B. It should be mentioned that other experiments, not referred to in Table A.1, in which the preionization and main pulses were conducted through the same coil (Fig. A.3A) produced markedly lower performance ($\eta_t=7\%$, $I_{sp}=800$ s in the 30 cm thruster case). In both schemes, the initial pulse accomplished the goal of preionizing the propellant. However, in the lower performance case the preionization pulse also partially accelerated the plasma away from the coil face, reducing the level of energy coupling between the main discharge pulse and

Table A.1: Estimated maximum performance values for 20 cm[12] and 30 cm[13] diameter pulsed inductive accelerators.

	Ambient Propellant Fill		Pulsed Gas Injection	
Preionization (using Fig. A.3B setup)	No	Yes	No	Yes
20 cm OD	$\eta_t = 6.2\%$ $I_{sp} = 1350$ s $C = 1.75$ μ F	11% 2800 s 3.9 μ F	5.5% 1200 s 3.9 μ F	- - -
30 cm OD (6 μ F/675 J)	$\eta_t = 17\%$ $I_{sp} = 1430$ s	- -	5% 500 s	18% 1470 s

the plasma. The coil located 4 cm downstream, on the other hand, launched a preionized current sheet *towards* the acceleration coil. This compressed the propellant and ionized gas into a thin, conductive region just above the coil and allowed for much greater coupling between the coil current pulse and the plasma sheet, yielding markedly improved I_{sp} and η_t .

A.1.2 Thruster System Development: 1979-1988

In the late 1970s, research at TRW became more focused on developing a full-scale engineering model of the pulsed inductive thruster with relatively high performance. Also during this phase, thruster performance was typically evaluated using a thrust balance as opposed to calculating the thrust from various field measurements. Preionization of the gas was not employed in the experiments performed during this time period. Additionally, these thrusters exclusively used a pulsed mass injection system, since an ambient fill cannot be used in a real thruster.

The biggest design change implemented during this time period was an increase of the acceleration coil diameter to one meter, which studies indicated would substantially increase performance[56]. The larger coil served to increase coil's inductance, consequently increasing the fractional change of total circuit inductance during a current pulse ($\Delta L/L_0$), by increasing the surface area of the coil and increasing the distance over which the coil and plasma sheet remain coupled.

The thruster used for tests in the early 1980s possessed a coil comprised of 36 one-turn spiral wires connected in parallel to a 20 μF capacitor bank. The bank stored 4 kJ of energy per pulse and was switched using a triggered spark gap. Performance measurements for this thruster are summarized in Table A.2. In Ref. [40], the thruster's performance was calculated by integrating the field distribution over the entire discharge volume. The

Table A.2: Performance of a 1 m diameter pulsed inductive thruster (from Refs. [40] and [57]). The performance was computed in each case using the indicated method. The data from Ref. [40] were obtained at two separate mass bits.

Publication Year	I_{sp} [s]	η_t [%]	Measurement Method
1982 (from Ref. [40])	1540	42	$\int j_\theta B_r dV$
	2240	50	
1984 (from Ref. [57])	1620	44	$\int j_\theta B_r dV$ Thrust Balance
	1236	25.4	

performance inferred from field measurements was compared to direct thrust measurements in Ref. [57].

The data from both Refs. [40] and [57] indicate improved performance over all previous designs. The performance values obtained using a thrust balance were much lower than the corresponding values calculated by integrating the field measurements. This suggested that the integral of the Lorentz body force should not be used to evaluate pulsed inductive thruster performance as it appears to overstate both I_{sp} and η_t .

In the late 1980s, a second series of studies were performed using several different thrusters[4, 5, 58]. The results obtained for two of these thrusters (designated the PIT MkI and MkIV) were particularly insightful and discussed extensively in the literature. Other than the number of spiral wires comprising the acceleration coil, the MkI was an exact replica of the early 1980s design (24 single-turn wires versus the previous version's 36 wires). The PIT MkIV acceleration coil was essentially a shrunken version of the MkI, possessing a diameter of 0.67 meters. In addition, its discharge circuit could be operated in a “ringing” mode, where charge could build-up on either side of the capacitor, or a “clamped” mode, where diodes were employed to keep the current flowing through the acceleration coil in the same direction for a longer period of time (see Fig. A.4). The

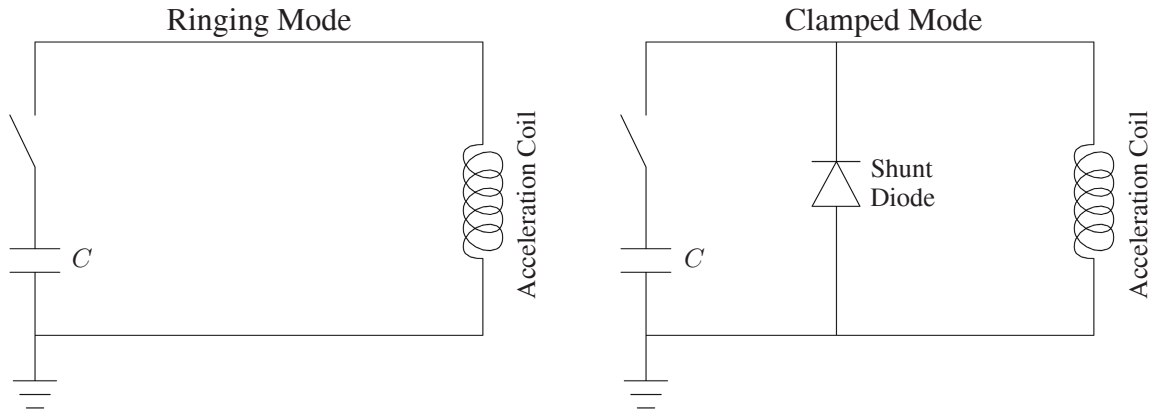


Figure A.4: Circuit schematics for the PIT MkIV operating in a ringing and clamped mode (after Ref. [4]).

clamped mode was intended to keep the current flowing in the same direction so that it couldn't reverse and ignite a secondary discharge that would short-circuit the acceleration of the initial sheet before it was decoupled from the acceleration coil.

A plot of performance measurements for the MkI and MkIV designs is presented in Fig. A.5. These data are based upon impulse measurements obtained using a thrust balance. The magnitude of the MkI thrust is consistent with the thrust balance performance measurement presented in Table A.2. However, the smaller diameter MkIV coil possessed a lower performance. In addition, the clamped mode exhibited lower performance than the ringing circuit.

Insight into the markedly lower MkIV performance can be gained from induced magnetic field measurements, which were obtained at several axial locations in both the MkI (Fig. A.6) and MkIV (Fig. A.7) thrusters. In the MkIV (ringing mode), all of the induced field waveforms initially increase at $t = 0$, indicating rapid resistive diffusion of the magnetic field through the plasma (low conductivity). However, the increases in the MkI waveforms occur at different times, which is indicative of a high conductivity current sheet passing the different spatial locations. In the MkI, the waveforms also increase

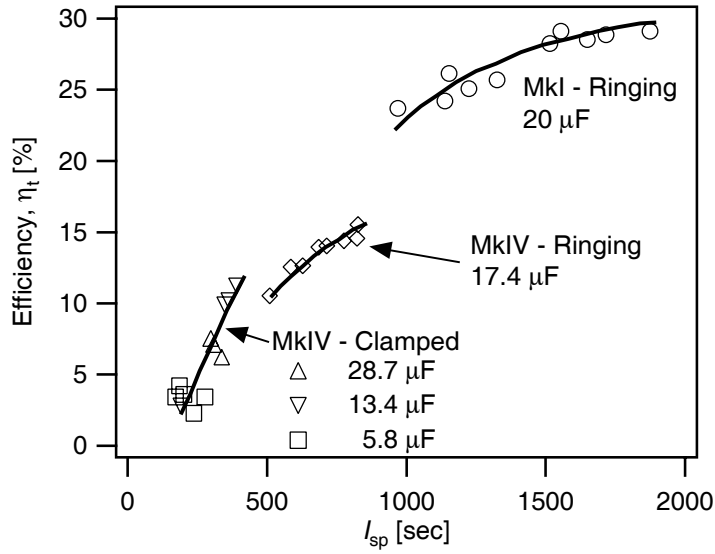


Figure A.5: Performance data for the PIT MkI and MkIV devices operating with argon propellant (from Refs. [4, 5]). Lines added to show performance trends.

more rapidly to greater peak values due to lower initial inductance in the circuit relative to the MkIV. Once the current sheet passes, the MkI waveforms all behave identically, indicating efficient sweeping of the plasma out of the acceleration region during the first half-cycle. On the other hand, the waveforms obtained during the second half-cycle of the MkIV discharge show a second current sheet (“crowbar” discharge). This implies that the current sheet, formed during the first half-cycle of the discharge, did not effectively sweep the plasma out of the acceleration region, thus allowing for coupling between the external circuit and the remaining plasma during the second half-cycle.

The major conclusion of these studies was that the poorer performance of the MkIV could be traced to its higher parasitic inductance. As such, the initial current rise rate, dI/dt , and peak current level in the MkIV acceleration coil were markedly lower than those found in the MkI, leading to an incomplete breakdown during the first half-cycle of the discharge in the MkIV.

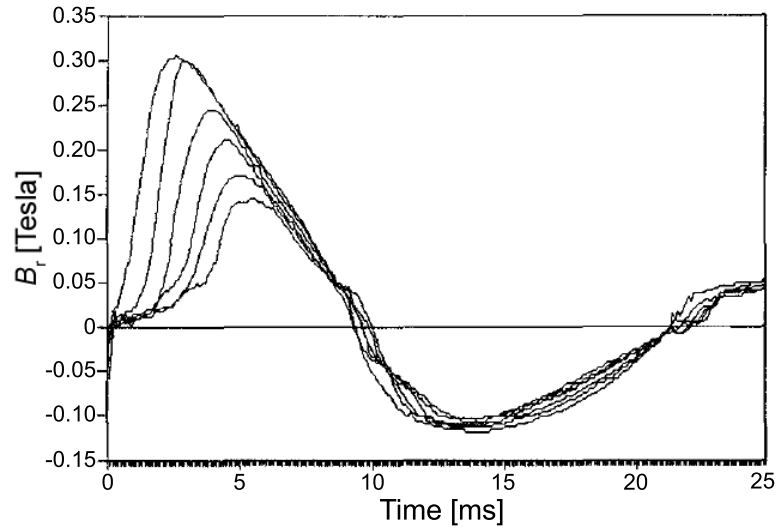


Figure A.6: Magnetic field, B_r , measurements in the PIT MkI for axial locations of $z=1, 2, 3, 4, 5, 6$ cm away from the acceleration coil (from Refs. [4, 5]).

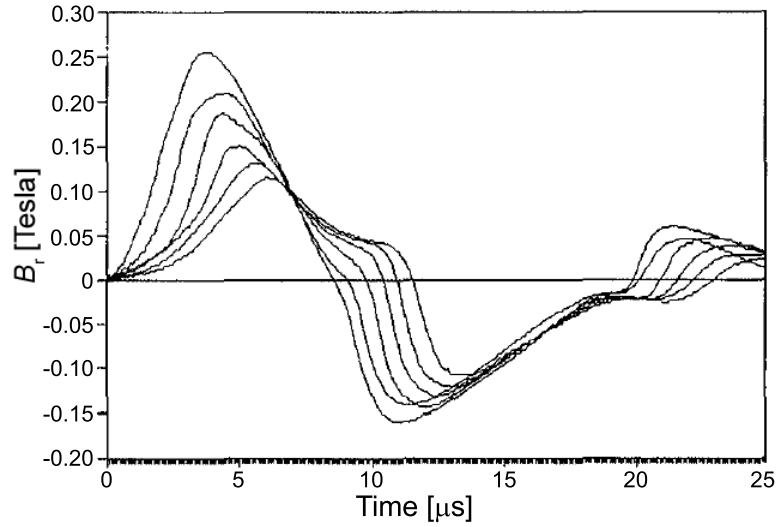


Figure A.7: Magnetic field, B_r , measurements in the PIT MkIV (ringing mode) for axial locations of $z=1, 2, 3, 4, 5, 6$ cm away from the acceleration coil (from Refs. [4, 5]).

A.1.3 Current State-of-the-Art: 1991-Present

PIT MkV

In the early 1990s, the TRW group designed and constructed the PIT MkV accelerator[1, 3, 59] (see Fig. A.8). This design still represents the current state-of-the-art for the PIT.

The MkV design was guided by the results gathered using the MkI and MkIV thrusters. Specifically, those studies highlighted the importance of forming an impermeable current sheet capable of efficiently entraining and accelerating all the propellant it encountered. The MkV thruster was designed with a lower parasitic inductance than previous design iterations. Moreover, the initial azimuthal voltage drop on the acceleration coil was substantially increased over that of past thrusters. Both of these changes increase the initial current rise rate, dI/dt , in the acceleration coil which, in turn, increases the speed of the breakdown

From a practical perspective, lowering the parasitic inductance is a matter of maintaining tight tolerances and minimal clearances between the thruster transmission lines. To increase the azimuthal voltage drop, a new coil design was implemented. The coil was still one-meter in diameter, but it was reconfigured from a single capacitor bank connected

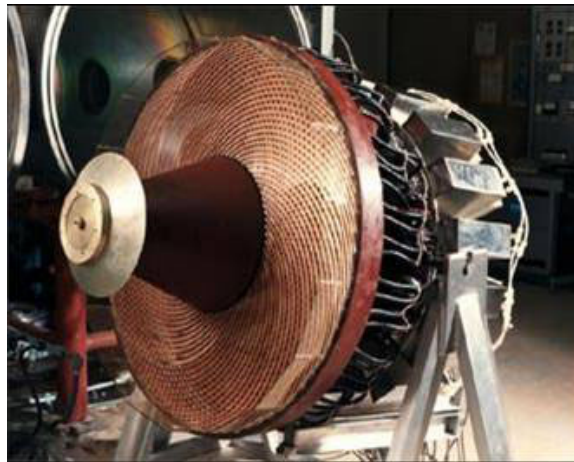


Figure A.8: Photograph of the PIT MkV (from Ref. [1]).

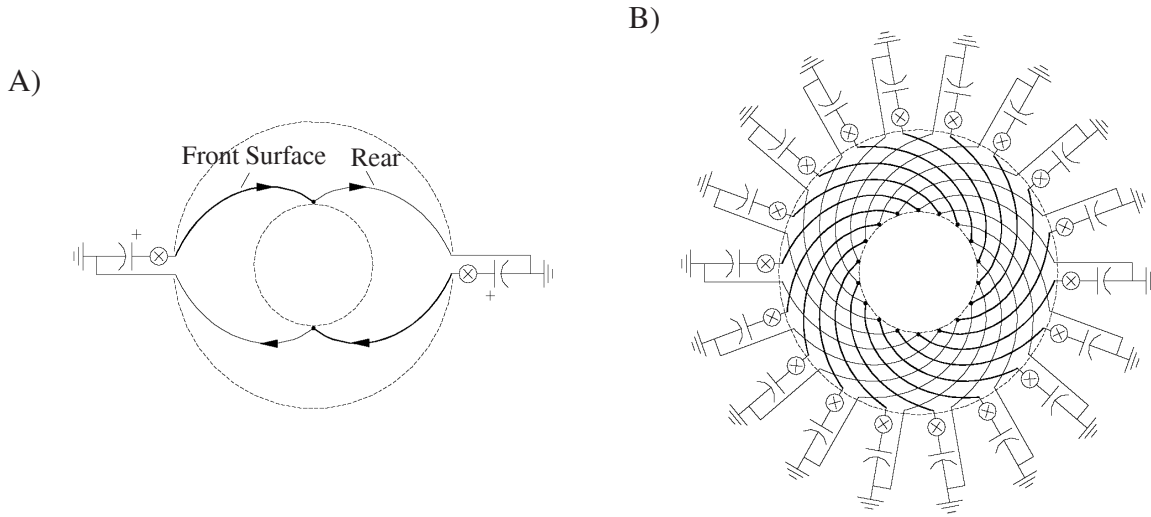


Figure A.9: Marx generator PIT coil configuration. A) One complete loop of a half-turn Marx generator. B) The nine complete loops comprising the PIT MkV. (from Ref. [1]).

in parallel to a set of single-turn spirals of a Marx-generator coil. One complete loop of the Marx-generator configuration is illustrated schematically in Fig. A.9A. Essentially, two capacitors are connected in series by two half-turn spiral conductors. To keep the induced magnetic field uniform over the face of the coil, the conductors spiral radially inward on the front face of the accelerator over their first quarter-turn and spiral radially outward over the second quarter-turn. This configuration yields an azimuthal voltage drop around a complete loop equal to twice the voltage on each capacitor. In other words, charging the capacitors to V_0 results in a total azimuthal voltage drop of $2V_0$. In the MkV, the Marx-generator configuration is repeated nine times to yield the coil shown in Fig. A.9B.

The performance of the PIT MkV was characterized extensively through thrust balance measurements. A data set showing measured performance, I_{sp} and η_t , as a function of mass bit using ammonia as the propellant is presented in Fig. A.10. The essential feature to notice is that the MkV has essentially constant efficiency over a broad range of I_{sp} . A summary of the MkV performance for different propellants is given in Table A.3. The performance on ammonia and hydrazine are markedly higher than in previous thrusters.

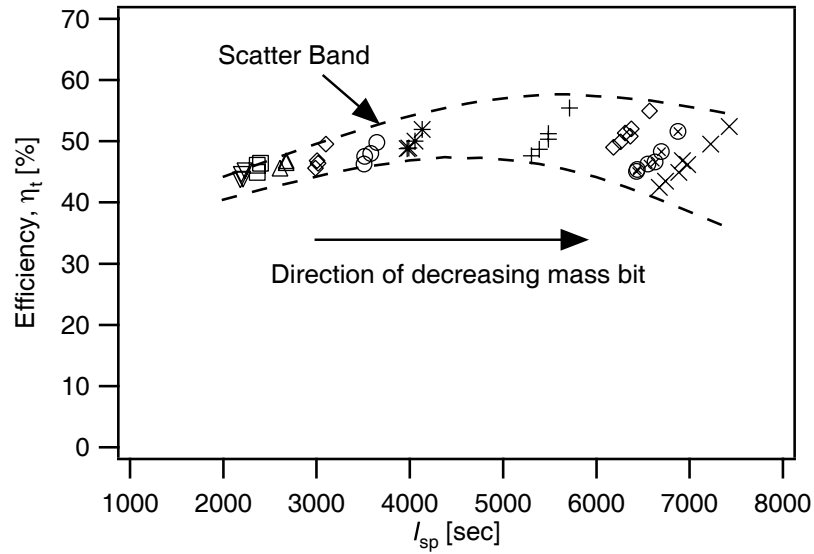


Figure A.10: Performance data for the PIT MkV operating with ammonia propellant at a capacitor bank voltage of 15 kV (after Ref. [3]). Different symbols represent different mass bits.

However, note that the performance values for argon are quite similar to those previously obtained in the MkI thruster operating on argon (compare to Fig. A.5).

Component/Subsystem Level Engineering

Since the introduction of the MkV design, PIT research has been focused on improving subsystems and components which otherwise could either detrimentally affect the thruster's

Table A.3: Ranges of I_{sp} and η_t for the PIT MkV operating on different propellants (from Ref. [46]).

Propellant	I_{sp} [s]	η_t [%]
Ammonia	3000-8000	50
Hydrazine	2500-5000	40
Argon	1000-2000	20-30
Carbon Dioxide	1000-2000	20-30

performance or limit its lifetime in the event of a failure. Many of these components, while acceptable for single-pulse operation, cannot handle the added stress of continuously-pulsed operation. This is especially critical since it has been proposed that PIT, in order to meet mission requirements, should operate at a high repetition rate (~ 50 - 100 Hz). We close our review of the PIT by briefly reviewing critical design changes and current research associated with the development of a long lifetime, reliable, high repetition rate thruster.

Capacitors The capacitors must operate in vacuum at a high repetition rate (~ 50 - 100 Hz). They must also withstand current reversal and ringing in the thruster circuit over the course of many shots (10^9 - 10^{10}) without experiencing lifetime degradation. Polypropylene all-film energy discharge capacitors have been life tested in the range of 10^{10} - 10^{11} total shots and have been employed in all recent PIT designs[3]. Mica capacitors also represent a long-lived technology[60], providing a possible alternative to the polypropylene capacitor design.

Propellant Valves The propellant valve currently in use in the MkV is essentially the same magnetically driven design originally developed for the MkI[58, 59], though the latest design uses an electromagnet coil instead of permanent magnets[61]. The seats and seals are required to be long-lived to minimize the propellant leak rate, especially later in the thruster's lifetime. The valve is required to yield an accurately controlled and evenly metered mass bit. It must also open and close rapidly (traversing a 0.5 mm gap in $150 \mu\text{s}$) to abruptly cut off the propellant flow and minimize waste.

High-Current Switches Spark-gap switches have been used in all previous versions of the PIT, but they are a major life-limiting component in the design. They erode like any other set of electrodes exposed to a high-current arc, and their erosion rates can be significant. Their presence also keeps the PIT from being a true *electrodeless* device. As such, efforts have been underway to replace the spark gaps with high-current, solid-state thyristors

(SCRs). Specifically, the requirements on the thyristors were as follows: standoff voltage = 15 kV, $dI/dt \geq 20 \text{ kA}/\mu\text{s}$, peak current $\geq 13 \text{ kA}$, and voltage fall time $\leq 300 \text{ ns}$ [46, 62]. While proof-of-concept experiments have shown that a set of stacked thyristors can meet these requirements, they have yet to be incorporated into a full pulsed inductive accelerator for testing. It should be pointed out that although they do not erode like spark gap switches, the type of SCRs which are capable of fulfilling the stated requirements are typically quite bulky and may impose a significant mass penalty on the system.

Active Cooling A PIT operating at high repetition rates ($\sim 50\text{-}100 \text{ Hz}$) and high power levels (hundreds of kW to MWs) will, of course, experience far greater heating rates than previous single-shot devices. The entire circuit (acceleration coil, thyristors, capacitors) will be subjected to enhanced resistive heating. In addition, studies have estimated that the amount of energy radiated back to the thruster from the plasma could be substantial[1]. The thruster components must be either capable of handling these thermal loads or the heat must be removed in some way. The latter option was chosen in the construction of the MkVI. All the conductors, including the acceleration coil itself, were constructed out of hollow copper tubing[62]. This allowed for a cooling fluid to be passed through the system to remove excess heat.

A.2 Other Pulsed Inductive Acceleration Concepts

A.2.1 Theta Pinch

One of the simplest and oldest pulsed inductive plasma acceleration devices in existence is the theta pinch. It is illustrated in Fig. A.11, along with its derivative, the conical theta pinch. These devices consist of a capacitor connected to a single-turn, theta-pinch coil located external to the working gas. When the capacitor is discharged through the coil,

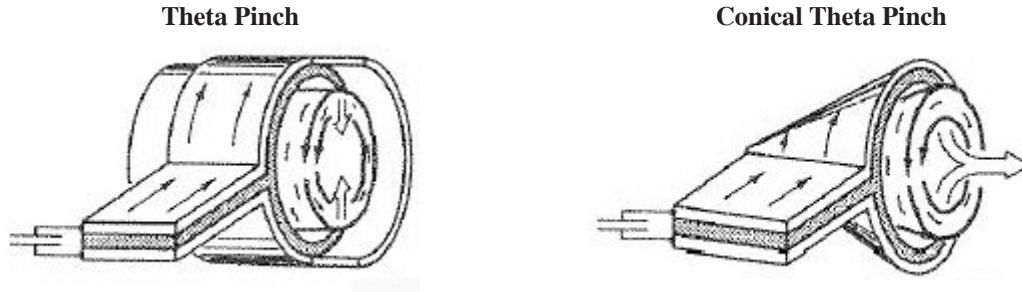


Figure A.11: Schematic representations of a theta pinch and conical theta pinch (from Ref. [2]). Small arrows indicate directions in which currents flow. Large arrows indicate direction of plasma motion.

current flows in the azimuthal (theta) direction and inductively breaks down the gas within the interior of the coil. A cylindrical current sheet forms as the current in the external coil inductively couples to the plasma by inducing azimuthal currents in the opposite direction. The induced current density, j_θ , interacts with the induced axial magnetic field, B_z , to yield a radial Lorentz body force which compresses the plasma within the cylinder.

There have been several investigations into the structure of a theta pinch. Examples of investigations into the plasma and field properties and shock structure of the imploding current sheet can be found in Refs. [54, 63] and the references therein. These studies showed that while there was ionization during the first half-cycle of the discharge, it was generally not sufficient to allow for the formation of a current sheet. However, this preionization did allow for more complete ionization and current sheet formation during the second half-cycle of the discharge.

A scaling analysis for a high-power theta-pinch propulsion scheme is given in Ref. [64]. However, there do not appear to be any experimental studies aimed at investigating the propulsive usefulness of theta pinches. Having said that, we can still conceptually envision the mechanism by which such devices might actually produce thrust.

In the case of the conical theta pinch, it is simple to see that a radial component of

the induced magnetic field exists which serves to axially accelerate the plasma as it is compressed, thus yielding thrust. It is, however, more difficult to see how the momentum associated with a radially imploding plasma could be converted into axially streaming momentum in a standard theta-pinch. There exists a great degree of symmetry between the theta pinch and another class of plasma accelerators known as Z-pinches, which have been investigated for propulsive purposes[16, 65, 66]. In the Z-pinch configuration the axial component of the current density, j_z , interacts with an azimuthal self-magnetic field, B_θ , to yield radial plasma compression. It has been found that as the current sheet implodes, highly accelerated jets of plasma can be formed due to conversion of thermal plasma enthalpy into axially-directed kinetic energy[67]. One may expect similar results in a theta-pinch device due to the symmetry between the two, though the presence of electrodes in the Z-pinch configuration may not allow for such a direct comparison between the two concepts.

A.2.2 Field-Reversed Configuration

The class of plasma devices in which closed magnetic field configurations exist are referred to as compact toroids. These plasma devices are typically classified by the relative strengths of the poloidal and toroidal magnetic fields, B_P and B_T , respectively. A compact toroid in which $B_P \approx B_T$ is known as a spheromak while that in which $B_P \gg B_T$ is called a field-reversed configuration (FRC). Note that spheromaks also possess both poloidal and toroidal plasma currents while those in an FRC are only in the toroidal direction.

FRCs, which have been studied quite extensively[68], possess some unique properties which make them interesting for fusion applications. The ratio of the plasma thermal energy to the magnetic field energy (β) in an FRC is high (≈ 1). Unlike other high β plasmas, FRCs can be magnetically confined for relatively long periods of time, exhibiting a high

degree of macroscopic stability. They are apparently free from gross instabilities and remain coherent under axial motion. The first experimental studies involving an FRC was performed by Alfvén *et al.*[69] FRCs have typically been created using a field-reversed theta-pinch method illustrated in Fig. A.12. The process merits its own discussion as it is different than the theta pinch acceleration process described previously.

In the top panel of Fig. A.12, an initial current flows in the theta-pinch coil, which inductively preionizes a portion of the gas while simultaneously generating a bias magnetic field. The plasma is sufficiently preionized during this first stage that the magnetic field lines induced during the first half-cycle are trapped or “frozen-in”. In step two, the current in the coil reverses. This induces a magnetic field at the wall of the theta-pinch coil which is directed in the opposite direction of the initial, bias field. The new field proceeds to radially

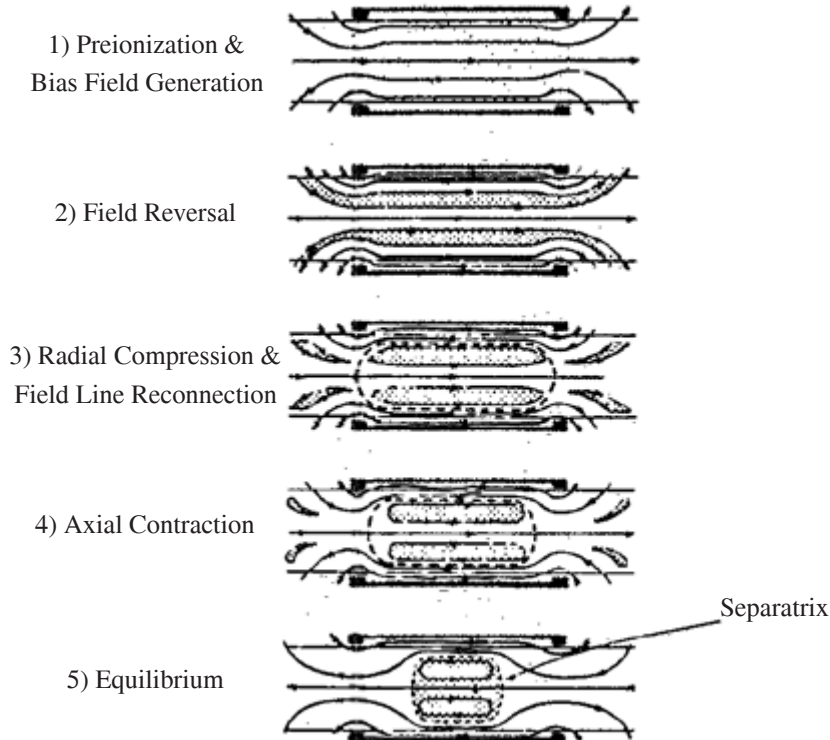


Figure A.12: Stages in the formation of an field-reversed theta-pinch plasma (from Ref. [70]).

compress the bias field and plasma in step three, increasing the ionization of the plasma and eventually causing the bias field lines to break and then reconnect with themselves to form the FRC field configuration. The FRC is further compressed in step four and finally reaches equilibrium in step five. While one can imagine that separate capacitors, switches and inductive coils could be used for the different inductive processes (preionization, bias field application and field reversal), in most experiments all these processes have been accomplished by a single, underdamped circuit.

A cursory examination of the fusion literature reveals why FRC plasmas are interesting for propulsion. They are relatively dense and coherent structures that can be accelerated by an externally-applied magnetic field. The translation and acceleration of FRC plasmas have been achieved using a linear series of theta pinches[71] and magnetic mirrors[72]-[75]. They have been shown to be quite stable, maintaining their cohesion even at super-Alfvénic speeds. Also, since the FRC plasma structure excludes external magnetic fields, it doesn't encounter issues associated with detachment inherent in several other magnetic nozzle-based propulsion concepts.

Recently it has been proposed to use low temperature FRC plasmas (also called plasmoids) for propulsion[76]. In this concept, illustrated in Fig. A.13A, an FRC plasma is formed using the field-reversed theta pinch method. It then accelerates by expanding along an electrically conducting nozzle. A plasmoid-based proof-of-concept accelerator (illustrated in Fig. A.13B) was recently constructed and tested[77]. In that experiment, the FRC plasma was created using a conical theta-pinch coil. The magnetic field is stronger at the smaller theta-pinch coil radius and preferentially accelerates the plasmoid in the direction indicated in figure in much the same way that FRC plasmas have been accelerated by magnetic mirrors. To date, the performance of plasmoid-based accelerators has not been quantified.

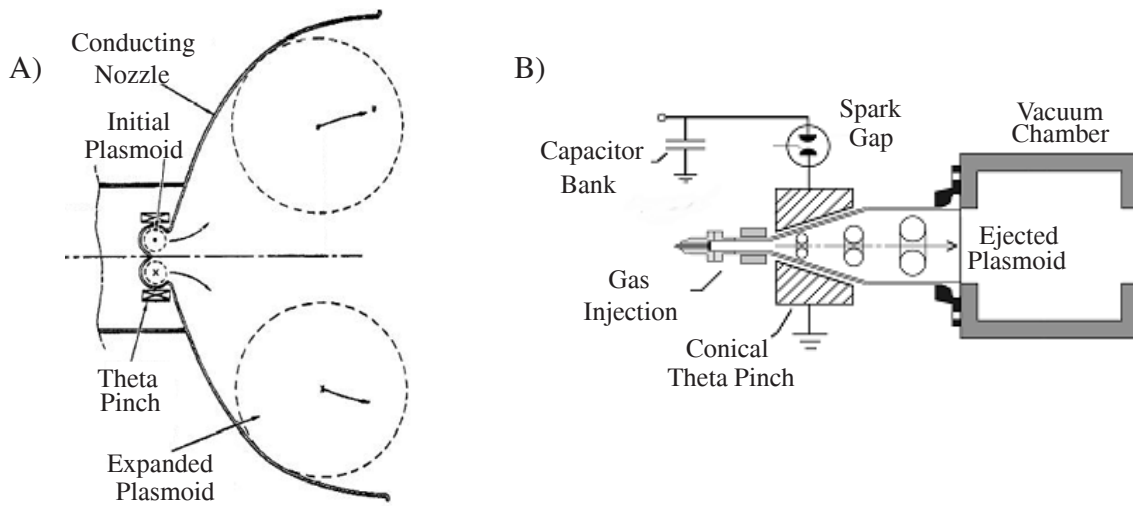


Figure A.13: Schematic representation of a pulsed plasmoid thruster consisting of A) a theta-pinch plasma source and electrically conducting nozzle for FRC plasma expansion (from Ref. [76]) and B) a conical theta-pinch source with expansion against the induced magnetic field lines (not shown) (from Ref. [77]).

A.3 Summary

Except for the PIT program, there has been very little research investigating pulsed inductive plasma acceleration for propulsive purposes. Consequently, the PIT currently represents the state-of-the art in inductive thruster technology, and there has been a wealth of fundamental and practical knowledge gained throughout the lifetime of that research program. The performance of this thruster is also the metric by which all other inductive propulsion concepts are currently measured.

The findings from the review of PIT research are summarized as follows:

- The current in the inductive current sheet is primarily conducted by electrons.
- Axial acceleration of the current sheet is primarily accomplished by the polarization electric field which arises due to charge separation.
- Uneven gas distributions can detrimentally affect current sheet formation and propel-

lant sweeping efficiency.

- Preionization does facilitate uniform current sheet formation and enhances propellant sweeping efficiency if the preionized plasma is near to or compressed against the acceleration coil face.
- Increasing the ratio $\Delta L/L_0$ increases thruster efficiency (Lovberg criteria).
- Decreasing the parasitic inductance, L_0 , or increasing the initial azimuthal voltage drop across the acceleration coil increases the rate of current sheet formation. This leads to a faster, more complete breakdown and higher propellant sweeping efficiencies.
- Pulsed inductive thrusters employing current sheets possess relatively constant thrust efficiency over a broad range of specific impulse.
- For a real mission, high-current switches and capacitors must be able to survive for 10^9 - 10^{10} shots while operating at a high repetition rates between 50 and 100 Hz. These problems are compounded by the fact that the PIT operates at high charge voltages and discharge currents, which additionally strain the system.

The PIT's large size and the complexity associated with switching multiple capacitors across the induction coil simultaneously may limit its applicability relative to other, more compact and mature thruster systems. While very little effort has been invested in researching theta-pinch devices for propulsive purposes, there is a large and quite substantial body of work in the field of controlled nuclear fusion. It remains to be seen whether theta-pinches can be used to produce fast, axially-streaming plasmas useful for spacecraft propulsion.

Appendix B

Computer Algorithms

The computational algorithms used to generate the data found in Chapter 5 are given in this appendix. The algorithms are specialized to solve for one of the following three mass distributions: slug mass loading, triangular (PIT-like) mass loading, and uniform fill mass loading. In each case, a main program, named *solver.m*, initializes the variables, calls a subroutine to solve the set of differential equations, and then performs post-processing to yield data consistent with our computation termination assumptions. The differential equation sets for each case are given after the *solver.m* program.

Slug Mass Loading

solver.m

```
clear all
%
global m; % psi1 vector position
global n; % psi2 vector position
global p; % alpha vector position
global mm; % L vector position
global pp; % gamma vector position
global nn; % nu vector position
%
%=====
% data inputs
%
% psi1: critical resistance ratio 1
% psi2: critical resistance ratio 2
% L: inductance ratio [(L_0/L_C)]
% alpha: dynamic impedance
% gamma: applied field dynamic impedance
% nu: applied field back-EMF parameter
%=====
%
global psi1;
global psi2;
global L;
global nu;
global alpha;
global gamma;
%
psi1=[.0095 0.01 0.015 0.02 0.025 0.03 0.035 0.04 0.045 0.05 ...
      0.055 0.06 0.065 0.07 0.075 0.08 0.085 0.09 0.095 0.1 ...
      0.15 0.2 0.25 0.3 0.35 0.4 0.45 0.5 0.55 0.6 0.65 0.7 ...
      0.75 0.8 0.85 0.9 0.95 1 1.5 2 2.5 3 3.5 4 4.5 5 5.5 6 ...
      6.5 7 7.5 8 8.5 9 9.5 10];
%
psi2=[0.01 0.015 0.02 0.025 0.03 0.035 0.04 0.045 0.05 ...
      0.055 0.06 0.065 0.07 0.075 0.08 0.085 0.09 0.095 0.1 ...
      0.15 0.2 0.25 0.3 0.35 0.4 0.45 0.5 0.55 0.6 0.65 0.7 ...
      0.75 0.8 0.85 0.9 0.95 1 1.5 2 2.5 3 3.5 4 4.5 5 5.5 6 ...
      6.5 7 7.5 8 8.5 9 9.5 10];
%
L=[.1 .2 .3 .4 .5 .6 .7 .8 .9 1.0 1.5 2 2.5 3 3.5 4 4.5 ...
   5 5.5 6 6.5 7 7.5 8 8.5 9 9.5 10];
%
alpha=[0.1 0.15 0.2 0.25 0.3 0.35 0.4 0.45 0.5 0.55 0.6 0.65 ...
      0.7 0.75 0.8 0.85 0.9 0.95 1 1.5 2 2.5 3 3.5 4 4.5 5 5.5 ...
      6 6.5 7 7.5 8 8.5 9 9.5 10 15 20 25 30 35 40 45 50 55 60 ...
      65 70 75 80 85 90 95 100];
%
gamma=[0.001 0.0015 0.002 0.0025 0.003 0.0035 0.004 0.0045 0.005 ...
      0.0055 0.006 0.0065 0.007 0.0075 0.008 0.0085 0.009 ...
      0.0095 0.01 0.015 0.02 0.025 0.03 0.035 0.04 0.045 0.05 ...
      0.055 0.06 0.065 0.07 0.075 0.08 0.085 0.09 0.095 0.1];
%
nu=[0.001 0.0015 0.002 0.0025 0.003 0.0035 0.004 0.0045 0.005 ...
    0.0055 0.006 0.0065 0.007 0.0075 0.008 0.0085 0.009 ...
    0.0095 0.01 0.015 0.02 0.025 0.03 0.035 0.04 0.045 0.05 ...
    0.055 0.06 0.065 0.07 0.075 0.08 0.085 0.09 0.095 0.1 ...
    0.15 0.2 0.25 0.3 0.35 0.4 0.45 0.5 0.55 0.6 0.65 0.7 ...
```

```

        0.75 0.8 0.85 0.9 0.95 1];
%
%
% Allow for solutions while different variables are held fixed
% Comment out terms being varied
%

psi1(1)=0.05;
psi2(1)=0.13;
alpha(1)=2.1;
L(1)=80/660;
gamma(1)=0;
nu(1)=0;
%
I=1; % number of psi1 elements - 56 max
II=1; % number of psi2 elements - 55
J=1; % number of alpha elements - 55
JJ=1; % number of L elements - 28
KK=1; % number of gamma elements - 37
K=1; %number of nu elements -55

for m=1:I,
for n=1:II,
for p=1:J,
for mm=1:JJ,
for pp=1:KK,
for nn=1:K,
%
    options = odeset('RelTol',1e-5,'AbsTol',[1e-5 1e-5 1e-5 1e-5 1e-5 1e-5]);
%
    [T,X] = ode45('eqnset_slug',[0 15],[0 0 1 1 0 0],options);
%
%
% - test to determine if the current I1* crosses zero
% - if it does, search through the current waveform for
%   the first element where it crosses (reverses) and
%   record that element
%
[ala,a1b]=min(X(:,1));
%
a2a = 2;
if ala < 0
    for q=2:a1b,
        if X((q-1),1) > 0
            if X(q,1) < 0
                a2a = q;
            end
        end
    end
end
end
%
%
% - test to determine if the position waveform passes
%   beyond the decoupling distance.
% - if it does, search the waveform to determine the
%   element at which it passes the distance and record it
%
[b1a,b1b]=max(X(:,5));
%
b2a = 2;
if b1a > 3
    for q=2:b1b,
        if X((q-1),5) < 3
            if X(q,5) > 3

```

```

        b2a = q;
    end
end
end
end
%
%
% - if a current reversal or the sheet travelling the given
% distance did not occur, use the final value of the velocity
% from the calculation
%
m1=size(X,1);
if (a2a==2 & b2a==2)
    vz=X(m1,6);
%
else
%
% - current reverses before z*=3
%
    if ((a2a < b2a & a2a ~= 2) | b2a == 2)
        vz=X(a2a,6);
%
% - sheet reaches z*=3 before current reversal
%
    else
        vz=X(b2a,6);
    end
end
end
%
    etaT(pp,nn)=(vz^2)/(2*L(mm)*alpha(p))*100;
    velocity(pp,nn)=vz;
%
end
end
end
end
end
end
end

```

eqnset_slug.m - called by the ode45 command in *solver.m*

```

function dx = equationset(t,x)
%
global psi1;
global psi2;
global L;
global alpha;
global nu;
global gamma;
%
% counting variables
global m; % psi1 vector position
global n; % psi2 vector position
global p; % alpha vector position
global mm; % L vector position
global nn; % Laf vector position
global pp; % gamma vector position
%
dx=zeros(6,1); % a column vector
%
%=====
% x(1): current in loop 1 [I1*]

```

```

% x(2): current in loop 2 [I2*]
% x(3): charge on capacitor [V*]
% x(4): mutual inductance [M*]
% x(5): position [z*]
% x(6): velocity [v*]
%
% psi1: critical resistance ratio 1
% psi2: critical resistance ratio 2
% L: inductance ratio [(L_0/L_C)]
% alpha: dynamic impedance
% nu: applied field back EMF parameter
% gamma: applied field acceleration
%=====
%
dx(1)=(L(mm)*x(3)+ (x(4)*x(1)+x(2))*((-1/2)*exp(-x(5)/2)*x(6)) ...
-x(2)*x(4)*L(mm)*psi2(n)-x(1)*L(mm)*psi1(m) ...
-L(mm)*x(4)*x(6)*nu(nn))/(L(mm)+1-x(4)^2);

dx(2)=x(4)*((L(mm)*x(3)+ (x(4)*x(1)+x(2))*((-1/2)*exp(-x(5)/2)*x(6)) ...
-x(2)*x(4)*L(mm)*psi2(n)-x(1)*L(mm)*psi1(m)-L(mm)*x(4)*x(6)*nu(nn)) ...
/((L(mm)+1-x(4)^2))+x(1)*((-1/2)*exp(-x(5)/2)*x(6))-x(2)*L(mm)*psi2(n) ...
-x(6)*nu(nn)*L(mm);

dx(3)=-x(1);

dx(4)=(-1/2)*exp(-x(5)/2)*x(6);

dx(5)=x(6);

dx(6)=(alpha(p)*(x(1))^2*exp(-x(5)))+(gamma(pp)*x(2));

```

Triangular Mass Loading

solver.m

```

clear all
%
global m; % psi1 vector position
global n; % psi2 vector position
global p; % alpha vector position
global mm; % L vector position
global pp; % gamma vector position

%=====
% data inputs
%
% psi1: critical resistance ratio 1
% psi2: critical resistance ratio 2
% L: inductance ratio [(L_0/L_C)]
% alpha: dynamic impedance
% gamma: applied field dynamic impedance
% mass: initial sheet mass
% nu: applied field back-EMF parameter
%=====
%
global psi1;
global psi2;
global L;

```



```

global alpha;
global nu;
global gamma;
global mass;
global rho;
global mass_t;
global delta;
%
psi1=[.0095 0.01 0.015 0.02 0.025 0.03 0.035 0.04 0.045 0.05 ...
      0.055 0.06 0.065 0.07 0.075 0.08 0.085 0.09 0.095 0.1 ...
      0.15 0.2 0.25 0.3 0.35 0.4 0.45 0.5 0.55 0.6 0.65 0.7 ...
      0.75 0.8 0.85 0.9 0.95 1 1.5 2 2.5 3 3.5 4 4.5 5 5.5 6 ...
      6.5 7 7.5 8 8.5 9 9.5 10];
%
psi2=[0.01 0.015 0.02 0.025 0.03 0.035 0.04 0.045 0.05 ...
      0.055 0.06 0.065 0.07 0.075 0.08 0.085 0.09 0.095 0.1 ...
      0.15 0.2 0.25 0.3 0.35 0.4 0.45 0.5 0.55 0.6 0.65 0.7 ...
      0.75 0.8 0.85 0.9 0.95 1 1.5 2 2.5 3 3.5 4 4.5 5 5.5 6 ...
      6.5 7 7.5 8 8.5 9 9.5 10];
%
L=[.1 .2 .3 .4 .5 .6 .7 .8 .9 1.0 1.5 2 2.5 3 3.5 4 4.5 ...
   5 5.5 6 6.5 7 7.5 8 8.5 9 9.5 10];
%
alpha=[0.1 0.15 0.2 0.25 0.3 0.35 0.4 0.45 0.5 0.55 0.6 0.65 ...
      0.7 0.75 0.8 0.85 0.9 0.95 1 1.5 2 2.5 3 3.5 4 4.5 5 5.5 ...
      6 6.5 7 7.5 8 8.5 9 9.5 10 15 20 25 30 35 40 45 50 55 60 ...
      65 70 75 80 85 90 95 100];
%
gamma=[0.001 0.0015 0.002 0.0025 0.003 0.0035 0.004 0.0045 0.005 ...
      0.0055 0.006 0.0065 0.007 0.0075 0.008 0.0085 0.009 ...
      0.0095 0.01 0.015 0.02 0.025 0.03 0.035 0.04 0.045 0.05 ...
      0.055 0.06 0.065 0.07 0.075 0.08 0.085 0.09 0.095 0.1];
%
nu=10*gamma;
%
% Set initial mass thickness and gradient
%
mass=0.1;
delta=(4/7.5);
mass_t=1;
rho=(mass_t-mass)*2/delta;
%
%
% Allow for solutions while different variables are held fixed
% Comment out terms being varied
%

psi1(1)=0.05;
psi2(1)=0.13;
alpha(1)=2.1;
L(1)=80/660;
gamma(1)=0;
nu(1)=0;
%
I=1; % number of psi1 elements - 56 max
II=1; % number of psi2 elements - 55
J=1; % number of alpha elements - 55
JJ=1; % number of L elements - 28
KK=1; % number of gamma,nu elements - 37
%
for m=1:I,
for n=1:II,
for p=1:J,
for mm=1:JJ,

```

```

for pp=1:KK,
%
    options = odeset('RelTol',1e-5,'AbsTol',[1e-5 1e-5 1e-5 1e-5 1e-5 1e-5 1e-5]);
%
    [T,X] = ode45('eqnset_triangu',[0 15],[0 0 1 1 0 0 mass],options);
%
%
% - test to determine if the current I1* crosses zero
% - if it does, search through the current waveform for
%   the first element where it crosses (reverses) and
%   record that element

[a1a,a1b]=min(X(:,1));
%
a2a = 2;
if a1a < 0
    for q=2:a1b,
        if X((q-1),1) > 0
            if X(q,1) < 0
                a2a = q;
            end
        end
    end
end
%
%
% - test to determine if the position waveform passes
%   beyond the decoupling distance.
% - if it does, search the waveform to determine the
%   element at which it passes the distance and record it
%
[b1a,b1b]=max(X(:,5));
%
b2a = 2;
if b1a > 3
    for q=2:b1b,
        if X((q-1),5) < 3
            if X(q,5) > 3
                b2a = q;
            end
        end
    end
end
%
%
% - if a current reversal or the sheet travelling the given
%   distance did not occur, use the final value of the velocity
%   from the calculation
%
m1=size(X,1);
if (a2a==2 & b2a==2)
    vz=X(m1,6);
    zz=X(m1,5);
    mass_f=X(m1,7);
%
% - sheet doesn't pass z*=3 and current doesn't reverse
%
    if (zz < 3)
        vz=vz*(mass_f/mass_t); % Adjust velocity for wasted mass
        mass_f=mass_t;
        zz=3;
    end
%

```

```

else
%
% - current reverses before z*=3
%
    if ((a2a < b2a & a2a ~= 2) | b2a == 2)
        vz=X(a2a,6);
        zz=X(a2a,5);
        mass_f=X(a2a,7);
    %
        if (zz < 3)
            vz=vz*(mass_f/mass_t); % Adjust velocity for wasted mass
            mass_f=mass_t;
            zz=3;
        end
    %
% - sheet reaches z*=3 before current reversal
%
    else
        vz=X(b2a,6);
        zz=X(b2a,5);
        mass_f=X(b2a,7);
    end
end
%
etaT(p,pp)=(mass_f)*(vz^2)/(2*L(mm)*alpha(p))*100;
velocity(p,pp)=vz;
%
%
end
end
end
end
end
end

```

eqnset_triangular.m - called by the ode45 command in *solver.m*

```

function dx = equationset(t,x)
%
global psi1;
global psi2;
global L;
global alpha;
global nu;
global gamma;
global mass;
global rho;
global mass_t;
global delta;
%
% counting variables
global m; % psi1 vector position
global n; % psi2 vector position
global p; % alpha vector position
global mm; % L vector position
global pp; % gamma vector position
%
dx=zeros(7,1); % a column vector
%
%=====
% x(1): current in loop 1 [I1*]
% x(2): current in loop 2 [I2*]
% x(3): charge on capacitor [V*]

```

```

% x(4): mutual inductance [M*]
% x(5): position [z*]
% x(6): velocity [v*]
% x(7): mass accumulation [m*]
%
% psi1: critical resistance ratio 1
% psi2: critical resistance ratio 2
% L: inductance ratio [(L_0/L_C)]
% alpha: dynamic impedance
% nu: applied field back EMF parameter
% gamma: applied field acceleration parameter
% mass: initial mass in sheet
%=====
%
dx(1)=(L(mm)*x(3)+ (x(4)*x(1)+x(2))*((-1/2)*exp(-x(5)/2)*x(6)) ...
-x(2)*x(4)*L(mm)*psi2(n)-x(1)*L(mm)*psi1(m) ...
-L(mm)*x(4)*x(6)*nu(pp))/(L(mm)+1)-x(4)^2);

dx(2)=x(4)*((L(mm)*x(3)+ (x(4)*x(1)+x(2))*((-1/2)*exp(-x(5)/2)*x(6)) ...
-x(2)*x(4)*L(mm)*psi2(n)-x(1)*L(mm)*psi1(m)-L(mm)*x(4)*x(6)*nu(pp)) ...
/((L(mm)+1)-x(4)^2))+x(1)*((-1/2)*exp(-x(5)/2)*x(6))-x(2)*L(mm)*psi2(n) ...
-x(6)*nu(pp)*L(mm);

dx(3)=-x(1);

dx(4)=(-1/2)*exp(-x(5)/2)*x(6);

dx(5)=x(6);

if x(7)<(mass_t) % sheet sweeping mass
    dx(6)=((alpha(p)*(x(1))^2*exp(-x(5)))-rho*(1-x(5)/delta)*(x(6))^2 ...
    +(gamma(pp)*x(2)))/x(7);
    dx(7)=rho*(1-x(5)/delta)*x(6);
else % sheet beyond region filled with mass
    dx(6)=((alpha(p)*(x(1))^2*exp(-x(5)))+(gamma(pp)*x(2)))/x(7);
    dx(7)=0;
end

```

Uniform Mass Loading

solver.m

```

clear all
%
global m; % psi1 vector position
global n; % psi2 vector position
global p; % alpha vector position
global mm; % L vector position
global pp; % gamma vector position
%
%=====
% data inputs
%
% psi1: critical resistance ratio 1
% psi2: critical resistance ratio 2
% L: inductance ratio [(L_0/L_C)]
% alpha: dynamic impedance
% gamma: applied field dynamic impedance

```

```

% mass: initial sheet mass
%=====
%
global psi1;
global psi2;
global L;
global alpha;
global nu;
global gamma;
global mass;
global rho;
global mass_t;
%
psi1=[.0095 0.01 0.015 0.02 0.025 0.03 0.035 0.04 0.045 0.05 ...
      0.055 0.06 0.065 0.07 0.075 0.08 0.085 0.09 0.095 0.1 ...
      0.15 0.2 0.25 0.3 0.35 0.4 0.45 0.5 0.55 0.6 0.65 0.7 ...
      0.75 0.8 0.85 0.9 0.95 1 1.5 2 2.5 3 3.5 4 4.5 5 5.5 6 ...
      6.5 7 7.5 8 8.5 9 9.5 10];
%
psi2=[0.01 0.015 0.02 0.025 0.03 0.035 0.04 0.045 0.05 ...
      0.055 0.06 0.065 0.07 0.075 0.08 0.085 0.09 0.095 0.1 ...
      0.15 0.2 0.25 0.3 0.35 0.4 0.45 0.5 0.55 0.6 0.65 0.7 ...
      0.75 0.8 0.85 0.9 0.95 1 1.5 2 2.5 3 3.5 4 4.5 5 5.5 6 ...
      6.5 7 7.5 8 8.5 9 9.5 10];
%
L=[.1 .2 .3 .4 .5 .6 .7 .8 .9 1.0 1.5 2 2.5 3 3.5 4 4.5 ...
   5 5.5 6 6.5 7 7.5 8 8.5 9 9.5 10];
%
alpha=[0.1 0.15 0.2 0.25 0.3 0.35 0.4 0.45 0.5 0.55 0.6 0.65 ...
      0.7 0.75 0.8 0.85 0.9 0.95 1 1.5 2 2.5 3 3.5 4 4.5 5 5.5 ...
      6 6.5 7 7.5 8 8.5 9 9.5 10 15 20 25 30 35 40 45 50 55 60 ...
      65 70 75 80 85 90 95 100];
%
gamma=[0.001 0.0015 0.002 0.0025 0.003 0.0035 0.004 0.0045 0.005 ...
      0.0055 0.006 0.0065 0.007 0.0075 0.008 0.0085 0.009 ...
      0.0095 0.01 0.015 0.02 0.025 0.03 0.035 0.04 0.045 0.05 ...
      0.055 0.06 0.065 0.07 0.075 0.08 0.085 0.09 0.095 0.1];
%
nu=10*gamma;
%
% Set initial mass thickness and density
%
mass=0.1;
mass_t=1;
rho=(mass_t-mass)/3;
%
%
% Allow for solutions while different variables are held fixed
% Comment out terms being varied
%
psi1(1)=0.05;
psi2(1)=0.13;
alpha(1)=2.1;
L(1)=80/660;
gamma(1)=0;
nu(1)=0;
%
I=1; % number of psi1 elements - 56
II=1; % number of psi2 elements - 55
J=1; % number of alpha elements - 55
JJ=1; % number of L elements - 28
KK=1; % number of gamma, nu elements - 37
%

```

```

for m=1:I,
for n=1:II,
for p=1:J,
for mm=1:JJ,
for pp=1:KK,
%
    options = odeset('RelTol',1e-5,'AbsTol',[1e-5 1e-5 1e-5 1e-5 1e-5 1e-5 1e-5]);
%
    [T,X] = ode45('eqnset_uniform',[0 15],[0 0 1 1 0 0 mass],options);
%
%
% - test to determine if the current I1* crosses zero
% - if it does, search through the current waveform for
%   the first element where it crosses (reverses) and
%   record that element

[al1a,al1b]=min(X(:,1));
%
a2a = 2;
if al1a < 0
    for q=2:al1b,
        if X((q-1),1) > 0
            if X(q,1) < 0
                a2a = q;
            end
        end
    end
end
%
%
% - test to determine if the position waveform passes
%   beyond the decoupling distance.
% - if it does, search the waveform to determine the
%   element at which it passes the distance and record it
%
[b1a,b1b]=max(X(:,5));
%
b2a = 2;
if b1a > 3
    for q=2:b1b,
        if X((q-1),5) < 3
            if X(q,5) > 3
                b2a = q;
            end
        end
    end
end
%
%
% - if a current reversal or the sheet travelling the given
%   distance did not occur, use the final value of the velocity
%   from the calculation
%
m1=size(X,1);
if (a2a==2 & b2a==2)
    vz=X(m1,6);
    zz=X(m1,5);
    mass_f=X(m1,7);
%
    if (zz < 3)
        vz=vz*(mass_f/mass_t); % Adjust velocity for wasted mass
        mass_f=mass_t;
        zz=3;
    end
end

```

```

        end
    %
    else
    %
    % - current reverses before z*=3
    %
        if ((a2a < b2a & a2a ~= 2) | b2a == 2)
            vz=X(a2a,6);
            zz=X(a2a,5);
            mass_f=X(a2a,7);
        %
            if (zz < 3)
                vz=vz*(mass_f/mass_t); % Adjust velocity for wasted mass
                mass_f=mass_t;
                zz=3;
            end
        end
    %
    % - sheet reaches z*=3 before current reversal
    %
        else
            vz=X(b2a,6);
            zz=X(b2a,5);
            mass_f=X(b2a,7);
        end
    end
end
%
etaT(n,mm)=(mass_f)*(vz^2)/(2*L(mm)*alpha(p))*100;
velocity(n,mm)=vz;
%
%
end
end
end
end
end
end

```

eqnset_uniform.m - called by the ode45 command in *solver.m*

```

function dx = equationset(t,x)
%
global psi1;
global psi2;
global L;
global alpha;
global nu;
global gamma;
global mass;
global rho;
global mass_t;
%
% counting variables
global m; % psi1 vector position
global n; % psi2 vector position
global p; % alpha vector position
global mm; % L vector position
global pp; % gamma vector position
%
dx=zeros(7,1); % a column vector
%
=====
% x(1): current in loop 1 [I1*]
% x(2): current in loop 2 [I2*]

```

```

% x(3): charge on capacitor [V*]
% x(4): mutual inductance [M*]
% x(5): position [z*]
% x(6): velocity [v*]
% x(7): mass accumulation [m*]
%
% psi1: critical resistance ratio 1
% psi2: critical resistance ratio 2
% L:    inductance ratio [(L_0/L_C)]
% alpha: dynamic impedance
% nu:    applied field back EMF parameter
% gamma: applied field acceleration parameter
% mass:  initial mass in sheet
%=====
%
dx(1)=(L(mm)*x(3)+ (x(4)*x(1)+x(2))*((-1/2)*exp(-x(5)/2)*x(6)) ...
-x(2)*x(4)*L(mm)*psi2(n)-x(1)*L(mm)*psi1(m) ...
-L(mm)*x(4)*x(6)*nu(pp))/(L(mm)+1-x(4)^2);

dx(2)=x(4)*((L(mm)*x(3)+ (x(4)*x(1)+x(2))*((-1/2)*exp(-x(5)/2)*x(6)) ...
-x(2)*x(4)*L(mm)*psi2(n)-x(1)*L(mm)*psi1(m)-L(mm)*x(4)*x(6)*nu(pp)) ...
/((L(mm)+1-x(4)^2))+x(1)*((-1/2)*exp(-x(5)/2)*x(6))-x(2)*L(mm)*psi2(n) ...
-x(6)*nu(pp)*L(mm);

dx(3)=-x(1);

dx(4)=(-1/2)*exp(-x(5)/2)*x(6);

dx(5)=x(6);

if x(7)<(mass_t) % sheet sweeping mass
    dx(6)=((alpha(p)*(x(1))^2*exp(-x(5)))-rho*(x(6))^2+(gamma(pp)*x(2)))/x(7);
    dx(7)=rho*x(6);
else % sheet beyond region filled with mass
    dx(6)=((alpha(p)*(x(1))^2*exp(-x(5)))+(gamma(pp)*x(2)))/x(7);
    dx(7)=0;
end

```


Bibliography

- [1] R.H. Lovberg and C.L. Dailey, *A PIT primer*, Technical Report 005, RLD Associates, Encino, CA, 1994.
- [2] R.G. Jahn, *Physics of Electric Propulsion*, McGraw-Hill, New York, 1968.
- [3] C.L. Dailey and R.H. Lovberg, *The PIT MkV pulsed inductive thruster*, Technical Report NASA-CR-191155, TRW Systems Group, Redondo Beach, CA, July 1993.
- [4] C.L. Dailey and R.H. Lovberg, *PIT clamped discharge evolution*, Technical Report AFOSR-TR-89-0130, TRW Space and Technology Group, Redondo Beach, CA, Dec. 1988.
- [5] R.H. Lovberg and C.L. Dailey, “Current sheet development in a pulsed inductive accelerator”, 25th *AIAA/SAE/ASME/ASEE Joint Propulsion Conference*, Monterey, CA, June 10-12, 1989. AIAA Paper 89-2266.
- [6] E.Y. Choueiri and K.A. Polzin, “Faraday acceleration with radio-frequency assisted discharge (FARAD)”, 40th *AIAA/SAE/ASME/ASEE Joint Propulsion Conference*, Ft. Lauderdale, FL, July 11-14, 2004. AIAA Paper 2004-3940.
- [7] E.Y. Choueiri and K.A. Polzin, “Faraday acceleration with radio-frequency assisted discharge (FARAD)”, *J. Propuls. Power*, Accepted for publication: Sept. 2005.

- [8] F.F. Chen and R.W. Boswell, “Helicons - The past decade”, *IEEE Trans. Plasma Sci.*, **25**(6):1245, Dec. 1997.
- [9] R.W. Boswell and F.F. Chen, “Helicons - The early years”, *IEEE Trans. Plasma Sci.*, **25**(6):1229, Dec. 1997.
- [10] J.A. Lehane and P.C. Thonemann, “An experimental study of helicon wave propagation in gaseous plasma”, *Proc. Phys. Soc.*, **85**(2):301, Feb. 1965.
- [11] C.L. Dailey and R.H. Lovberg, “Current sheet structure in an inductive-impulsive plasma accelerator”, *AIAA J.*, **10**(2):125, Feb. 1972.
- [12] C.L. Dailey, *Pulsed electromagnetic thruster*, Technical Report AFRPL-TR-71-107, TRW Systems Group, Redondo Beach, CA, Dec. 1971.
- [13] C.L. Dailey and H.A. Davis, *Pulsed plasma propulsion technology*, Technical Report AFRPL-TR-73-81, TRW Systems Group, Redondo Beach, CA, July 1973.
- [14] A.R. Ellingboe, R.W. Boswell, J.P. Booth, and N. Sadeghi, “Electron beam pulses produced by helicon-wave excitations”, *Phys. Plasmas*, **2**(6):1807, June 1995.
- [15] R. Spektor and E.Y. Choueiri, “Excitation and propagation of electrostatic ion cyclotron waves in rf-sustained plasmas of interest to propulsion research”, 40th *AIAA/ASME/SAE/ASEE Joint Propulsion Conference*, Ft. Lauderdale, FL, July 11-14, 2004. AIAA Paper 2004-4095.
- [16] T.E. Markusic, K.A. Polzin, E.Y. Choueiri, M. Keidar, I.D. Boyd, and N. Lepsetz, “Ablative Z-pinch pulsed plasma thruster”, *J. Propuls. Power*, **21**(3):392, May-June 2005.

- [17] E.S. Wright, *The design and development of Rogowski coil probes for measurement of current density distribution in a plasma pinch*, Master's Thesis, Dept. of Aerospace and Mechanical Sciences, Report No. 740, Princeton Univ., Princeton, NJ, 1965.
- [18] S.L. Leonard, "Basic macroscopic measurements", in *Plasma Diagnostic Techniques*, pages 8–68, R.H. Huddleston and S.L. Leonard (ed), Academic Press, New York, 1965.
- [19] T.E. Markusic, E.Y. Choueiri, and J.W. Berkery, "Measurements of current sheet canting in a pulsed electromagnetic accelerator", *Phys. Plasmas*, **11**(10):4847, Oct. 2004.
- [20] M. Light, I.D. Sudit, F.F. Chen, and D. Arnush, "Axial propagation of helicon waves", *Phys. Plasmas*, **2**(11):4094, Nov. 1995.
- [21] R.H. Lovberg, "Magnetic probes", in *Plasma Diagnostic Techniques*, pages 69–112, R.H. Huddleston and S.L. Leonard (ed), Academic Press, New York, 1965.
- [22] C.A. Romero-Talamás, P.M. Bellan, and S.C. Hsu, "Multielement magnetic probe using commercial chip inductors", *Rev. Sci. Instrum.*, **75**(8):2664, Aug. 2004.
- [23] T.E. Markusic, *Current sheet canting in pulsed electromagnetic accelerators*, Ph.D. Dissertation, Dept. of Mechanical and Aerospace Engineering, Thesis No. 3102-T, Princeton Univ., Princeton, NJ, 2002.
- [24] H.M. Mott-Smith and I. Langmuir, "The theory of collectors in gaseous discharges", *Phys. Rev.*, **28**(4):727, Oct. 1926.
- [25] S.S. Bushman and R.L. Burton, "Heating and plasma properties in a coaxial gasdynamic pulsed plasma thruster", *J. Propuls. Power*, **17**(5):959, Sept.-Oct. 2001.

- [26] P.J. Turchi and R.G. Jahn, “Cathode region of a quasi-steady MPD arcjet”, *AIAA J.*, **9**(7):1372, July 1971.
- [27] A.P. Bruckner and R.G. Jahn, “Exhaust plume structure in a quasi-steady MPD accelerator”, *AIAA J.*, **12**(9):1198, Sept. 1974.
- [28] R.F. Eckman, L. Byrne, N.A. Gatsonis, and E.J. Pencil, “Triple Langmuir probe measurements in the plume of a pulsed plasma thruster”, *J. Propuls. Power*, **17**(4):762, Sept.-Oct. 2001.
- [29] D.L. Tilley, E.Y. Choueiri, A.J. Kelly, and R.G. Jahn, “Microinstabilities in a 10-kilowatt self-field magnetoplasma dynamic thruster”, *J. Propuls. Power*, **12**(2):381, Mar.-Apr. 1996.
- [30] K.D. Diamant, E.Y. Choueiri, and R.G. Jahn, “The role of spot mode transition in the anode fall of pulsed magnetoplasma dynamic thrusters”, *J. Propuls. Power*, **14**(6):1036, Nov.-Dec. 1998.
- [31] S.-L. Chen and T. Sekiguchi, “Instantaneous direct-display system of plasma parameters by means of a triple probe”, *J. Appl. Phys.*, **36**(8):2363, Aug. 1965.
- [32] K.M. True, *Reflections: Computations and Waveforms*, Technical Report Application Note 807, National Semiconductor, Santa Clara, CA, Mar. 1992.
- [33] F.F. Chen, J.D. Evans, and D. Arnush, “A floating potential method for measuring ion density”, *Phys. Plasmas*, **9**(4):1449, Apr. 2002.
- [34] P. Mikellides, Personal communication, Jan. 2006.
- [35] M. Mitchner and C.H. Kruger, *Partially Ionized Gases*, John Wiley & Sons, New York, 1973.

- [36] F.F. Chen, *Introduction to Plasma Physics and Controlled Fusion: Plasma Physics*, Plenum Publishing Corp., New York, 1984.
- [37] J.D. Huba, *NRL Plasma Formulary*, Plasma Physics Division, Naval Research Laboratory, Washington, DC, 2004.
- [38] S.C. Brown, *Basic Data for Plasma Physics*, American Institute of Physics, New York, 1994.
- [39] J.K. Ziemer and E.Y. Choueiri, “Scaling laws for electromagnetic pulsed plasma thrusters”, *Plasma Sources Sci. Technol.*, **10**(3):395, Aug. 2001.
- [40] R.H. Lovberg and C.L. Dailey, “Large inductive thruster performance measurement”, *AIAA J.*, **20**(7):971, July 1982.
- [41] K.A. Polzin and E.Y. Choueiri, “Performance optimization criteria for pulsed inductive plasma acceleration”, 41st *AIAA/ASME/SAE/ASEE Joint Propulsion Conference*, Tucson, AZ, July 10-13, 2005. AIAA Paper 2005-3694.
- [42] K.A. Polzin and E.Y. Choueiri, “Performance optimization criteria for pulsed inductive plasma acceleration”, *IEEE Trans. Plasma Sci.*, Accepted for publication: Feb. 2006.
- [43] P. Mikellides and D. Kirtley, “MACH2 simulations of the Pulsed Inductive Thruster (PIT)”, 38th *AIAA/ASME/SAE/ASEE Joint Propulsion Conference*, Indianapolis, IN, July 7-10, 2002. AIAA Paper 2002-3807.
- [44] P. Mikellides and C. Neilly, “Pulsed Inductive Thruster, part 1. Modeling, validation and performance analysis”, 40th *AIAA/ASME/SAE/ASEE Joint Propulsion Conference*, Ft. Lauderdale, FL, July 11-14, 2004. AIAA Paper 2004-4091.

- [45] D. Allison and P. Mikellides, “Pulsed Inductive Thruster, part 2. A two-temperature thermochemical model for ammonia”, 40th *AIAA/ASME/SAE/ASEE Joint Propulsion Conference*, Ft. Lauderdale, FL, July 11-14, 2004. AIAA Paper 2004-4092.
- [46] I. Hrbud, M. LaPointe, R. Vondra, C.L. Dailey, and R. Lovberg, “Status of pulsed inductive thruster research”, *Proceedings of the Space Technologies and International Forum (STAIF) 2002 Conference*, M.S. El-Genk (ed), AIP Conference Proceedings **608**:627–632, Feb. 3-7, 2002. Also NASA Technical Report, Document Number 20020048589.
- [47] R.H. Lovberg, B.R. Hayworth, and T. Gooding, *The use of a coaxial plasma gun for plasma propulsion*, Technical Report AE62-0678, G.D. Convair, San Diego, CA, May 1962.
- [48] J.K. Ziemer, *Performance scaling of gas-fed pulsed plasma thrusters*, Ph.D. Dissertation, Dept. of Mechanical and Aerospace Engineering, Thesis No. 3016-T, Princeton Univ., Princeton, NJ, 2001.
- [49] K.A. Polzin and E.Y. Choueiri, “Design rules for high-performance FARAD thrusters”, 29th *International Electric Propulsion Conference*, Princeton, NJ, Oct. 31-Nov. 4, 2005. IEPC Paper 2005-207.
- [50] A.W. Degeling, C.O. Jung, R.W. Boswell, and A.R. Ellingboe, “Plasma production from helicon waves”, *Phys. Plasmas*, **3**(7):2788, July 1996.
- [51] J.K. Ziemer, E.A. Cubbin, E.Y. Choueiri, and D. Bix, “Performance characterization of a high efficiency gas-fed pulsed plasma thruster”, 33rd *AIAA/ASME/SAE/ASEE Joint Propulsion Conference*, Seattle, Washington, July 6-9, 1997. AIAA Paper 97-2925.

- [52] J.K. Ziemer, E.Y. Choueiri, and D. Bix, “Trends in performance improvements of a gas-fed pulsed plasma thruster”, *25th International Electric Propulsion Conference*, Cleveland, OH, Aug. 24-28, 1997. IEPC Paper 97-040.
- [53] C.L. Dailey, “Investigation of plasma rotation in a pulsed inductive accelerator”, *AIAA J.*, **7**(1):13, Jan. 1969.
- [54] R.H. Lovberg, “Investigation of current-sheet microstructure”, *AIAA J.*, **4**(7):1215, July 1966.
- [55] L. Spitzer, *Physics of Fully Ionized Gases*, Interscience, New York, 1956.
- [56] C.L. Dailey and R.H. Lovberg, “Large diameter inductive plasma thrusters”, *14th AIAA/DGLR International Electric Propulsion Conference*, Princeton, NJ, Oct. 30-Nov. 1, 1979. AIAA Paper 79-2093.
- [57] C.L. Dailey and R.H. Lovberg, “Thrust balance performance data for a one-meter pulsed inductive thruster”, *17th JSASS/AIAA/DGLR International Electric Propulsion Conference*, Tokyo, Japan, May 28-31, 1984. IEPC Paper 84-54.
- [58] C.L. Dailey and R.H. Lovberg, *Pulsed inductive thruster component technology*, Technical Report AFAL-TR-87-012, TRW Space and Technology Group, Redondo Beach, CA, Apr. 1987.
- [59] R.H. Lovberg and C.L. Dailey, “PIT Mark V design”, *AIAA/NASA/OAI Conference on Advanced SEI Technologies*, Cleveland, OH, Sept. 4-6, 1991. AIAA Paper 91-3571.
- [60] S.W. Benson and J.R. Frus, “Advanced pulsed plasma thruster electrical components”, *37th Joint Propulsion Conference*, Salt Lake City, UT, July 8-11, 2001. AIAA Paper 2001-3894.

- [61] R.H. Lovberg and C.L. Dailey, *Design of PIT MkVI*, Technical Report NASA-CR-2000-210573, TRW, Inc., Redondo Beach, CA, Dec. 2000.
- [62] J.H. Poylio, D. Russell, W. Goldstein, B. Jackson, R.H. Lovberg, and C.L. Dailey, “Pulsed Inductive Thruster: Flight-scale proof of concept demonstrator”, 40th *AIAA/ASME/SAE/ASEE Joint Propulsion Conference*, Ft. Lauderdale, FL, July 11-14, 2004. AIAA Paper 2004-3640.
- [63] M. Alidières, R. Aymar, F. Koechlin, P. Jourdan, and A. Samain, “Shock and current sheet structure in a theta-pinch configuration”, *Phys. Fluids*, **13**(6):1525, June 1970.
- [64] M.R. LaPointe, “High power theta-pinch propulsion for piloted deep space exploration”, *Proceedings of the Space Technologies and International Forum (STAIF) 2000 Conference*, M.S. El-Genk (ed), AIP Conference Proceedings **504**:1564–1571, Jan. 30-Feb. 3, 2000.
- [65] S. Gartenhaus and L.M. Tannenwald, “Propulsion from pinch collapse”, in *Plasma Acceleration*, pages 73–78, S.W. Kash (ed), Stanford University Press, Stanford, CA, 1960.
- [66] R.G. Jahn and W. von Jaskowsky, “Structure of a large-radius pinch discharge”, *AIAA J.*, **1**(8):1809, Aug. 1963.
- [67] R.G. Jahn, W. von Jaskowsky, and R.L. Burton, “Ejection of a pinched plasma from an axial orifice”, *AIAA J.*, **3**(10):1862, Oct. 1965.
- [68] M. Tuszewski, “Field reversed configurations”, *Nuclear Fusion*, **28**(11):2033, Nov. 1988.
- [69] H. Alfvén, L. Lindberg, and P. Mitlid, “Experiments with plasma rings”, *J. Nuclear Energy, Part C: Plasma Phys.*, **1**(3):116, 1960.

- [70] M. Tuszewski, W.T. Armstrong, R.E. Chrien, W.N. Hugrass, K.F. McKenna, D.J. Rej, R.E. Siemon, D.P. Taggart, and B.L. Wright, “Axial dynamics in field-reversed theta pinches. I: Formation”, *Phys. Fluids B*, **3**(10):2844, Oct. 1991.
- [71] A.L. Hoffman, P. Gurevich, J. Grossnickle, and J.T. Slough, “Inductive field-reversed configuration accelerator for tokamak fueling”, *Fusion Sci. Technol.*, **36**(2):109, Sept. 1999.
- [72] D.J. Rej, W.T. Armstrong, R.E. Chrien, P.L. Klingner, R.K. Linford, K.F. McKenna, E.G. Sherwood, R.E. Siemon, M. Tuszewski, and R.D. Milroy, “Experimental studies of field-reversed configuration translation”, *Phys. Fluids*, **29**(3):852, Mar. 1986.
- [73] A. Shiokawa and S. Goto, “Dynamic property of spontaneous toroidal field in field-reversed configuration plasmas”, *Phys. Fluids B*, **5**(2):534, Feb. 1993.
- [74] H. Himura, S. Okada, S. Sugimoto, and S. Goto, “Rethermalization of a field-reversed configuration plasma in translation experiments”, *Phys. Plasmas*, **2**(1):191, Jan. 1995.
- [75] H. Himura, S. Ueoka, M. Hase, R. Yoshida, S. Okada, and S. Goto, “Observation of collisionless thermalization of a plasmoid with a field-reversed configuration in a magnetic mirror”, *Phys. Plasmas*, **5**(12):4262, 1998.
- [76] R.F. Bourque, P.B. Parks, and D.R. Baker, “Pulsed plasmoid electric thruster”, *AIP Conference Proceedings*, **217**(2):501–506, Jan. 5, 1991.
- [77] S.J. Koelfgen, C.W. Hawk, R. Eskridge, M.H. Lee, A. Martin, and J.W. Smith, “A plasmoid thruster for space propulsion”, 39th *AIAA/ASME/SAE/ASEE Joint Propulsion Conference*, Huntsville, AL, July 20-23, 2003. AIAA Paper 2003-4992.